LUND UNIVERSITY

MASTER THESIS

Test of a low Noise/low power preamplifier for the PANDA Electromagnetic Calorimeter

Author:
FAISAL ZEESHAN

Supervisors:
Prof. Bernd KRUSCHE
Prof. Anders OSKARSSON

February 18, 2013

Abstract

This thesis project was carried out in department of physics (Division of experimental nuclear and particle physics), University of Basel, Switzerland.

The PANDA (Anti-proton Annihilations at Darmstadt) experiment is one of the biggest projects at the new FAIR (Facility for Anti-proton and Ion Research) facility in Darmstadt. The main purpose of the PANDA experiment is to study Hadron spectroscopy, Nucleon structure and Hyper-nuclei using the interaction between antiprotons and protons (as fixed target). Scientists were working successfully on the idea of antiproton projects at LEAR/CERN and the Fermilab antiproton accumulator, which lead to initiate the PANDA project.

The University of Basel (Physics department) is collaborating in the PANDA project in particular on the design and test of special preamplifier circuits for the readout of the electromagnetic calorimeter (EMC) which is a major subunit of the detector. The Forward part of the EMC consists of 3856 PWO II crystals and each crystal will be equipped either with one Vacuum-Photo-Tetrode (VPTT) or with two Large Area Avalanche Photo-diodes (LAAPDs). For the readout of the PANDA EMC, special types of pre-amplifiers (LNP) are needed to be developed.

Some of the development for low noise/ low power (LNP) preamplifier has already been done at Basel University (Physics department). The expected timeline for the further development, production, testing and sorting of LNP would end in 2015.

Acknowledgements

This work would not have been possible without the guidance and the help of several individuals who in one way or another contributed and extended their valuable assistance in the preparation and completion of this study. I would like to thank my local supervisor, Prof. Anders Oskersson, department of Physics, Lund University, Sweden and in particular my supervisor in Basel, Prof. Bernd Krusche, department of physics (Division of experimental nuclear and particle physics) University of Basel, for giving me an opportunity to work in their groups and guide me in this interesting topic. I would like to thank Dr. Irakli Keshelashvili for his work that inspired this thesis, for his programming support as well as many productive discussions and always being able to answer my questions. And last but not least, thanks to my family and friends, especially my parents and the one above all of us, almighty Allah, for answering my prayers and for giving me the strength.

Contents

Chapter 1

Introduction

1.1 Introduction

The $\bar{\text{P}}$ANDA (AntiProton Annihilations at Darmstadt) project is basically constructed to study hadron physics and get to know more about the nature of the strong interaction. It appears like a big challenge for the scientists to build an experimental setup which fulfills the requirements of the physics needs without jeopardizing quality. The design of the $\bar{\text{P}}$ANDA project clearly helps us to get the answers of some important questions. For example: Confinement of the quarks, existence of glue balls and the hybrids, exotic states in the charmonium region, non perturbative QCD dynamics and study of nucleon structure with electromagnetic processes [1]. Experimentally there are many different methods to study hadron structure but antiproton proton $\bar{\text{p}}$p annihilation is expected to give us optimum results with high precision and statistics.

1.2 Overview of the $\bar{\text{P}}$ANDA experiment

In the $\bar{\text{P}}$ANDA experiment, an antiproton beam will be generated from the High Energy Storage Ring (HESR) at the FAIR (Facility for Antiproton and Ion Research) facility in Darmstadt colliding with the internal proton target.

The HESR will have two different operation modes [2].

(1) The high intensity mode, where a beam momentum spread $\delta p/ = p = 10^{-4}$ a luminosity of $2 \times 10^{32} cm^{-2} s^{-1}$ will be available.

(2) The high resolution mode, where the luminosity requirement will be released to $10^{31} cm^{-2} s^{-1}$ to have a maximum momentum precision of 10^{-5}. These operation modes will help us to measure masses and widths of the hadronic states.

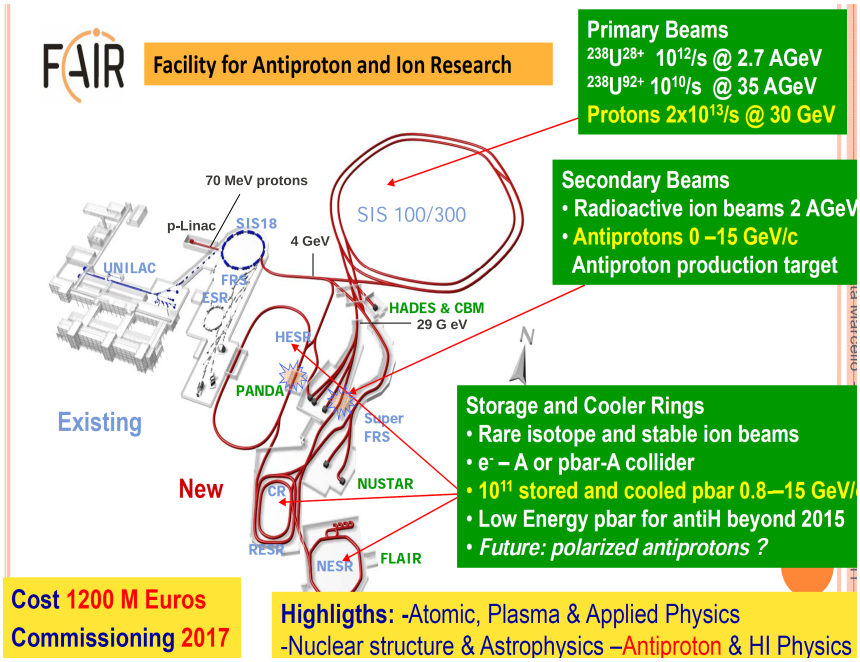

Figure 1.1: It shows an existing accelerators and future accelerators at GSI [3], In 2001, the major plan was to develop a new accelerator facility at GSI called FAIR. A proton linac will be constructed on the site of the GSI. Protons of energy 70 MeV will be injected into the existing synchrotron SIS18 which acts as a preaccelerator for the future synchrotron SIS100 where protons will be accelerated up to 29 GeV/c. Then they will be extracted to the antiproton separator where they hit in each 5 seconds with the antiproton production target (copper or nickel). Antiprotons are collected in the storage ring CR and then transported towards the HESR [25]. HESR will provide antiproton beams with high quality for the $\bar{P}ANDA$ experiment. The expected time line for the installation of all the components at FAIR would be in 2016 and the operational year would be in 2018.

A major component part of the $\bar{P}$ANDA experiment is the Electro Magnetic Calorimeter (EMC). The EMC consists of two parts, a target spectrometer EMC and a forward spectrometer EMC. The material used to build the target spectrometer EMC is lead tungstate $PbWO_4$ scintillating crystals (PWO) as already used in the CMS, ALICE and PRIMEX electromagnetic calorimeters [4]. The target spectrometer EMC is further divided into three parts to cover almost all expected directions of particles, produced from the target material after interaction with the incident beam. The largest part is called barrel part which consists of 11360 crystals and the length of each crystal is about 200 mm. The backward end-cap consists of 592 crystals and in the forward direction the end-cap EMC consists of 3856 crystals. The calorimeters are used to measure energy and position of the incoming particles. During the absorption process, particles interact with the material of the calorimeter and produce secondary particles, which further interact with other particles and make an electromagnetic (EM) shower. Sensitive photo detectors will be used to detect signals produced from

the EMC. For the P̄ANDA project, the low energy threshold of less than 10 MeV requires good quality and sensitive photo detectors.

Expected event rates for the barrel part of the EMC vary between 10 KHz to 100 KHz and up to 1 MHz for the forward endcap of the EMC. Therefore, for the barrel and backward part of the EMC special type of the Large Area Avalanche Photo-diodes (LAAPDs) have been chosen. For the forward end-cap of the EMC, Vacuum-Photo-Tetrodes (VPTTs) and the Large Area Avalanche Photo-diodes (LAAPDs) have been chosen respectively.

Photo detectors will be attached directly to all of the crystals of EMC and the preamplifiers will be placed close to the photo detectors inside the calorimeter. To get a good quality amplified signal, scintillating crystals including photo detectors and preamplifier's will be cooled down up to -25 ℃. Low noise/ low power (LNP) charge-sensitive preamplifier circuit is developed at Basel university (Physics department). The LNP preamplifier design is based on a low-noise J-FET transistor.

Digitizer modules will be used to digitize signals getting from the photo detectors (LAAPDs, VPTs, VPTTs) These digitizers consist of high frequency and low power pipelined ADC chips which will be placed at a distance of 20-30 cm from the barrelpart of the EMC and 90-100 cm from the forward endcap of the EMC [1]. For the complete structure of the P̄ANDA detector, all of these components will be embedded in the general Detector Control System (DCS) to get a correct and a stable operation of an experiment [1].

1.3 Physics behind the P̄ANDA experiment

For many decades, physicists have been trying to understand the phenomena of strong interaction and still need to get answers of many fundamental questions. For example: confinement of the quarks, existance of the glueballs and hybrids, nature of strong interaction and more about hadronic matter [5]. So the P̄ANDA experiment will explore hadronic matter and gives us a complete understanding of hadron spectroscopy which leads us to know more about unclear aspects of Quantum Chromo Dynamics (QCD).

Protons and neutrons are commonly called nucleons which come from the family of hadrons. Hadrons are made of quarks and quarks are the only particles that can interact strongly. The strong force between two quarks is very low at short distances but it increases when the distance between the two quarks also increase.

Whenever a quark-antiquark pair is separated, at the same time the energy of the gluon field is also increased rapidly, which causes to form a new quark-antiquark pair. This phenomenon is called confinement. This is one of the important problems to understand in modern physics.

Many processes at high energies can be explained by perturbative QCD, but this theory fails when the distances among the quarks are equal to the size of the nucleon. On the other hand, in the region of non-perturbative strong QCD, the force among the quarks becomes so strong that they can not be separated further [6]. The main purpose of the P̄ANDA collaboration is to connect the perturbative and the non-perturbative QCD regions [6]. A large part of this experiment will be dedicated to understand some of the important questions like

Why we can not observe free quarks?
What would be the structure of the nucleon?
Does non-standard hadron configuration exist?
How are color neutral objects formed?
Hadron spectroscopy?
Charmonium Spectroscopy?

1.3.1 Hadron Spectroscopy

Hadron physics still needs to answer some of the important questions and one of them is gluonic excitation. Gluonic hadrons are divided into two parts called glueballs and hybrids. Gluballs consist of pure glue states and hybrids consist of $q\bar{q}$ pair and excited glue [5]. Long distance features of QCD (Quantum ChromoDynamics) are used to determine the properties of glueballs and hybrids. Antiproton-proton annihilation will help us to search on gluonic hadrons. It will also form all of the charmonium states and we will be able to collect thousands of $c\bar{c}$ states per day. This will help us to explore energy regions below and above the open charm threshold [5].

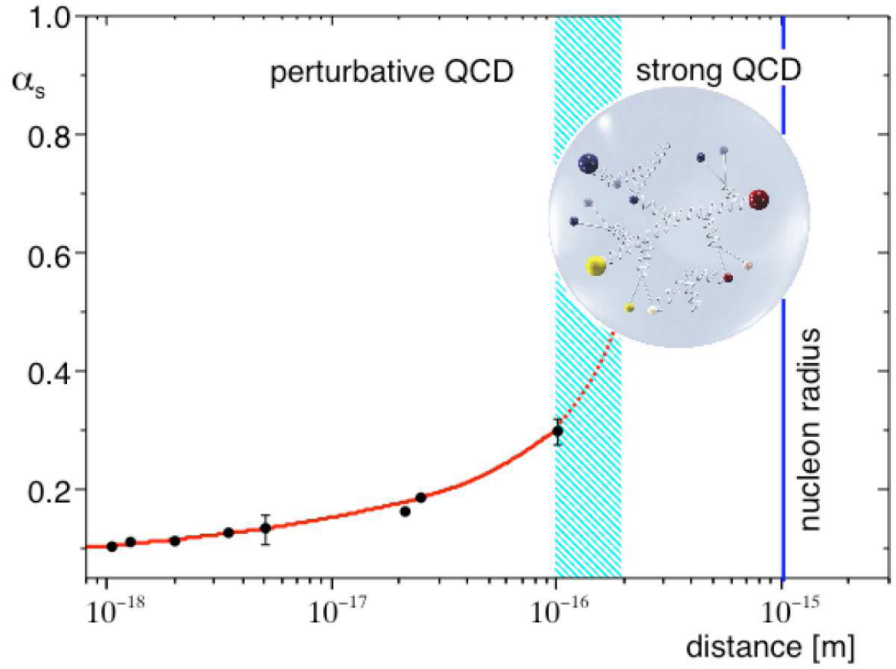

Figure 1.2: The α_s (strong coupling constant), as a function of the distance scale, QCD becomes non-perturbative with large distances. Therefore study of strong interaction in the transition region between perturbative QCD and nuclear phenomena is important. [6]

Charmonium Spectroscopy

It is expected that we can observe all of the possible charmonium states directly by $p\bar{p}$ annihilation. For a better understanding of QCD, it is important to get all

of the possible charmonium states below and above the open charm threshold. The charmonium system and the possible transitions are shown in figure (1.3). There are eight states below the $D\bar{D}$ threshold at 3730 MeV. As these $c\bar{c}$ states are so narrow and if we want to study their central masses and widths, then it requires to use an energy scan across the spectral function. All of the states below the $D\bar{D}$ threshold are known but still the behavior of some of the states are uncertain and unclear.

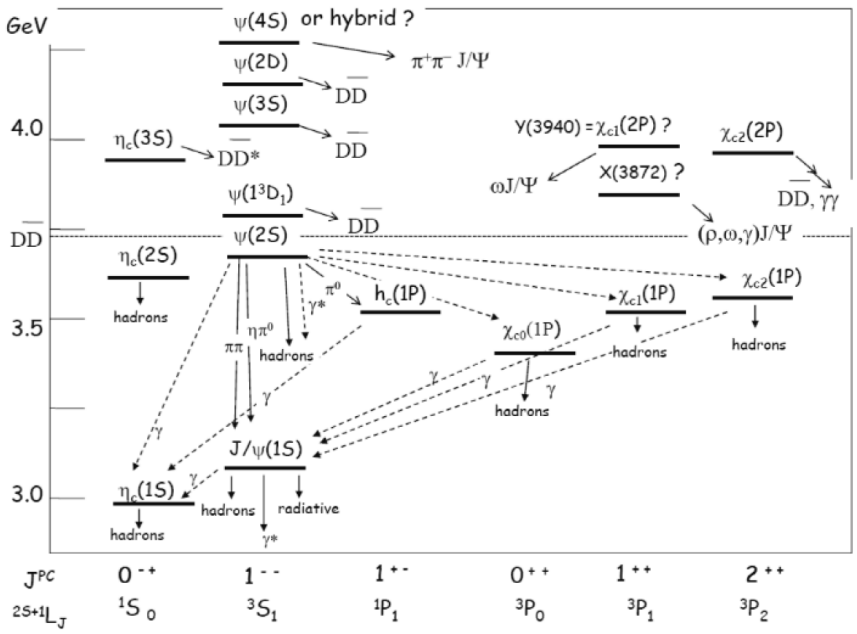

Figure 1.3: The Charmonium spectrum and its transitions, Proton-antiproton collisions will exploit masses up to 5.5 GeV/c^2 for $\bar{P}$ANDA experiment, leads to get access for glueballs, charmed hybrids, and charmed-rich four-quark states [7].

On the other hand those states which are above the $D\bar{D}$ threshold are also shown in figure (1.3). These states are unconfirmed and unobserved states. Some of the new states have been recently discovered by BaBar, Belle and CLEO labeled as X, Y and Z states[8]. But still we don't have deeper understanding of these states. After studying the properties of X,Y and Z states, it is clear that these states are not conventional charmonium states. The important thing of $p\bar{p}$ annihilation at $\bar{P}$ANDA experiment is the spectroscopy of so far undiscovered charmonium and charmonium like states with the angular momentum of 2 or higher [8].

D Meson Spectroscopy

The $\bar{P}$ANDA experiment will also help us to go through the D meson spectroscopy. D mesons are the lightest particles which contain charm quarks. The observations of the new states by BaBar, Belle and CLEO introduce more interests in theoretical and experimental parts of particle physics. These new states contradict previously known D states especially the Ds state because of

being lower mass and narrower in width. So far, few states have been predicted theoretically on an upper limit of few keV up to 200 keV, based on its internal structures [8]. Experimentally few states have been observed up to few MeV width because of the limited detector resolution. Now with the help of High Energy Energy Storage Ring (HESR), $\bar{\text{P}}$ANDA beam will be able to measure these widths down to values of 100 keV [11] because of its good momentum resolution.

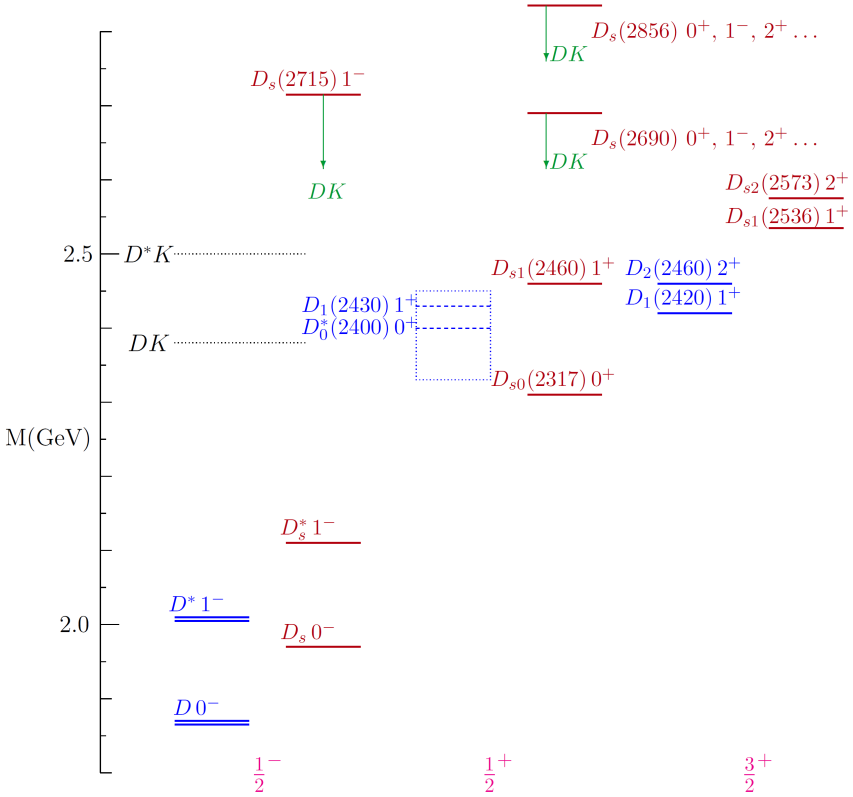

*Figure 1.4: New states Ds(2317)[10,11,12] and Ds(2460)[10,13,12] have been observed by Belle, BaBar, and CLEO [9], Both states are less then 1 MeV wide by the same energy gap of 45 MeV below the isospin averaged DK and D*K thresholds respectively [8]. In the $\bar{\text{P}}$ANDA experiment, the anti proton beam line with its good momentum resolution will helps us to determine the width of Ds(2317) state.*

Baryon Spectroscopy

The $\bar{\text{P}}$ANDA experiment will help us to get comprehensive details about Baryon Spectroscopy. The available information is not enough on the Ξ and Ω excitation spectrum with one or zero known 4-star resonances, respectively[8].

1.3.2 Nucleon Structure

To understand the structure of the nucleon, a techniques has been recently introduced called Generalized Parton Distributions (GPDs)[10]. $p\bar{p}$ annihilation into two photons at large 's' and 't' can also be described in terms of (GPDs)[10]. There are different kinds of methods offered to measure the crossed-channel Compton scattering and annihilation processes with a scalar meson, a vector meson, or a lepton pair in the final state[10]. The nucleon structure can also be precise in terms of electromagnetic Form Factors (FF). This field electromagnetic Form Factors (FF) will helps us to investigate the electric $|G_E|$ and magnetic $|G_M|$ distributions within the nucleon. From different experiments, the proton time-like form factors have been measured mostly in the low Q^2 region[10]. It is almost impossible to measure $|G_E|$ and $|G_M|$ separately because of poor statistics. But in the $\bar{P}$ANDA experiment, it is possible to measure $|G_E|$ and $|G_M|$ separately due to very large statistics over a large Q^2 range. It also helps us to improve the results of E 760 and E 835 [10] measurements.

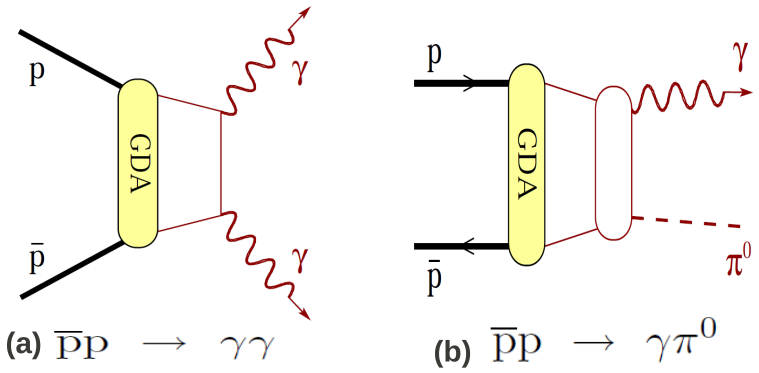

Figure 1.5: Two different electromagnetic processes [26]. In figure (a), the handbag diagram of wide angle Compton scattering (WACS) is the process with emission of the two final photons at large polar angle in the centre of mass system. In figure (b), meson production process can also give valuable information about the structure of the proton. The blob on the right hand side represents the parametrised general dynamics for process.

1.3.3 $\Lambda\Lambda$ Hypernuclei

Hypernuclei are defined by introducing the new quantum number strangeness, into a nucleus, which will replace an up or a down quark in a nucleon. Single and double Λ hypernuclei are already discovered. Only 6 double Λ hypernuclei are known up to now. The $\bar{P}$ANDA experiment by which the anti-proton beam $\bar{P}$ will be used with a combination of highly sensitive experimental techniques, will open a new chapter of strong nuclear physics and help us to determine $\Lambda\Lambda$ strong interaction strength, which is not possible to measure by direct scattering experiments.

In the $\bar{\text{P}}$ANDA experiment, bound states of Ξ hypernuclei will be used to form double Λ hypernuclei [26]. Production of double Λ hypernuclei is based on two steps as shown in figure (1.6) First step: antiproton beam will hit the primary carbon target and produce low momentum Ξ^- hyperons by the following reactions.

$\bar{\text{p}} + \text{p} \rightarrow \Xi^-\Xi^+$

$\bar{\text{p}} + \text{n} \rightarrow \Xi^-\Xi^o$

Second step: Ξ^- will be captured by the external secondary target and form double Λ Hypernuclei.

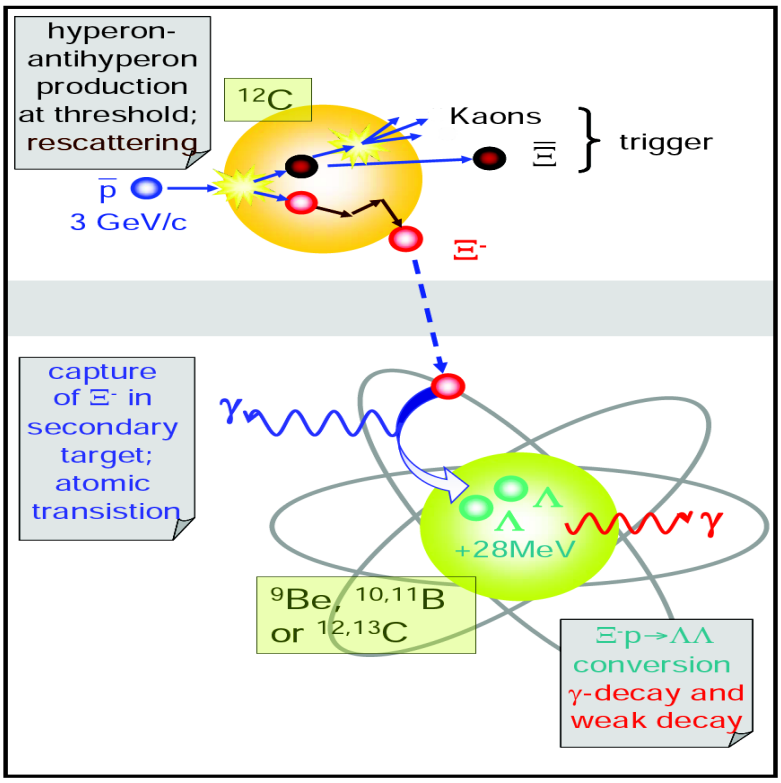

Figure 1.6: A two step process for the formation of double lamda hypernuclei in PANDA experiment [26].

1.3.4 Other Topics

The importance with the $\bar{\text{P}}$ANDA experiment is that it will also provide us some of the key information about topics which are not discussed so far. For example: $\bar{\text{P}}$ANDA experiment will study the properties of hadrons. So far, most of the experiments have been performed on the light quark sector but $\bar{\text{P}}$ANDA experiment will extend our studies towards heavy-quark sector as well. Recently

it has been observed experimentally that the properties of mesons like Π , K , and Ω have been changed in a dense environment [6].

J/ψ Nucleon interaction will also studied in the $\bar{P}$ANDA experiment because so far we have seen so many uncertainties during the indirect experiment, for example, the studies of high energy proton-nucleus collisions [8].

Scientists from different countries related with the $\bar{P}$ANDA collaboration are also taking interest to make use of the electro-magnetic probes, photons and leptons in the antiproton-proton annihilation. These probes will help us to study the structure of the proton by measuring Generalized Parton Distributions (GPDs) and to determine quark distribution functions via the Drell-Yan processes[6].

Chapter 2

The $\bar{\text{P}}$ANDA Experiment

2.1 Introduction

$\bar{\text{P}}$ANDA (AntiProton Annihilations at Darmstadt) is a big project which is under construction on the area of GSI Helmholtzzentrum für Schwerionenforschung at Darmstadt in Germany. There are almost 450 scientists from 17 different countries working on various topics like strong and weak forces, structure of hadrons and exotic states of matter in this organization[11].

The main purpose to build this project is to operate the Facility for Antiproton and Ion Research (FAIR). In 2001, The total cost of the FAIR project is estimated to be about 1.4 billion dollars. While, from the total cost of 70% has been contributed by Germany, and the rest of 30% is contributed by 17 collaborating countries. The biggest contribution comes from Russia, about 245 million dollars[12].

FAIR can also be used to produce and cool down anti-proton beams with a momentum between 1.5GeV/c and 15GeV/c interacting with internal targets. The intense pulsed ion beam is provided to the central part of FAIR called the synchrotron complex. The primary proton beam produces anti-protons which are filled into the High Energy Storage Ring (HESR). These anti-protons are then collided with fixed targets, either a hydrogen cluster jet or a high frequency frozen hydrogen inside the $\bar{\text{P}}$ANDA detectors.

This experiment is based on hadron spectroscopy to search exotic states in the charmonium mass region. Also, the interaction of charmed hadrons with the nuclear medium, the nuclear potential and hyperon-hyperon interactions on double-hypernuclei can be studied nucleon structure by applying different electromagnetic processes as discussed can be investigated.

2.2 High Energy Storage Ring (HESR)

The High Energy Storage Ring (HESR) is located at FAIR facility. It will be used to produce anti-proton beam with very high quality. It contains some of the important features that makes it special. For example, beam parameters consist of two operation modes: High Luminosity mode (HL) with beam intensities upto 10^{11}, and High Resolution mode (HR) with a momentum spread down to a few times 10^{-5}[5]. It is specially designed in two 180^{o} arc sections

which are connected by two long straight sections. One straight section consists of an electron cooler system and the other section consists of internal target experimental station (H_2 Pellet, Injection kickers, Septa) as shown in figure (2.1).

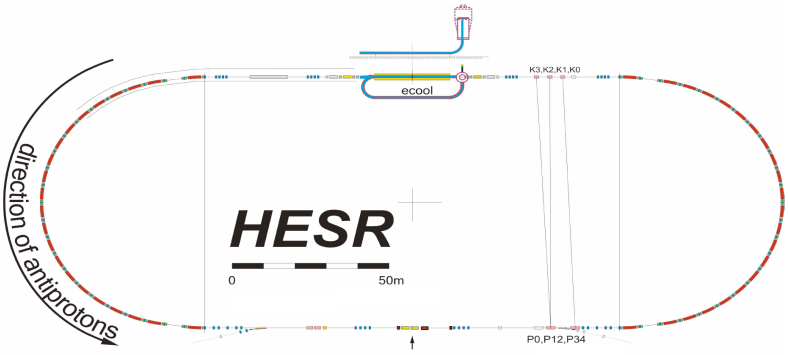

Figure 2.1: Shows direction of antiprotons, position for injection, cooling devices and experimental installations[5].

Some important parameters required to operate HESR are shown in table 2.1.

Injection Parameters	
Transverse emittance	0.25 mm mrad (normalized, rms) for 3.5. 10^{10} particles, scaling with number of accumulated particles: $\varepsilon \sim N^{4/5}$
Relative momentum spread	$3.3.10^{-4}$ (normalized, rms) for 3.5. 10^{10} particles, scaling with number of accumulated particles: σ_p/p $N^{4/5}$
Bunch length	150m
Injection Momentum	3.8 GeV/c
Injection	Kicker injection using multi-harmonic RF cavities
Experimental Requirements	
Ion species	Antiprotons
$\bar{p}$ production rate	$2.10^7/s$ ($1.2.10^{10}$ per 10 min)
Momentum / Kinetic energy range	1.5 to 15 GeV/c / 0.83 to 14:1 GeV
Number of particles	10^{10} to 10^{11}
Target thickness	$4.10^{15} atoms/cm^2$ (H_2 pellets)
Transverse emittance	¡ 1 mm. mrad
Betatron amplitude E-Cooler	25-200m
Betatron amplitude at IP	1-15m
Operation Modes	
High resolution (HR)	Luminosity of $2.10^{31} cm^{-2} s^{-1} for 10^{10}$ p rms momentum spread $\sigma_p/p \leq 2.10^{-5}$, 1.5 to 9 GeV/c, electron cooling up to 9 GeV/c
High luminosity (HL)	Luminosity of $2.10^{32} cm^{-2} s^{-1} for 10^{11}$ p rms momentum spread $\sigma_p/p \sim 10^{-4}$, 1.5 to 15 GeV/c, stochastic cooling above 3:8 GeV/c

Table 2.1: This table shows a important features of HESR. such as, Injection Parameters, Experimental Requirements, Operation Modes[5]

.

2.3 Experimental Setup

The design of the $\bar{P}$ANDA experiment is shown in figure (2.2). This design is aimed to get excellent results for 4π acceptance, High resolution for tracking, calorimetry and identification of the particles. The $\bar{P}$ANDA detector is divided into two main parts.

(1) Target Spectrometer

(2) Forward Spectrometer

So far, the total length of the $\bar{P}$ANDA detector is 12 m and width is 3.5 m.

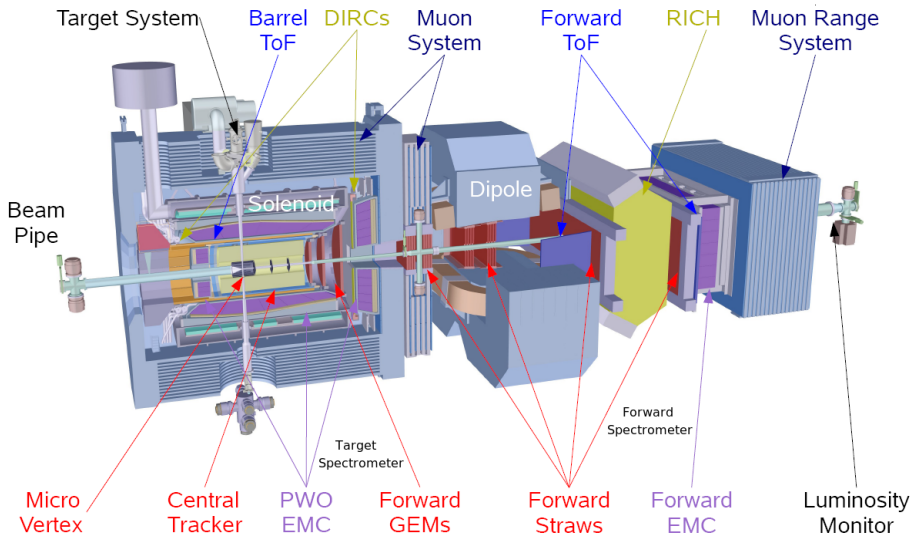

Figure 2.2: shows an overview of the $\bar{P}$ANDA spectrometer. The target spectrometer is based on superconducting solenoid magnet and forward Spectrometer is based on dipole magnet . It also shows the placement of different detectors [13].

The Target Spectrometer is based on a superconducting solenoid magnet and the Forward Spectrometer is based on a dipole magnet. A solenoid magnet provides field strength of 2 T and it has coil opening of 1.89 m and a coil length of 2.75 m [1]. The target spectrometer is located in the barrel part at an angle larger than 22^o and an endcap part for forward range down to 5^o in the vertical and 10^o in the horizontal plane [1]. The configuration of the dipole magnet is as follows. It has a field strength of 2 T with a 1.4 m wide and 70 cm high opening [1], and it covers forward angles. Both spectrometers will work as trackers to identify Charged particles, including muons and together with electromagnetic calorimetry and they allow detection of the complete spectrum of final states.

For that purpose, the $\bar{P}$ANDA detector is further divided into four parts.

(1) Target system
(2) Particle identification detectors
(3) Tracking devices
(4) Calorimetry

2.4 Target system

A beam of anti-proton will circulate in a HESR about 500 000 times per second [11], without making any interaction with the target material. At the same time it will pass through the electron cooler and in every round trip it will be cooled down and beam will also struggle not to loose energy, which, in fact, helps to maintain high beam quality. The anti-proton beam will have momentum 1.5GeV/c up to 15GeV/c. But if we want to get highly precise charmonium spectroscopy then it is needed to improve the beam properties below 8 GeV/c momentum by cooling using high energy electrons [11].

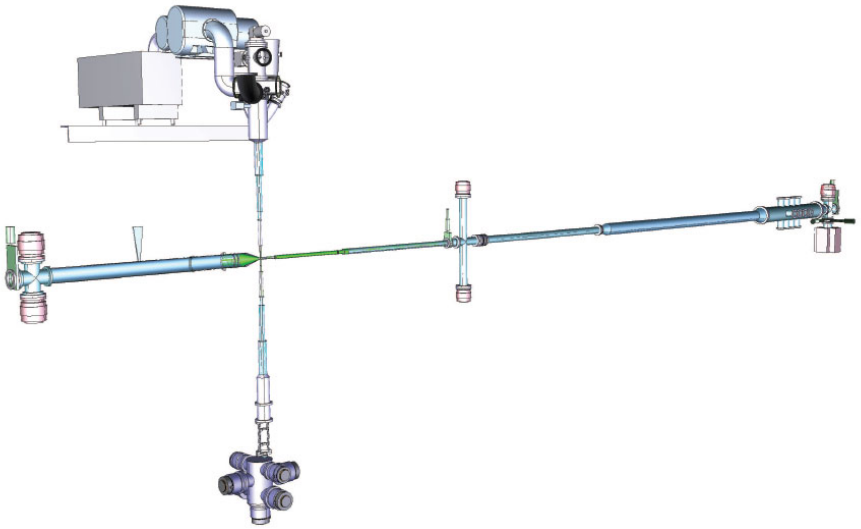

Figure 2.3: Anti-proton beam line circulating in the HESR, interacting at an internal target station of the HESR [11].

Experimental Parameters	
$\bar{p}$ production rate	2×10^7/s (1.2×10^{10} per 10 min)
Momentum / Kinetic energy range	1.5 to 15 GeV/c / 0.83 to 14.1 GeV
Number of particles	10^{10} to 10^{11}
Betatron amplitude at IP	1 - 15m
Betatron amplitude E-Cooler	25 - 200m
Operation Modes	
High resolution (HR)	Peak Luminosity of $2\times10^{31}cm^{-2}s^{-1}for10^{10}$ $\bar{P}$ assuming $\rho_{target} = 4.10^{15}atoms/cm^2$ RMS momentum spread $\sigma_p/P \leq 4\times10^{-5}$, 1.5 to 8.9 GeV/c
High Luminosity (HL)	Peak Luminosity up to $2\times10^{32}cm^{-2}s^{-1}for10^{11}$ $\bar{P}$ assuming $\rho_{target} = 4.10^{15}atoms/cm^2$ RMS momentum spread $\sigma_p/P \sim 10^{-4}$, 1.5 to 15 GeV/c

Table 2.2: Some of the statistics about the $\bar{P}$ANDA beam line [12].

2.4.1 $\bar{P}$ANDA Target Materials

Three different types of the target materials will be used for the $\bar{P}$ANDA experiments, depending on the requirements of the experiment. These materials are as follows

(1) Cluster beam target
(2) Pellet beam target
(3) Fiber target

Cluster Beam Target

Cluster jet beams are produced by the expansion of the pre-cooled gases in the micro sized nozzles into the vacuum. When gas passes through such a nozzle, it cools down and makes a supersonic beam. Different types of gases have different behavior depending on the experimental conditions. Nano-particles are created due to the condensation of gases called clusters. The size of the clusters depends on the experimental conditions, typically its like $10^3 - 10^5$ atoms per cluster[11]. Cluster target is an excellent target system because of some important properties of the cluster beam like its homogeneous volume density distribution, a sharp boundary and a constant angular divergence.

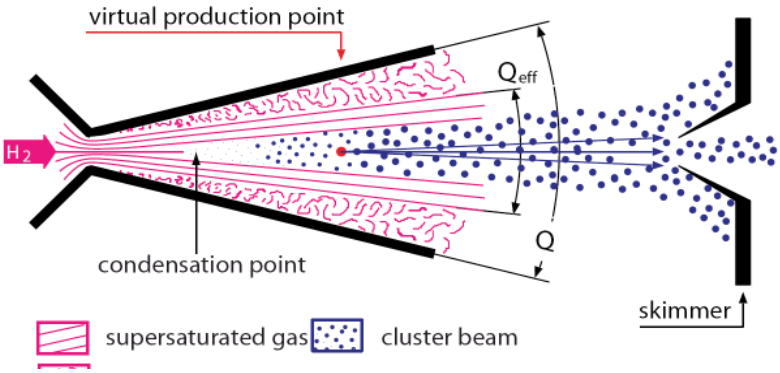

Figure 2.4: Formation of the cluster beams by expansion in a Laval-type nozzle [14]. The distance between the cluster-jet nozzle and the target will be larger due to the detector constraints. The width of the target region should stay smaller than 10 mm when optimized with skimmers.

Pellet beam target

A pellet target consist of the frozen Hydrogen micro-spheres. The size of these pellets depends on the injection nozzle but typically their size varying between 20 μm to 40 μm. These pellets fall vertically with a speed of 60 m/s and the flow rate of 10,000 pellets/s, to interact with a beam of anti-proton [11]. Every single pellet interacts almost 100 times with a beam, so its easy to find out the position of a single pellet with high accuracy in the longitudinal and the transverse direction. Pellet targets were developed in Uppsala and used experimentally WASA-at-COSY. But the $\bar{P}$ANDA pellet target, which is more sophisticated is available at Forschungszentrum Julich[11] as shown in figure 2.5. With the help of this target, different pellets can also be produced from Nitrogen and Argon.

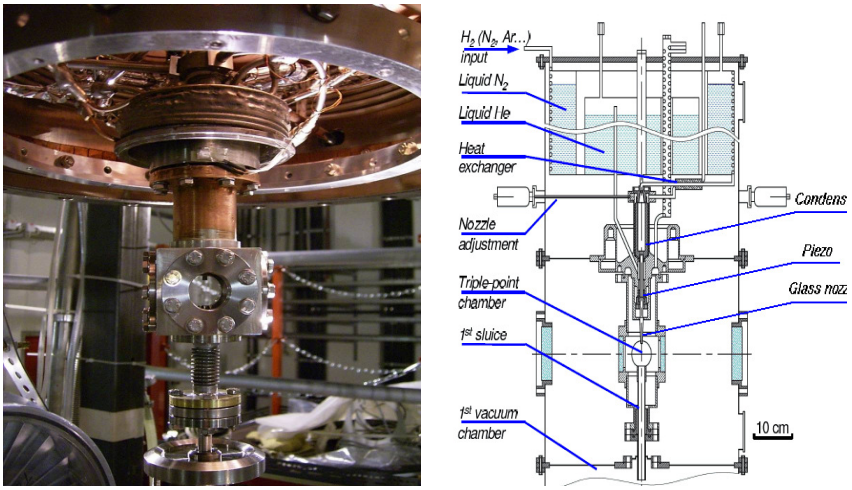

Figure 2.5: Sketch and photo (central part) of the FZ Jülich pellet generator[14], which will serve as a prototype target for the $\bar{P}ANDA$ experiment.

Fiber Target

Whenever we have used fiber or wire as a target as compared to cluster or pellet, it gives us a very good beam emittance of better than 1 pi mm mrad for HESR at the best [11].

2.5 Particle identification detectors

Normally particle identifing is based on mass and charge. Only knowing momentum is not enough to find out the identity of particles. For the identification of charged particles, it requires large momentum range varying from 200MeV/c up to 10GeV/c [11]. Cherenkov detectors are used to identify the charged particles but still some other detectors are under construction to identify by Cherenkov light in the target spectrometer. Therefore the $\bar{P}$ANDA detector will be equipped with different Particle Identification Systems (PID). These systems are as follows.

(1) Barrel DIRC (Detection of Internally Reflected Cherenkov)
(2) Disc DIRC (Detection of Internally Reflected Cherenkov)
(3) Muon detection
(4) Forward RICH
(5) Forward TOF (Time of Flight)

2.5.1 Barrel DIRC (Detection of Internally Reflected Cherenkov Light)

Cherenkov radiation is an electromagnetic radiation which is emitted when charged particles are moving through a dielectric medium at speeds exceeding that of light in the medium and polarizes the molecules of that medium in

it. When these molecules turn back to their ground states, they emit radiations called Cherenkov radiation.

Cherenkov detectors will be used to identify particles of momentum spectrum above 1 GeV/c and some other detectors will be used to identify particles of momentum below the Cherenkov threshold for kaons. Particle can also be identified by the detection of the internally reflected Cherenkov light (DIRC) as observed in BaBar detector [11], when it hits at polar angles between 22^o and 144^o.

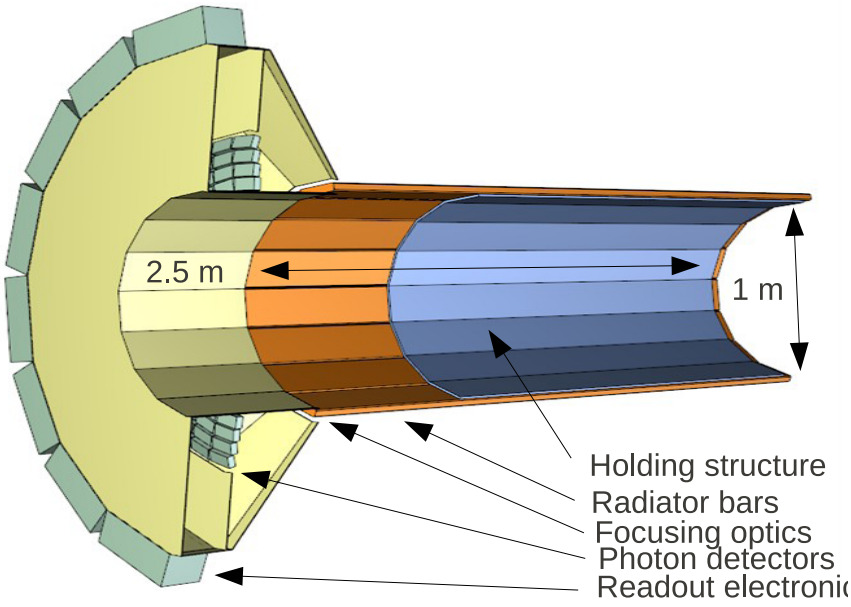

Figure 2.6: Current design of barrel DIRC [15] is similar to the BaBar DIRC and it has the following features. Inner radius: 48 cm, Radiator: 96 bars, fused silica (n=1.47) 17 mm (T) × 33 mm (W)× 2500 mm (L), Compact photon detector: array of MCP − PMT (Burle Planacon) in magnetic field $0.5 - 1T$ *total* $7000 - 10000$ *channels [15].*

2.5.2 Disc DIRC (Detection of Internally Reflected Cherenkov)

The forward region of the target spectrometer will be covered by a new type of Cherenkov detector called Disc DIRC as shown in figure 2.7. The radiator has a form of a disc which is made of fused silica. The disc has a diameter of about 2 m and a thickness of 20 mm [15]. The central part of the disc consists of a rectangular opening for particles measured in the forward spectrometer. Internally reflected light propagates towards the photo detectors placed on the circumference of the disc as shown in figure 2.7. Currently there are two options for the light-guides towards the photo detectors: either to use LiF mirror elements for mitigating the dispersion effect or to apply a dichroic mirror for the same purpose [15]. Special types of photo detectors will be used because of high magnetic field and high rates of photons up to 0.75 MHz/cm^2. These

types are MCP-PMTs and silicon photo Multipliers (SiPMs).

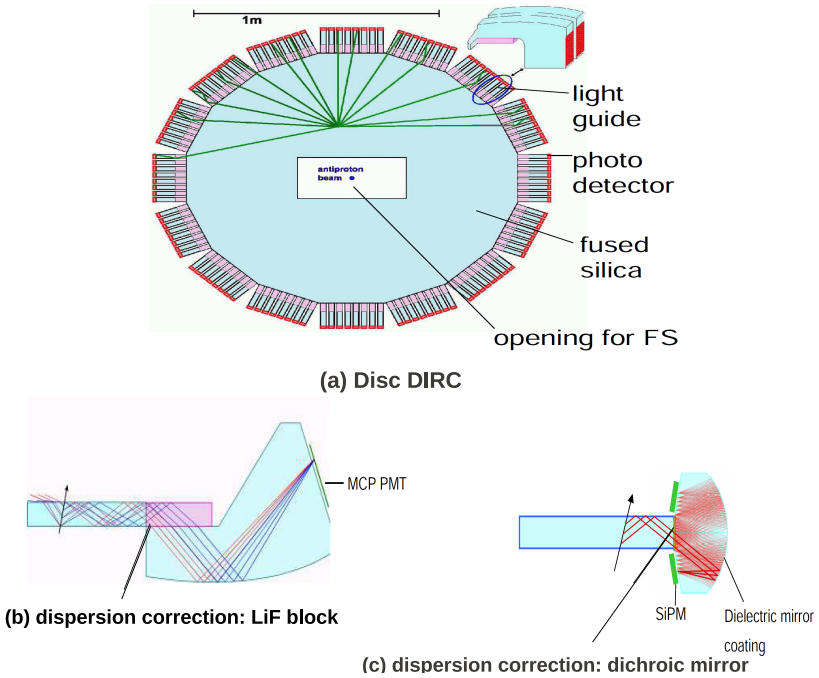

Figure 2.7: (a) shows different functions a disc DIRC, made of fused silica and location of the photo detectors (b) shows option for light guides by using LiF mirror. (c) shows option for light guides by using dichroic mirror [15].

2.5.3 Muon Detection System

In the $\bar{\text{P}}$ANDA experiment with momentum ranges from few GeV up to 10 GeV will be measured. It requires good quality detection systems. If we take Drell-Yan (DY) muon pairs as an example to know the performance of the $\bar{\text{P}}$ANDA detector, then some of the factors should be considered, for example, its average energy from few GeV up to 10 GeV and polar angle of muons.

Muons can be identified by using different types of detector systems or methods [11]. For example

(1) Muon tracker (good clear track sample visibility even in presence of hadronic shower)

(2) Calorimetry, both electromagnetic and hadronic

(3) Scintillator counters (time-of-flight measurement)

(4) Cherenkov counters

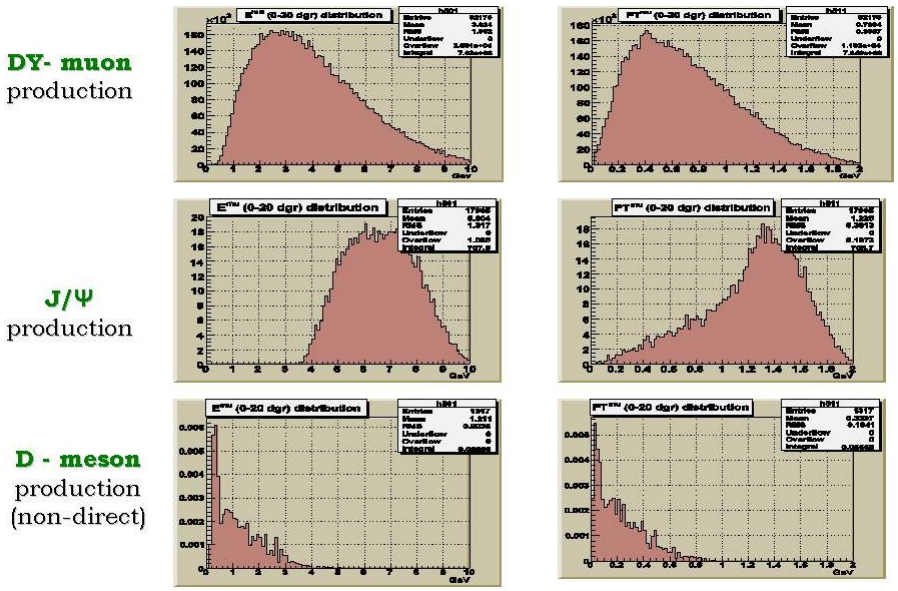

Figure 2.8: shows the distribution of single muons in the angular interval up to 20^o. Left column shows full momentum and right column shows the transverse momentum [11].

Range System (RS) as a Muon System

In december 2008, the $\bar{P}$ANDA collaboration has finally decided to use Range System (RS) for detecting the muons. The structure of RS is most suitable to detect muons stopped by the absorber and also those crossing the iron [11]. In the first case the stopping power of iron is about 1.5 GeV per metre of absorber for the relativistic muons with dE/dx = 2 MeV/g [11].

The muon momenta are specifically dependent on the polar angle of $\bar{P}$ANDA kinematics. Therefore the muon system is specially designed to make use of that and shown in figure 2.9.

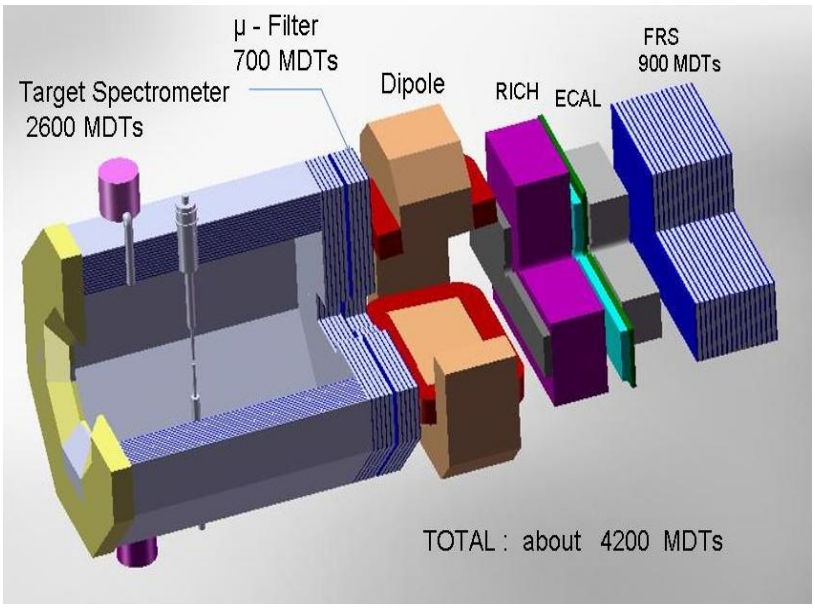

Figure 2.9: shows muon system [11]. The target Spectrometer (TS) consists of two parts: Barrel part (B) and End Cap part (EC), The Muon Filter (MF) is an additional magnetic screen between the solenoid of TS and the dipole of the Forward Spectrometer (FS) and it also increased the depth of absorber for better detection of muons. The total number of Mini Drift Tubes (MDTs) are 4200.

Forward Muon Detectors

The forward muon system is quite similar to the target muon system but give results for higher momenta. The system helps for the detection of pion decays, to determine energy of neutrons and anti-neutrons and the discrimination of pions from muons [5].

2.5.4 Forward RICH (Ring Imaging Cherenkov Counter) detector

To identify particles in the forward direction, dual radiator RICH (Ring Imaging Cherenkov Counter) detectors are preferred. The separation of $\pi/K/p$ at high momentum from 2-15 GeV/c can be possible by using two radiators, called silica aerogel and C_4F_{10}.

2.5.5 Time of Flight (TOF) system

The time of flight barrel system in the target spectrometer will be used to identify slow charged particles in the DIRC detector and for the track deconvolution of the TP-Chamber [11].

The time of flight detector will detect those particles which are slow but cover large polar angles. The target spectrometer has less flight path of only

50 - 100 cm. Therefore the detector must have an excellent time resolution between 50 - 100 ps. This system is also useful to increase the redundancy for other sub-detector systems [11].

2.6 Tracking devices

The tracking system in the target spectrometer consists of the silicon Micro-Vertex detector and the Central Tracker. Two options are considered for the Central Tracker: Straw Tube Tracker or ungated Time Projection Chamber (TPC) with GEM read out. Those particles which are emitted at an angle below 22^o will be tracked by planar GEM detectors. In the forward spectrometer, charged particles are measured by the Forward Tracker consisting of three pairs of planar tube detectors [15].

(1) Micro Vertex Detector

(2) Straw Tube Tracker

(3) GEM-TPC Detectors

(4) GEM Disc detectors

(5) Forward Tracker

2.6.1 Micro Vertex Detector (MVD)

The Micro Vertex Detector (MVD) will be used to detect secondary vertices from D and hyperon decays and will be placed close to the interaction point to get maximum acceptance. The length of the MVD is about 40 cm and its diameter is 30 cm. It consists of four barrel layers and six forward disks as shown in figure 2.10. Two inner barrels are made of hybrid pixel detectors and two outer barrels are made of double sided micro strip detectors. The first four disks are made of hybrid pixel detectors and the last two consist of micro strip detectors [15].

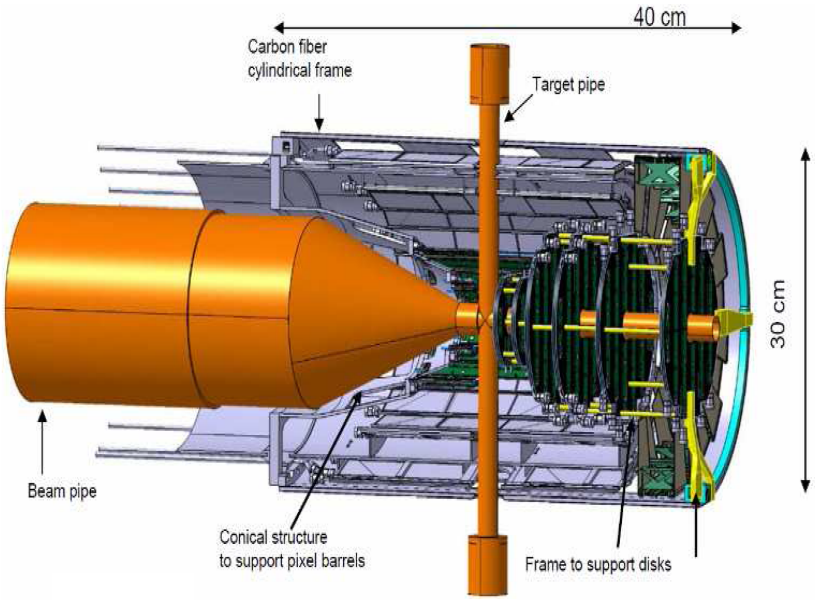

Figure 2.10: It shows Micro-Vertex Detector for PANDA [15]

2.6.2 Straw Tube Tracker

The Straw Tube Trackers are specially designed for the momentum analysis in the target spectrometer. There are 4200 straws around the beam pipe at radial distances between 15 cm and 42 cm with an overall length of 150 cm as shown in figure 2.11.

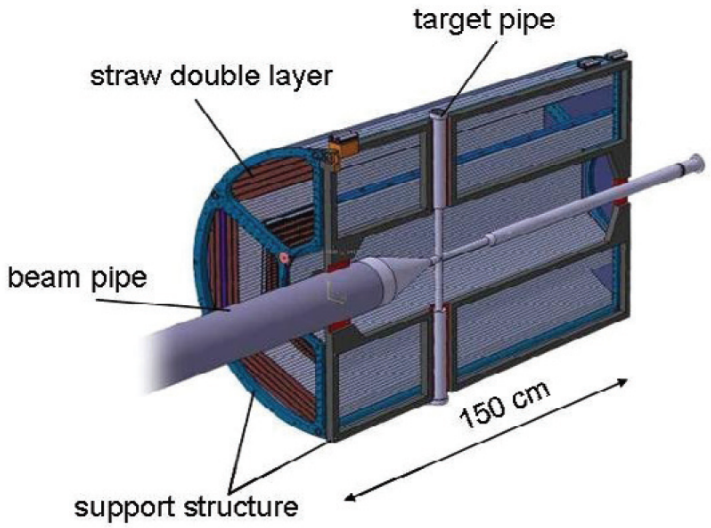

Figure 2.11: Schematic view of the Straw Tube Tracker [15]. Straw diameter: 10 mm. Material: Mylar.

2.6.3 GEM-TPC Detectors

The Time Projection Chamber (TPC) is an alternative method of the Straw Tube Tracker with GEM read out. A TPC consists of two gas filled half-cylinders surrounding the MVD. A reduced scale prototype of GEM TPC was successfully tested at GSI with heavy ion beams [15].

2.6.4 GEM Disc detectors

A set of three GEM detectors will be placed downstream of the target in the target spectrometer. They are made in a form of a disc, each disc consisting of a central double-sided read out plane. The read out electronics is located on the perimeter of the discs [15].

2.6.5 Forward Trackers

Momentum analysis of charged particles deflected in the field of the $\bar{P}$ANDA dipole magnet can be detected by the forward trackers. The forward tracker consists of three pairs (FT1, FT2), (FT3, FT4),(FT5, FT6) of tracking stations [11]. The first pair (FT1, FT2) is placed in front of the dipole magnet. The second pair (FT3, FT4) is placed behind the dipole magnet and the third pair (FT5, FT6) is placed inside the magnet gap to track low momentum particles as shown in figure 2.12 [11].

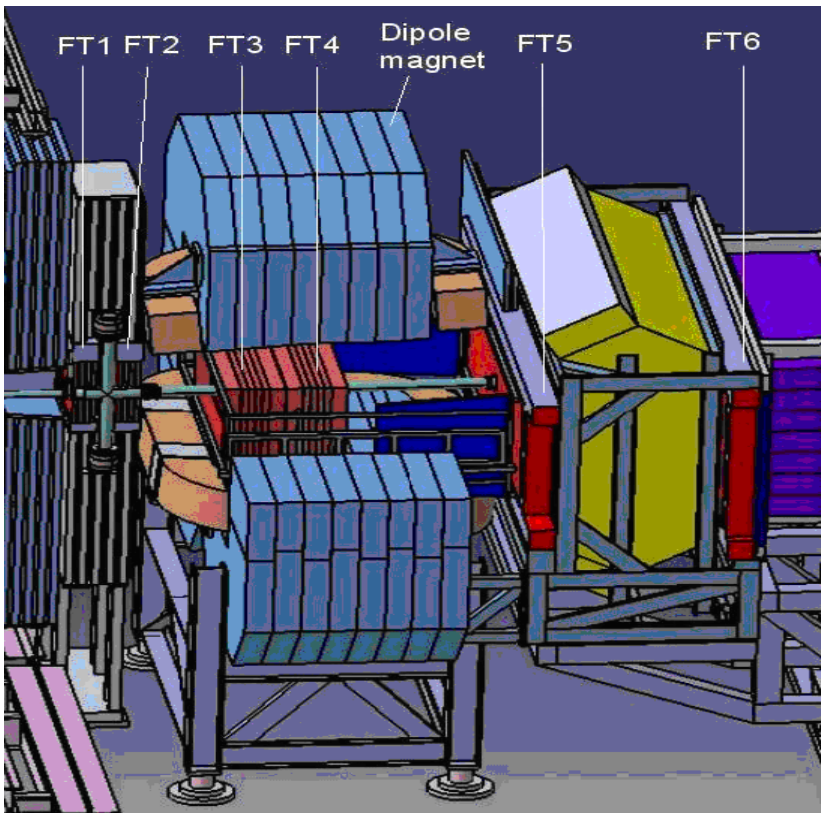

Figure 2.12: Placement of all the three pairs of forward trackers (FT1, FT2), (FT3, FT4),(FT5, FT6) with respect to the dipole magnet; The forward tracker covers angular acceptance up to $\pm 10^o$ horizontal and $\pm 5^o$ vertical with respect to the beam direction [11].

Each tracking station is based on four double-layers. The first and fourth layers consist of vertical straws (0^o) and the two intermediate double-layers (second and third) consist of straws inclined at +5˚and -5˚, respectively [11].

Basic parameters of individual tracking stations are discussed in table 2.3. The presented numbers might change since the optimization of the FT is still going on [11].

Station	No of modules	No of straws	z-pos.[mm]	Area x×y $[mm^2]$
FT1	4×8 = 32	1024	2954	1298×640
FT2	4×8 = 32	1024	3274	1298×640
FT3	4×12 = 48	1536	3945	1944×690
FT4	4×12 = 48	1536	4385	1944×767
FT5	4×25 = 100	3200	6075	4045×1180
FT6	4×37 = 148	4736	7475	5984×1480

Table 2.3: Number of modules and number of straws for individual Forward Tracking stations (FT1, FT2, FT3, FT4, FT 5, FT 6), z-position shows the beam direction downstream the target (z-coordinate), and the horizontal (x) and vertical (y) extension of first double layer in each tracking station[11].

2.7 Calorimetry

Calorimeters are used to measure energy of the neutral and charged particles. Calorimeters are based on those materials which can absorb all energy of the incoming particles. Output signals from the calorimeters are directly proportional to the energy deposition of the incoming particles.

After the absorption of the incoming particles inside the material of Calorimeter, they interact with other particles of the material and produced secondary shower of particles.

There are two types of Calorimeters.

(1) Electromagnetic Calorimeters

(2) Hadron Calorimeters

In the $\bar{P}$ANDA experiment, the Electromagnetic calorimeters will be used. In the target spectrometer, Lead-tungstate material will be used for calorimetry because of its good energy resolution, high density and fast response.

2.7.1 $\bar{P}$ANDA Electro-Magnetic Calorimeter (EMC)

For the $\bar{P}$ANDA Experiment, the Electromagnetic Calorimeter (EMC) is placed inside the superconducting coil of the solenoid in the region of target spectrometer. Good quality Scintillator materials are required to minimize the radial thickness of calorimeter layer to operate high interaction rates and to have good energy resolution. Lead-tungstate (PWO) fulfills all these requirements except for the light output. Some work has been done to improve the quality of (PWO) and this work resulted in (PWO-II) crystals. The light yield has to be as high as possible to achieve a low energy threshold and to achieve good energy resolution. For that purpose EMC has to be cooled down to T = -25 ˚which increases light out by a factor of four.

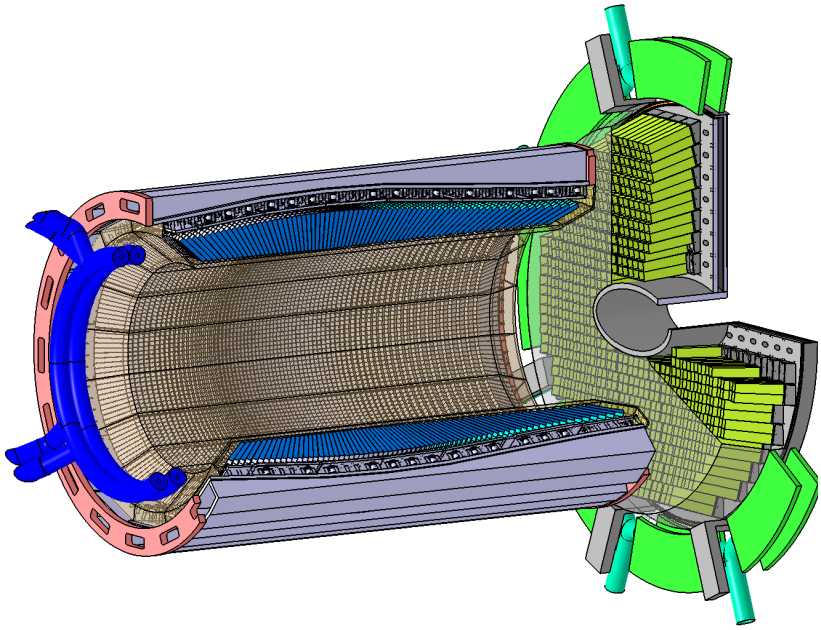

Figure 2.13: The sketch of $\bar{P}$ANDA Electromagnetic Calorimeter [11]. It consists of three main parts. The cylindrical barrel part of the EMC consists of 11360 crystals, typical length of each crystal 200mm. The backward end-cap EMC consists of 592 crystals and the forward end-cap EMC consists of 3856 crystals respectively.

Material	$PWO - II$
Crystal size	2 cm x 2 cm x 20 cm
Thickness	$22X_0$
Energy resolution	1.54% $\sqrt{E/[GeV]} + 0.3\%$
Time resolution	<2 ns
Number of crystals	15808
Geometric coverage	96% 4π

Table 2.4: Basic experimental requirements for $\bar{P}$ANDA EMC [11]

2.7.2 Working Principle of the EMC

When a charged particle strikes the surface of electromagnetic calorimeter material, it absorbs all of its energy and produces secondary charged particles. Then secondary charged particles interact with other particles and make an electromagnetic shower as shown in the figure (2.14).

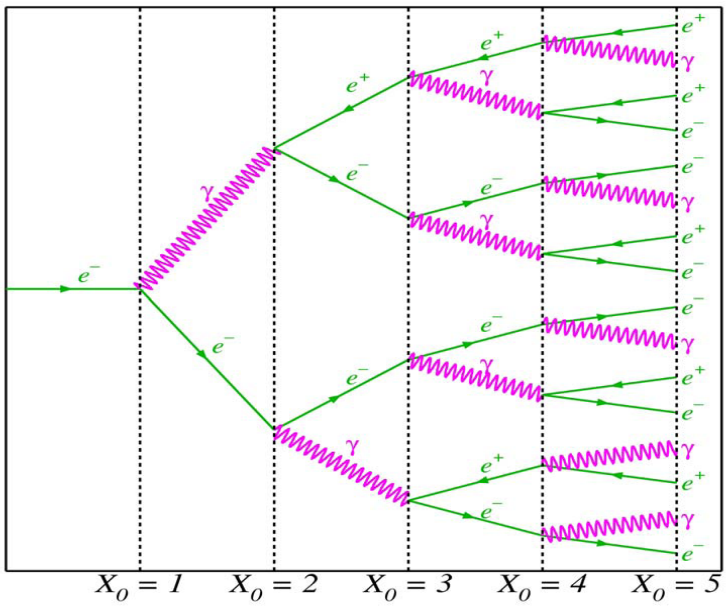

Figure 2.14: It shows an electromagnetic shower [16]. A high energy photon (E_o) is converted into e^-e^+ pair after one radiation length, each particle has energy ($E_o/2$). After two radiation lengths, we have four particles of energy ($E_o/4$), each e^- and e^+ emit bremsstrahlung photon and another e^-e^+ pair. After three radiation length, total number of particles would be eight and energy of each particle is ($E_o/8$). The process continues, until the process isenergetically impossible.

Different processes occur when a gamma particle hits the surface of the calorimeter. For example: Photoelectric effect, pair production and Compton effect. An initial particle must contain enough energy E_c to produce secondary particles. The energy at which ionization loss is equal to the bremsstrahlung loss is called critical energy E_c. E_c for solid materials is about $E_c \approx 600$ MeV/Z.

A few factors are important to produce an electromagnetic shower, those are as follows [16].

(1) If the energy of an electron $E > E_c$, then it covers a distance of about one radiation length and emits photon with energy E = E/2

(2) Each photon with energy E > E_c covers a distance of about one radiation length and creates electron positron pair.

(3) If the electron has energy E < E_c, it will deliver its remaining energy by ionisation energy loss. If it is a positron it will annihilate with electrons and give additional 1.022 MeV.

2.7.3 Forward EMC (Electromagnetic Calorimeter)

A shashlyke-type calorimeter with high resolution and efficiency has been chosen for the detection of high energy photons and electrons for the forward spectrometer [5]. High energy photons and electrons hit the Lead-scintillator sandwiches and produces EMC showers, which produce light which is readout by photomul-

tipliers. To cover the forward acceptance, 26 rows and 54 columns are required with a cell size of 55 mm, i.e. 1404 modules in total, which will be placed at a distance of 7-8 m from the target [5].

2.8 Dipole Magnet

A dipole magnet is an important parts in the forward spectrometer and it will be used for the momentum analysis of charged particles. It covers almost the entire angular acceptance of the target spectrometer of ±10 and ±5 in horizontal and vertical direction respectively [5]. The main challenges are the dimensions of the dipole magnet and its accommodation within the yoke gap. For example, its large opening size (about 1m to 3m) and its short total length (2.5m).

The basic parameters of dipole magnet are shown in table 2.4.

Dipole Magnet (Basic Parameters)	
Field integral	2 Tm
Bending variation	$\leq \pm 15\%$
Vertical Acceptance	± 5
Horizontal Acceptance	± 10
Ramp speed	$1.2\%/s$
Total dissipated power	360 kW
Total Inductance	0.87 H
Stored energy	2.03 MJ
Weight	220 t
Dimensions (H × W × L)	3.88 ×5.3× 2.5 m
Gap opening (H × W)	$0.80 - 1.01 \times 3.10$ m

Table 2.5: The main parameters of $\bar{P}ANDA$ dipole magnet for the forward spectrometer [11].

Chapter 3

Photo detectors for the $\bar{\text{P}}$ANDA EMC

3.1 Introduction

To measure down to a low energy threshold of about 10 MeV, the $\bar{\text{P}}$ANDA EMC requires excellent photodetectors. Lead-tungstate crystals $PbWO_4$ produce comparatively low light intensity and therefore some of the good quality photodetectors will be used to solve this problem. Photo multiplier tubes (PMTs) are good detectors but will not be used in the target spectrometer because of the strong magnetic field of about 2T.

Some special types of the photo detectors have been developed to read out scintillating light emitted from the $PbWO_4$ crystals. These photo detectors must contain some special properties. For example: they can work in high radiation and in strong magnetic field, must be fast and sensitive. So far, three different types of photodetectors have been developed and will be used in the $\bar{\text{P}}$ANDA EMC. These photodetectors are as follows.

(1) Large Area Avalanche Photo-diodes (LAAPDs), Hamamatsu (type number S11048 (X))

(2) Vacuum photo-triodes (VPTs), Hamamatsu (type number R11375 MOD3)

(3) Vacuum-Photo-Tetrodes (VPTTs), Hamamatsu (type number R11375 MOD)

3.1.1 Avalanche Photo-diodes (APDs), General discription

APDs are highly sensitive semiconductor devices which use the photoelectric effect to convert incident light into a charge. The performance of the APD is dependent on two factors: quantum efficiency and total leakage current. Quantum efficiency means how well incident photons are absorbed and then produced primary charge carriers. The quantum efficiency of the APD is about 80 percent. APD is a silicon based semiconductor device which consists of one Anode, one Cathode and a pn junction. The pn junction consist of 'p' and 'n' regions doped by positive and negative charge carriers respectively. Electron-hole pairs

are created by the ionisation of energetic electrons in the depletion region as shown in the figure (3.1).

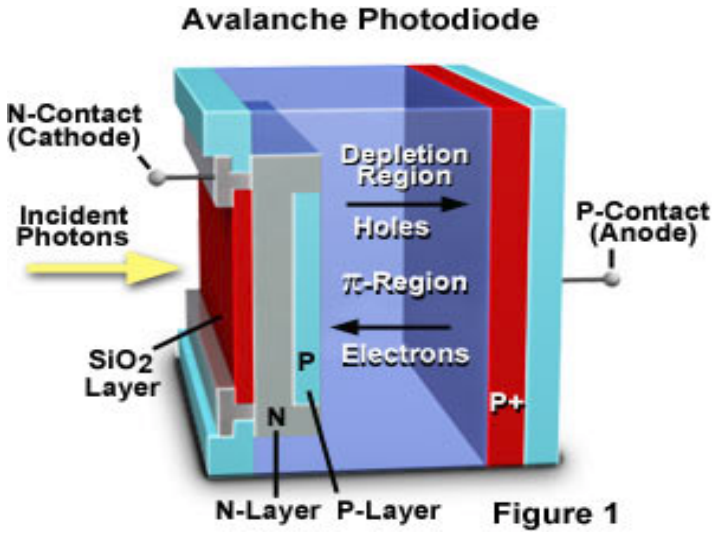

Figure 3.1: A typical avalanche photodiode, First of all high energy incident photons are passing through the silicon dioxide layer and than crossing the 'p' and 'n' layers. Finally they are entering into the depletion region where they are exciting free electrons and holes which are then directed towards the cathode and the anode terminals of the APD respectively [21]

.

Large Area Avalanche Photo-diodes (LAAPDs), Hamamatsu (type number S11048 (X)) for the barrel, backward and forward part of the EMC

To maximize the signal effect as much as possible, Large Area APDs (LAAPDs) have been developed. LAAPDs will be used to deal with the barrel part of the EMC, the backward endcap of the EMC and the forward end-cap of the EMC of the target spectrometer.

The operation on the LAAPD is dependent on its gain factor and the gain factor is also dependent on the temperature. That means how gain factor will change at the room temperature as well as at an operating temperature T -25^{o}C. Expected event rates for the barrel part of the EMC is 10kHz to a maximum of 100kHz. Therefore Large Area Avalanche Photo-diodes (LAAPDs) are more efficient for the barrel part of the EMC. Different sizes of the crystals have been placed at different angles in the barrel part of EMC. Lead tungstate scintillating crystals (PWO-II) have a typical geometry of $(200mm \times 25 \times 25)$ which leads us to develop a shape of a LAAPD. Two LAAPDs will be directly attached with the individual crystal.

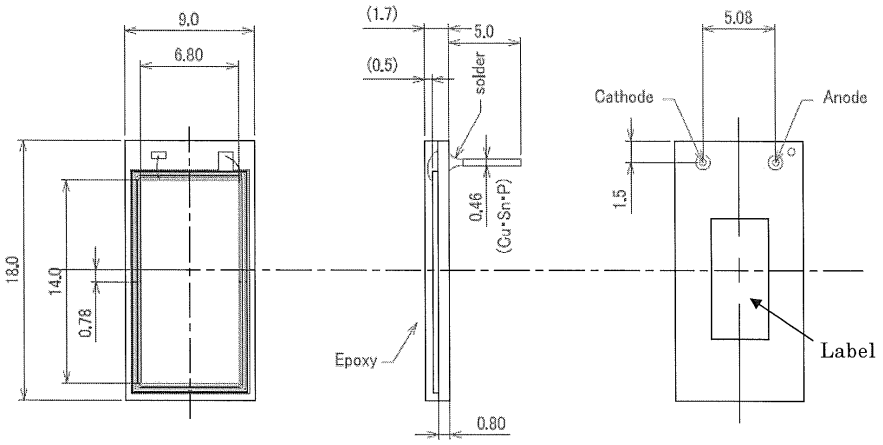

Figure 3.2: A silicon avalanche photo-diode type number S11048(X) [22] has been designed by Hamamatsu. This design is especially made to readout the barrel part of the EMC crystals. It has an active area of 14.0×6.8 mm. It consist of one anode, one cathode and a pn junction. It has a wave length of maximum response 580 nm. It has a width of 9.0 mm and a length of 18.0 mm. The central sensitive part of photocathode has diameter of 6.80 mm. Its operating temperature is varying between -20^o C to $+60^o$ C and storage temperature is varying between -20^o C to $+80^o$ C.

3.1.2 Vacuum photo-triodes (VPTs), Hamamatsu (type number R11375 MOD3) for the forward endcap of the EMC

Different types of the photodetectors are tested and analyzed to detect light from the forward endcap Lead tungstate scintillating crystals (PWO-II) of the EMC. The outer part of the forward endcap EMC will be equipped by the LAAPDs because of the low radiation and the central part will be equipped by Vacuum Photo Triodes (VPTs) or by Vacuum Photo Tetrodes (VPTTs) because of higher event rates up to 500 KHz. VPTs are based on one dynode and can work in a strong magnetic field without loosing so much gain. Quantum efficiency of the VPT is round about 20 to 25 percent. Other types of photodetectors will not be used because of the presence of strong magnetic field B. New types of VPTs are under construction and will be tested soon when available. Different types of VPTs have been manufactured at Research Institute Electron, St. Petersburg, Russia and Hamamatsu, Japan. These types are tested and analyzed for the forward endcap of the EMC. The latest version (R11375 MOD3) of the VPT is manufactured at Hamamatsu and shown in the figure (3.3).

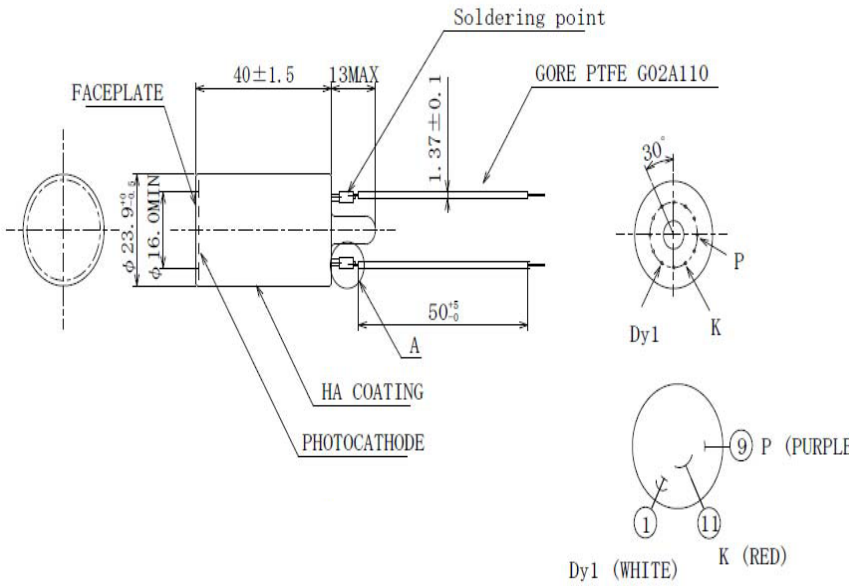

Figure 3.3: Hamamatsu triode of the type R11375 MOD3 [22] consist of one dynode, one anode and one cathode. The Bialkali material has been used to build this photocathode and the window material consist of UV transmitting glass. It has a wave length of maximum response 420 nm. It has a diameter of 23.9 mm and a length of 40 ± 1.5 *mm. The central sensitive part of the photocathode has diameter of 16.0 mm. The maximum supply voltage between the anode and the cathode is 1000 V and the maximum supply voltage between the anode and the last dynode is 500 V. Its operating temperature is varying between* $-30^{o}C$ *to* $+50^{o}C$ *and the storage temperature is varying between* $-80^{o}C$ *to* $+50^{o}C$*.*

3.1.3 Vacuum-Photo-Tetrodes (VPTTs), Hamamatsu (type number R11375 MOD) for the forward Endcap Of the EMC

Vacuum Photo-Tetrode (VPTT) is also another option to dectect light from the forward endcap of the EMC. Several types of the VPTTs have been manufactured at the Research Institute Electron, St. Petersburg, Russia and at Hamamatsu, Japan. But the latest version (R11375 MOD) [22] of the VPTT is built at Hamamatsu for the $\bar{P}$ANDA project and shown in the figure (3.4).

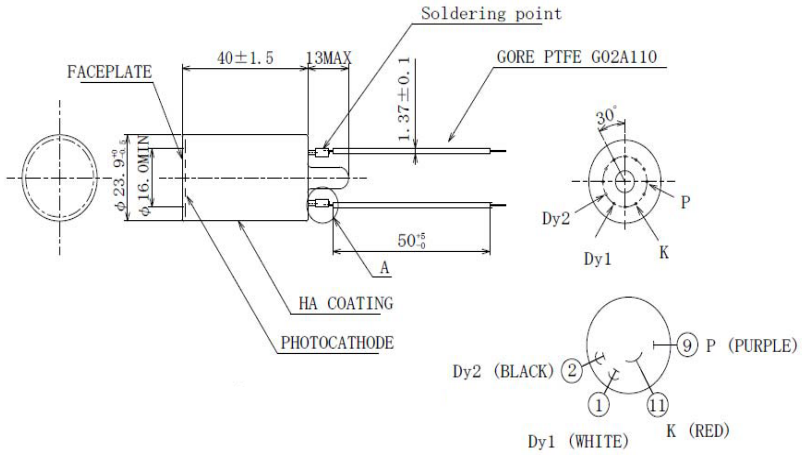

Figure 3.4: Hamamatsu tetrodes of the type R11375 MOD [22] consist of two dynodes, one anode and one cathode. As it consist of two dynodes it has more gain factor as compared to VPT. The Bialkali material has been used to build this photocathode and the window material consist of UV transmitting glass. It has a wave length of maximum response 420 nm. It has a diameter of 23.9 mm and a length of 40 ± 1.5 *mm. The central sensitive part of the photocathode has a diameter of 16.0 mm. The maximum supply voltage between the anode and the cathode is 1000 V and the maximum supply voltage between the anode and the last dynode is 500 V. Its operating temperature is varying between* -30^oC *to* $+50^oC$ *and the storage temperature is varying between* -80^oC *to* $+50^oC$*. Its weight is 14g.*

3.2 Photomultiplier Tubes (PMTs)

Photomultiplier tubes (PMTs) are basically very sensitive detectors and also called vacuum tubes which are made to detect light. These detectors can detect light in the range of ultraviolet, visible and near infrared region of the electromagnetic spectrum. The main function of the PMT is to increase the strength of electrons with low noise and with higher frequency response. Such properties make its importance in the field of nuclear and particle physics, medical imaging, medical diagnostics and astronomy.

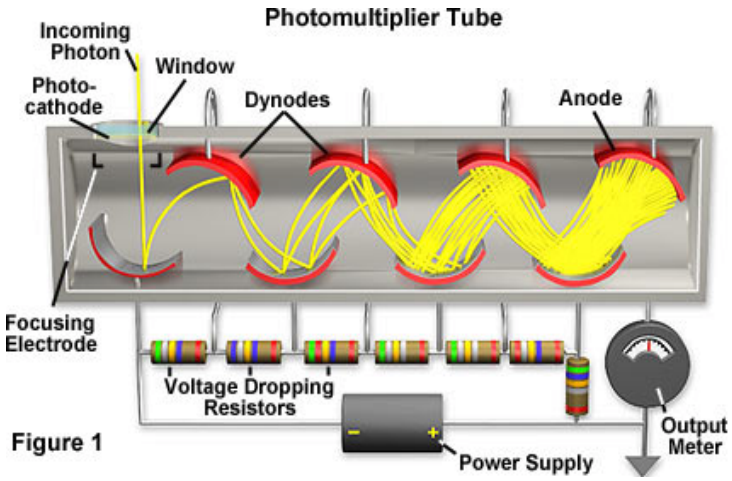

Figure 3.5: shows a complete function of a typical photomultiplier tube. An incoming photon hits on the surface of the photocathode and produces a primary electron which is then accelerated towards the first dynode, where it interacts with other electrons and produces secondary electrons which are further accelerated towards a series of dynodes and produces more and more electrons, which are finally collected at the anode [23].

A PMTs consists of a glass tube with high vacuum inside containing photocathodes, dynodes and anode. Photocathodes are made of photosensitive materials to eject the electrons. Dynodes are basically electron multipliers and the anode is used to collect electrons and produce final signal. First of all a high negative voltage is applied to the photocathode. An incident photon strikes with the surface of the photocathode and produces a primary electron by the photoelectric effect. The primary electron is directed and accelerated towards the first dynode with the help of an electric field. When a primary electron hits the surface of first dynode, it transfers some of its energy to the electrons of the surface and produces secondary electrons. These secondary electrons are further accelerated and directed towards a series of dynodes and produces more and more electrons. Then these electrons are concentrated towards the anode as shown in figure (3.5). Finally the current is collected from the anode for analyses.

The PMT (Hamamatsu) type number R5070 with voltage divider E 2924-500 (base) is shown in the figure (3.6) is used to compare results with other photodetectors to test the linearity of the LNP-PreAmp. But it will not be used in the $\bar{P}$ANDA experiment because of the high count rates. Photo detectors of the types Hamamatsu APD S11048(X) (Rectangular), Hamamatsu triode R11375 MOD3 and Hamamatsu tetrode R11375 MOD will be used in the $\bar{P}$ANDA experiment.

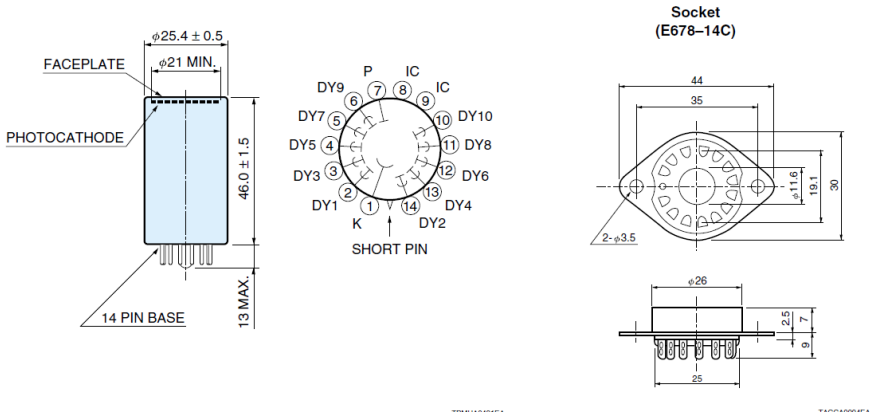

Figure 3.6: The PMT (Hamamatsu), type R5070 [24] with voltage divider E 2924-500 (base), diameter of 25 mm is used during the test of linearity of the LNP-PreAmp at Basel University to get good results and to compare these results with other types of the photodetectors (APD, VPT, VPTT)

3.3 General Characteristics

Model/Type No.	Photo detector	Typical Gain	Storage Temp ℃	Spectral Response λ(nm)	Typical Quantum Efficiency	Operating Voltage
R5070A	PMT	4.3 $\times 10^5$	-80 to +50	300 to 900	20 %	1000 V
S11048(X)	APD	50	-20 to +50	320 to 1000	70%	typ∼400 V
R11375MOD3	VPT	8	-80 to +50	300 to 650	20%	750 V
R11375MOD	VPTT	25	-80 to +50	300 to 650	20%	750 V

Table 3.1: shows some of the important characteristics of the different types of photodetectors (APD, VPT, VPTT) which will be used in the $\bar{P}$ANDA experiment, except PMT (R5070A). PMT (R5070A) is used only during the tests at Basel University and compare these results with other types of the photodetectors (APD, VPT, VPTT).

Chapter 4

General Readout Scheme for the LNP (Low Noise/ Low Power) Pre-amplifier

4.1 Introduction

A pre-amplifier is an electronic device used to amplify weak electronic signals. Pre-amplifiers are placed close to the photo detectors to reduce noise effects and interference effects. Currently in the market, the available preamplifiers achieve low noise at the expense of relative high power consumption. To readout the $\bar{\text{P}}$ANDA electromagnetic calorimeter (EMC), it is needed to develop special types of pre-amplifiers that can amplify signals with low noise and with low power consumption.

For that purpose different types of complementary low noise and low-power (LNP) discrete charge sensitive pre-amplifier have been developed. Some of them will be used to read out large area avalanche photo-diodes (LAAPD), vacuum-photo-triodes (VPTs) and vacuum-photo-tetrodes (VPTT). All these photodetectors (LAAPDs, VPTs, VPTT) will be attached to the end faces of the lead tungstate scintillating crystals (PWO-II) of a typical geometry (200mm x 25mm x 25mm) which give much better results in strong magnetic field as compared to the photomultiplier tubes (PMT). The barrel part and the backward endcap of the EMC will be equipped with LAAPDs because of the low radiation as compared to the forward endcap of the EMC. The central part of the forward endcap EMC will be equipped with VPTTs because of high radiation level and the outer part will be equipped with LAAPDs.

The LNP-preamplfier linearly converts the charge signal into a positive voltage pulse which is transmitted via a 50 Ohm line to the subsequent electronics [22].

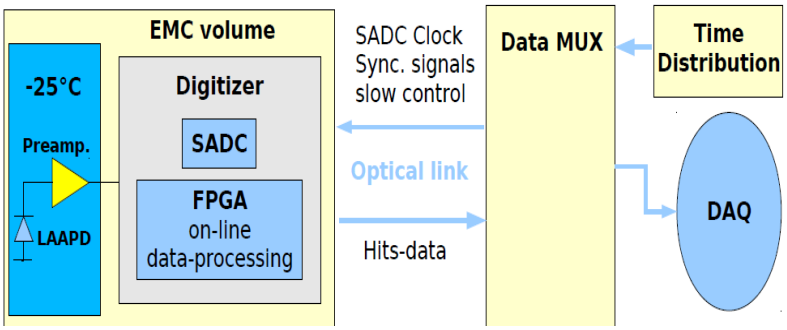

Figure 4.1: A sketch of the desired readout Scheme for the $\bar{P}$ANDA EMC [27]. It includes digitizer, data concentrator (DCON) and data-acquisition (DAQ) modules. The digitizer module consists of SADCs and FPGA and it is located inside the EMC volume, SADCs are used for continuous digitization of the preamplifier signals and an FPGA for online data processing. Then data is trasferred to the DMUX module, located outside the $\bar{P}$ANDA EMC [27]. The function of the DCON module is to collect data from different digitizers and start data pre-processing ,e.g. on-line pile-up recovery. Pre-processed data are sent to the DAQ for the identification of the particles and shower detection etc. The DAQ combines EMC data with all other $\bar{P}$ANDA subdetectors and only complete events will be selected by selection criteria [27]

.

4.2 Development of the LNP-preamplifiers at Basel university for $\bar{P}$ANDA experiment

Different versions of the LNP-preamplifiers have been developed at Basel university and the process is still going on. The latest model SP883d belongs to the family of the LNP-preamplifiers originally designed for the APDs with a capacitance of up to 500pF (i.e. two paralleled Hamamatsu S8664-1010 or S11048) [22].

The LNP-preamplfier must contain some of the key factors. For example: It must be low noise/ low power, low overall cost/easy operation, integration of a low power loss HV bleeder for operation in cooled areas and the flexible design for different photodetectors APD/VPT/VPTT [22]. The latest version of the LNP-preamplfier SP883d is developed in 2010 and the family members of the LNP-preamplfier are shown in table 4.1.

Model/Type No.	Photodetector	HV_max.	Description
SP883a	APD 10x10mm	500V	APD single channel family, 18x48mm, PCB: 0.8mm
SP883a01	VPT short glass	1000V	With round shaped filter PCB, soldered to tube
SP883a02	APD 10x10mm	500V	compensation for up to 500pF
SP883a02_1000V	APD rectangular	1000V	With 1000V capacitors (Bias APD: ca. 650V) compensation for up to 500pF
SP883a03	APD rectangular	1000V	Low gain, Low Bias HV filter resistor
SP883b	APD 10x10mm	500V	quad channel (Proto60), 46x46mm
SP883c	VPT metal (Ham)	1000V	without onboard HV divider, PCB: 4-Layer 1.6mm
SP883(c)d		1500V	Prototyp: Umbau von SP883c auf Funktion v. "d"
SP883d		1500V	Combi family (APD/VPT/VPTT), "stamp-format", 2 PCB à 18x28mm, with onboard HV-Divider
SP883d_VPT(Ham)	VPT glass, (Ham)	1500V	with onboard HV-Divider for VPT (750V)
SP883d_VPTT(Ham)	Tetrode glass, (Ham)	1500V	with onboard HV-Divider for VPTT (750V)
SP883d_VPTT(RIE)	RIE	1500V	with onboard HV-Divider for RIE VPTT's (1200V)
SP883d_APD	APD rectangular	450V	3MΩ-filter for 2 APD-Bias, mit 100pF*compensat.

Table 4.1: This table shows the family of LNP-preamplfiers, developed at Basel University. The latest version SP883d is developed in 2010 and then further subdivided into different versions [22].

100pF*-compensation value is implemented (designed for VPT/T). This may cause to a little slower rise time, but better stability, especially at lower temperature. Also used for LowGain-APD (SP883a03). Standard value for APD with +/-6V is 47pF, for +8V/-2V 100pF.

Note: type number key, Example SP883d01_APD:

SP; Schematic Plan

883 Projectnumber Electronics Lab Physics Basel for the Panda EMC Preamp

d Model/Type/Version
01 Revision/Version 1 1
_APD variante/adaption
(Ham) Hamamatsu

4.3 LNP-preamplifier for the barrel part of the EMC to readout LAAPDs

In 2006, Basel university (physics department) has developed a special type of a low noise/ low power charge sensitive preamplifier (LNP-preamplifier) to readout LAAPDs for the barrel part of the EMC and it gives much better results. Two types belong to the family of the LNP-preamplifier SP883a and SP883b. They were developed for the barrel part of the EMC (proto 60) to readout single LAAPD per crystal. But these two types (SP883a,SP883b) are no more in use including the another type SP833a01. PFEL (GSI) ASIC is working on (proto 120) and developed some special types of the preamplifiers to readout two LAAPDs per crystal for the barrel part of the EMC.

The latest ASIC version 1.4 is shown in the figure (4.2). This version is produced and tested with the complete functionalities but yet no successful tests are made within the EMC prototype [28].

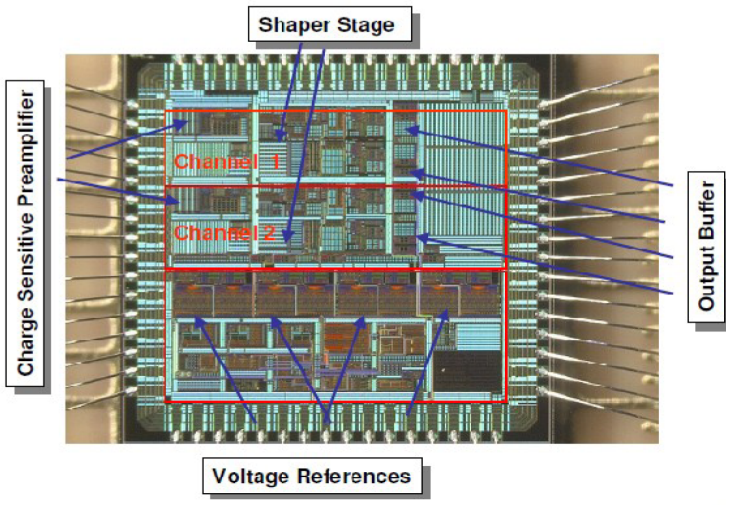

Figure 4.2: The APFEL-ASIC has two equvalent analog channels, each channel consisting of a charge sensitive preamplifier, a shaper stage and the differential output drivers[28]. Digital part: programming of the chip

.

4.4 Circuit diagram of the LNP-preamplifier to readout LAAPDs for the backward endcap EMC

To readout the backward endcap of the EMC, LAAPDs will be directly attached with the lead tungstate scintillating crystals (PWO-II). LAAPDs will convert scintillating light into an electric charge and the LNP-preamplfier will convert charge signals into a positive voltage pulse.

To raise the performance of LNP-preamplfier version SP883a02 (18x48mm) for the backward endcap of the EMC, it is further developed and made some modifications which are as folows.

J-FET (BF862, NXP Semiconductors) are combined with low power and high speed current- feedback operational amplifer. The specification is given below [22].

Rise-time

Cd = 82 pF: 10ns

Cd = 270 pF: 18ns

Feedback time-constant: $25\mu s$

Gain: 0.5 V/pC at 50 Ohm termination

- Maximum single pulse input charge: 4 pC (±6 V supply)
- Maximum 100 kHz burst input charge: 1 pC (±6 V supply)
- Maximum countinuous 100 KHz input charge: 8 pC (±6 V supply)

The single channel LNP-preamplfier version: PCB size (48 x 18) mm^2

The LNP-preamplfier (Version SP 883a02) has the ability to handle detector capacitances from 0 pF to 500 pF. This is large enough to deal with LAAPDs. LAAPDs can be connected directly with LNP-preamplfier or by shielded cable.

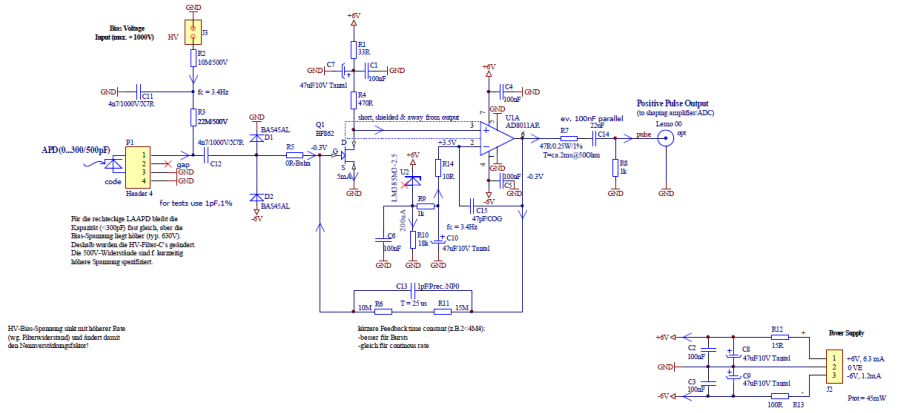

Figure 4.3: Circuit diagram of the LNP-preamplifier revision 2 (SP 883a02) to readout LAAPDs for the backward endcap of the EMC [22]

.

The circuit diagram of the LNP-preamplfier is shown in figure 4.3. This circuit diagram is basically divided into two main parts called high voltage component side (left side of the figure 4.3) and a low voltage component side (

Right side of the figure 4.3) The high voltage component side consists of APD bias voltage input (max +500V). It is a low-pass (RC) filter consisting of a 10 $M\Omega$ resistor and a 4.7 nF high voltage (HV) capacitor which results in a cut-off frequency of 3.4 Hz. Afer passing through the low-pass filter, the bias voltage follows the path via 22 MΩ resistor and moves towards the cathod terminal of the APD. The anode terminal of the APD is grounded. This (C 12) 4.7 nF high voltage capacitor is used to decouple the gate of J-FET to block the DC signals and allow only AC signals to pass the gate. The low voltage component side consists of the low noise J-FET of the type BF862. It is specified with input voltage noise density of 0.8 nV/sqrt (Hz) at 100 KHz [22].

The J-FET input capacitance is 10 pF and the forward transconductance is 30 mS at drain source current (I_DS) of 5 mA [22]. Two low leakage silicon diodes of the type BAS45AL are used to protect the gate of the J-FET from over voltages as shown in the figure (4.3).

Then input signals follow the path and reaches the operational amplifier of the type AD8011AR. The input voltage noise density of this amplifier is around 2 nV/sqrt (Hz) at 10 kHz which is suitable for such a low noise design. The operational amplifier also gets high frequency compensation because of the combination of the capacitor C 15 (47 pF) and the resistor R 14 (10 Ohm). The output of the operational amplifier is DC coupled by a feedback network (1 pF // 25 Meg Ohm) and also AC-coupled by a 1 μF capacitor and a 47 Ohm series resistor to the output of the LNP-preamplifier [22].

4.5 Circuit diagram of the LNP-preamplifier to readout LAAPDs for the forward endcap of the EMC

For the forward endcap of the EMC, the expected event rates are up to 500 kHz per crystal and the magnetic field would be up to 1.2 T. Therefore the VPTT photo detector will be used at the core of the forward endcap EMC and at the surrounded area, LAAPDs will be used because of comparatively low event rates and the magnetic field. So far, the LNP-P version SP883a03 has been developed to read out LAAPDs for the forward end cap EMC with lower gain.

SP883a03 (18x48mm) is based on the the same PCB as Version SP883a02, developed at Basel university, but with some different components to have lower gain and lower filter resistance (Bias-HV dependency) for the Proto 192. Its performance and specification is given below [22]:

Filter:

R2 is now 50kOhm instead of 10MOhm and

R3 is now 100kOhm instead of 22MOhm

Gain:

C13 is now 2.7pF instead of 1pF

R11 is now 0 Ohm instead of 15MOhm

Compensation: C15 is now 100pF instead of 47pF

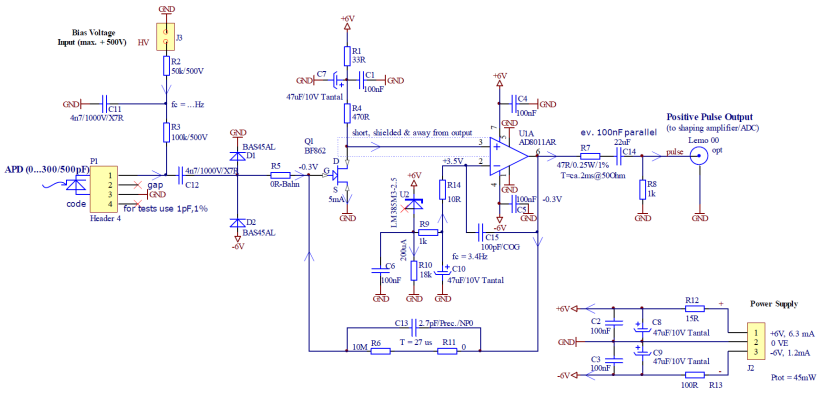

Figure 4.4: Circuit diagram of the LNP-preamplifier version (SP883a03) to readout LAAPDs for the forward endcap of the EMC [22]

.

4.6 LNP-preamplifier to readout VPT/ VPTT for the forward endcap of the EMC

An LNP-preamplfier of version SP883d (18x28mm) has been developed to readout VPTT (Hamamatsu) for the forward endcap of the EMC. This is a latest version SP883d from the family of LNP-preamplifiers. $\bar{\text{P}}$ANDA scientists are also working on VPTT RIE (Research Institute Electron) from Russia which has different configuration. But in the future, Scientists believe to concentrate on VPTT (Hamamatsu). The circuit diagram is shown in figure 4.5.

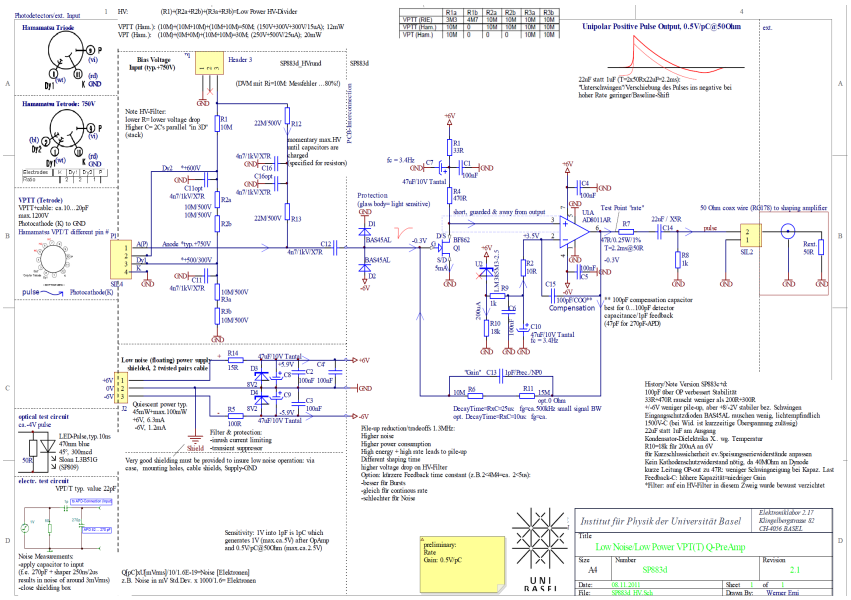

Figure 4.5: An overview of the latest LNP-preamplifier version (SP883d) to readout VPT/ VPTT for the forward endcap of the EMC [22]

.

A low power high voltage divider which consists of capacitors and resistors has been used to provide an external high voltage to the photo detectors (VPT/VPTT) as shown in the figure 4.5. In case of the APD (Hamamatsu), only low pass (RC) filters have been used.

The difference between the versions of SP883d PS (VPT/VPTT) is shown in the table 4.2.

Photodetectors	(R1)	(R2a + R2b)	(R3a + R3b)	Total resistance
VPTT (Ham)	(10MΩ)	(10MΩ + 10MΩ)	(10MΩ + 10MΩ)	50MΩ
VPT (Ham)	(10MΩ)	(0MΩ + 0MΩ)	(10MΩ + 10MΩ)	30MΩ

Table 4.2: This table shows the difference between the versions of the LNP-preamplifier type SP883d to readout VPT (Hamamatsu) and VPTT (Hamamatsu) for the forward endcap of the EMC.

Chapter 5

Linearity test of the Low Noise/Low Power (LNP) preamplifier

5.1 Introduction

The University of Basel (Physics department) is collaborating in the PANDA project in particular on the design and test of special preamplifier circuits for the readout of the electromagnetic calorimeter (EMC) which is a major sub-unit of the detector. To readout PANDA EMC, special types of (LNP) pre-amplifiers are developed as discussed in chapter 4.

Linearity of the measurement devices is an important feature in experimental physics. After the development of the LNP-preamplifier, it is important to test its linearity. First our need to understand how EMC works and why it is necessary to have a linear response of the LNP-preamplifier. For example, if two photons of energy 1 GeV are moving with interval of 500 ns towards the lead tungstate scintillating crystals (PWO-II) of EMC, these photons will produce secondary particles, that interact with other particles and makes an electromagnetic shower as shown in figure (5.1). As every crystal is equipped with photo detectors and preamplfiers, they give individual results, also shown in figure (5.1).

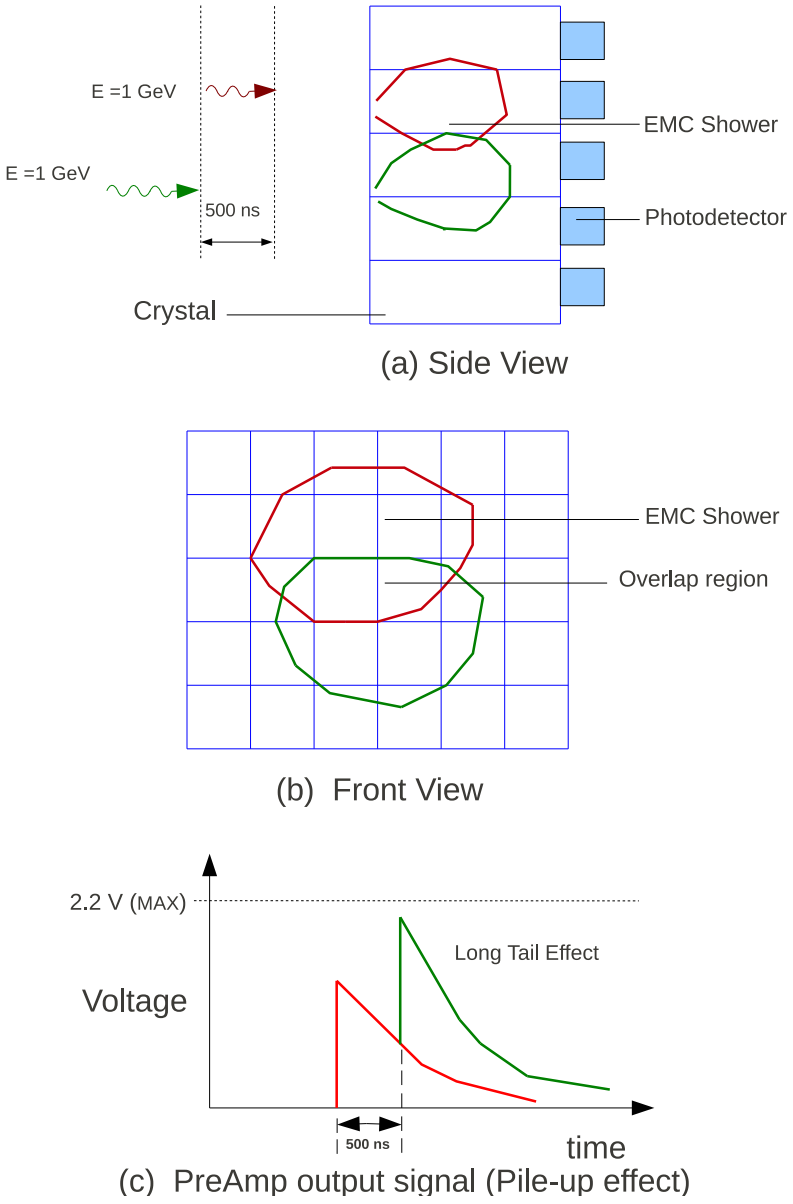

Figure 5.1: Figure (a) shows a side view of the PWO-II crystals, Two photons are hitting the surface of the PWO-II crystals and producing EMC showers, which are detected by the photo detectors. Panel (b) shows a front view of the PWO-II crystals and the overlaping region of the EMC showers. Panel (c) shows it is output signal of the Preamplifier from the overlap region, As the second pulse lies on the tail of the first pulse called long tail effect.

Pile-up effects

High counting rates and long signal tails can lead to the interfering effects between the pulses. These effects are called pile-up. There are two types of pile-up called long tail effect and peak pile-up effect [29]. Long tail effects can occur because of the superposition of the pulses on the long duration as shown in figure (5.1). Peak pile-up effects can occur if the two pulses overlap each other in time in such a way that they seems to be a one pulse.

This effect can be reduced by keeping the total width of pulses as small as possible [29]. But the problem is that, when we are keeping the pulse width small, the noise level is increased. Still it needs more work to solve this problem in an optimal way.

Temperature Effects

Inside the $\bar{\text{P}}$ANDA target spectrometer, the inorganic scintillator crystals (PWO-II) , photodetectors and preamplifiers will be cooled down to a temperature of -25°C to get the maximum light output.

5.2 Linearity of the components

Inorganic scintillators are suitable for detection of gamma-rays, high energy electrons and positrons, because they are very dense materials with high atomic number Z, and incoming particle looses enough energy after interacting with them. Therefore for the $\bar{\text{P}}$ANDA target spectrometer, the inorganic scintillator crystals (PWO-II) has been chosen because of their high density and high Z, high resolution, good light output and its fast decay time of ∼30 ns. Together this promises good resolution in energy, space and time.

The linearity of the components to be used for the $\bar{\text{P}}$ANDA experiment is described in different levels and shown in figure (5.2).

Level I

A high energy gamma hits the PWO-II crystal and produces an electromagnetic shower with scintillation light as output. The produced output signal shall be directly proportional to the energy of the incoming photon.

$$\triangle E = kN_{ph} \tag{5.1}$$

where
$\triangle$E = Energy deposit of incident gamma
N_{ph} = Number of scintillation photons
k = proportionality constant

Level II

Scintillation light emitted from the PWO-II crystals will be detected by the photodetectors as discussed in chapter 3. An incident scintillation photon hits the surface of the photocathode and with a probability given by the quantum efficiency a photoelectron is produced because of the photoelectric effect.

$$N_{p.e} = Q_{qe} N_{ph} \tag{5.2}$$

where
$N_{p.e}$ = number of photoelectrons
Q_{qe} = quantum efficiency of charged particle
N_{ph} = number of photons

Level III

Photoelectrons are accelerated towards the anode if the photodetector where a bunch of electrons are collected at the anode terminal and gives the charge which is directly proportional to the number of photoelectrons.

$$Q = gN_{p.e} \tag{5.3}$$

where
$N_{p.e}$ = number of photo electrons
Q = charge
g = gain factor

Level IV

After the detection of the light, preamplification of the signal is important. For preamplification, different types of charge sensitive low noise/ low power (LNP) preamplifiers have been developed, as discussed in chapter 4. The output voltage of the preamplifier is directly proportional to the input charge given to the preamplifier.

$$V = kQ \tag{5.4}$$

where
Q = Input charge given to the preamplifier
K = proportionality constant
V = Output voltage of the preamplifier

Level V

The shaper is used to reshape the pulse signals into a standard shape and also to fix their widths.

Level VI

The shaped signal is sent to the ADC (Analog-to-Digital Converter) with the coaxial cables. The ADC converts the analog signal to an equivalent digital form.

It is necessary for the stability of the signals that the preamplifier capacitance must be larger then the source capacitance at the input i.e the detectors, cables etc [20]. The noise of the preamlifier has also effects on the resolution of the

detector. This noise can be reduced by placing the preamplifier as close as possible to the detector and minimize the input capacitance to the preamplfier.

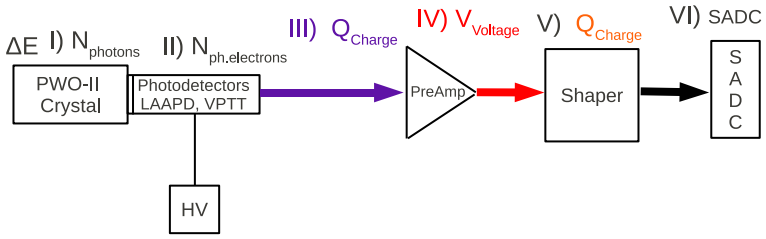

Figure 5.2: shows different levels of signal processing. All of the mentioned components will be used for PANDA experiments and their performance should be linear. Our work is to test the linearity of the LNP-preamplifier.

5.3 Linearity tests of the LNP-preamplifier

The linearity is dependent on some of the factors $K(N, Q)$ that should remain constant during the experiment and described in equation 5.5. Some of the other factors like temperature, radiation, presure, and humidity are kept constant as well as possible or assuemed to be constant during the tests.

$$V = k(N, Q)Q + V_0 \tag{5.5}$$

$$\triangle V = k(N, Q)Q \tag{5.6}$$

where
$\triangle$V = output voltage from the LNP-preamplifer
K = proportionality constant
N = number of input count rates (events)
Q = input charge

Linearity of the components are discussed in section 5.2 and details are shown in figure 5.2. Our work is to test linearity of the LNP-preamlifier. As output voltage of the LNP-preamplifier is directly proportional to the input charge given to the preamplifier, the output voltage must be linear with respect to the input charge. Linearity of the LNP-preamlifier is tested by several methods which are described as follows.

(1) Double burst linearity test of LNP-preamplifier

This test is performed to test linearity of the LNP-preamplifier. For example: when two bursts hit the surface of PWO-II crystals and produce EM showers

which may overlap as discussed in section 5.1. Therefore to test linearity of the LNP-preamlifier in such a situation, two pulses are generated with fixed amplitudes and with a delay varying gradually between 0.5 μs to 10μs as an input signal to the LNP-preamplifier to test its linearity.

These tests are performed in two different ways.

(1) Linearity test of the LNP-preamplifier without photodetector connected.

(2) Linearity test of the LNP-preamplifier with photodetector connected.

(2) Amplitude linearity test of the LNP-preamplifier

In this test, amplitude of the input signals given to the LNP-preamlifier is varying up to different levels to test its linearity and performed as follows.

(1) Amplitude linearity test of the LNP-preamplifier with photodetector connected.

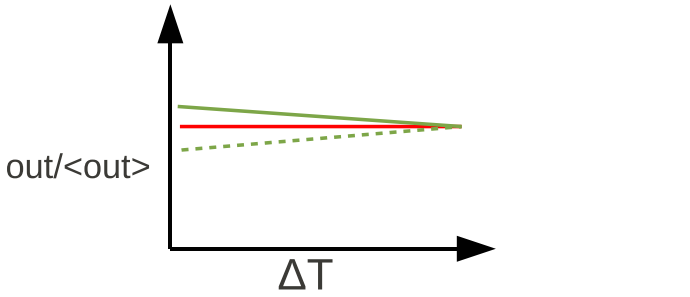

(a) LNP-PreAmp linearity for double bursts

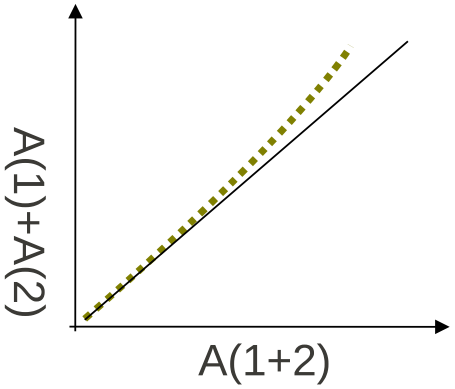

(b) LNP-PreAmp amplitude linearity

Figure 5.3: These figures (a) and (b) are just drawings. (a) shows double burst linearity graph of the LNP-preamplifier, The x-axis shows the delay between the two bursts varying between 0.5 μs to 10 μs and the y-axis shows normalized output signal as a function of delay between two bursts. Red and green solid lines (data points) shows first and second bursts respectively. Dotted green line shows another possibility of the distribution of second burst. (b) shows amplitude linearity graph of the LNP-preamplifier, the solid line shows the sum of the two individual events is linear with respect to the combined event and dotted line shows if its not linear

.

5.4 Linearity test of the LNP-preamplifier without photodetector connected

As discussed earlier, the double burst linearity method is used to test linearity of the LNP-preamlifier and it is further divided into two cases. The first method is to test the linearity of the LNP-preamplifier without photodetectors which is further divided into two different cases.

(1) Linearity test of the LNP-preamplifier by using a standard pulse generator.

(2) Linearity test of the LNP-preamplifier by using the LED driver based on

an FPGA (Field Programmable Gate Array).

5.4.1 Linearity test of the LNP-preamplifier by using a standard pulse generator

In this case, a linearity of the LNP-preamplifier is tested by using a 14 bit Tektronix AFG 3252 (Arbitrary/Function Generator) which has maximum analog band width of 240 MHz and a sampling rate of 2 GSamples/s. It is used because of its special features and benifits. The idea was that to generate two pulses with delay varying gradually between 0.5 μs to 10μs to test linearity of the LNP-preamplifier. The $\bar{\text{P}}$ANDA experiment, with expected event rates up to 1 MHz.

The test setup is illustrated in figure (5.4) and it consists of following components.

14 bit Tektronix AFG 3252 (Arbitrary/Function Generator)

Passive Splitter – optimized for 50Ω impedance

LNP-preamplifier SP883a03 ≪low gain≫ with+/-6V linear power supply

SADC: (Sampling Analog to Digital Converter) 12-bit, 500MS/s, 500MHz, 4ch. Struck SIS3350

VME Interface and Controller

Working Principle

The working principle is shown in figure (5.4). Two pulses are generated from the generator and split into two different paths by using a passive splitter. After splitting, the first signal sent directly to one of the channels of the SADC and the second signal is passing through the LNP-preamplifier and then directed towards the other channel of the SADC.

The SADC consists of four channel digitizer recorder with a sampling rate of up to 500 MS/s (for the individual channel) and with a resolution of 12-bits. The SADC is used for digitisation of the preamplifier signals.

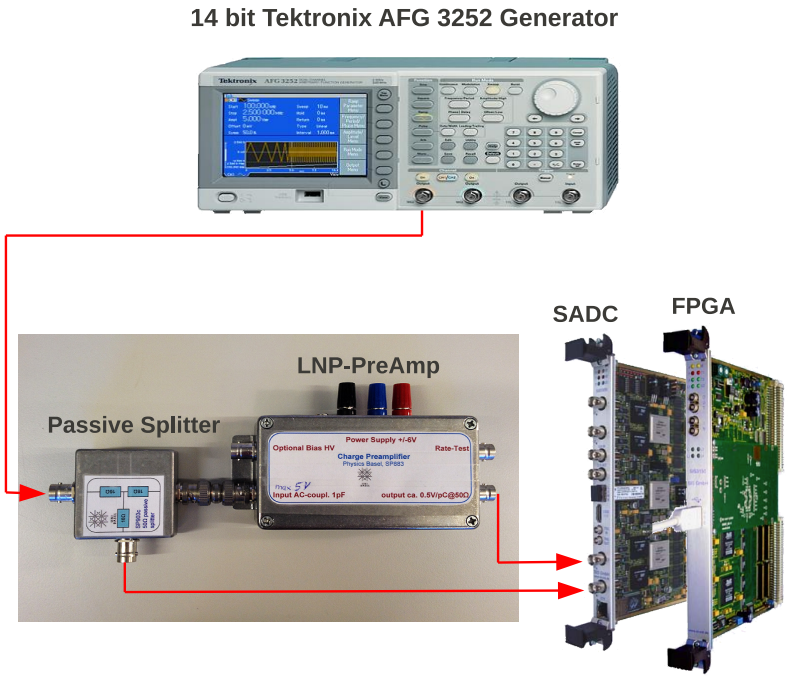

Figure 5.4: shows test setup to test double burst linearity of the LNP-preamplfier of the type SP883a03 by using 14 bit tektronix AFG 3252 function generator. A passive splitter is used to split input generator signals. The SADC is used for the digitisation of the LNP-Preamplifier signals and an the FPGA is used for an on-line data processing.

Passive splitters

During the test, passive splitters are used to split the signal into two different paths because of their special benefits. For example: they keep original shape of the signal same after splitting and no power is required to run them.

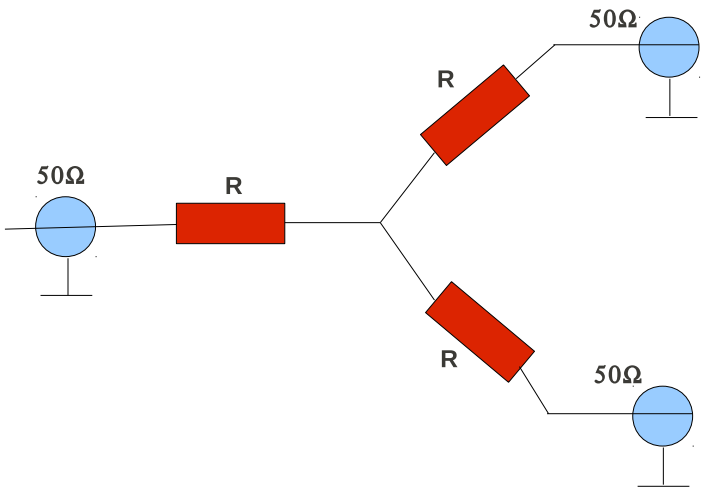

Figure 5.5: It shows Passive Splitter – optimized for 50 Ω impedance.

Beam parameters

In this case, two pulses are generated from the generator with delay varying gradually between 0.5 μs to 10μs and the interval between two events is 500 μs. The total number of events generated from the generator is 30, 000 / measurement and every event is sampled 8000 times. The distance between two events is 1 ms or 1 kHz and the distance between the two samples is 2 ns or 500 MS/s. Two pulse bursts (red and green) are also shown which are passing through the individual event.

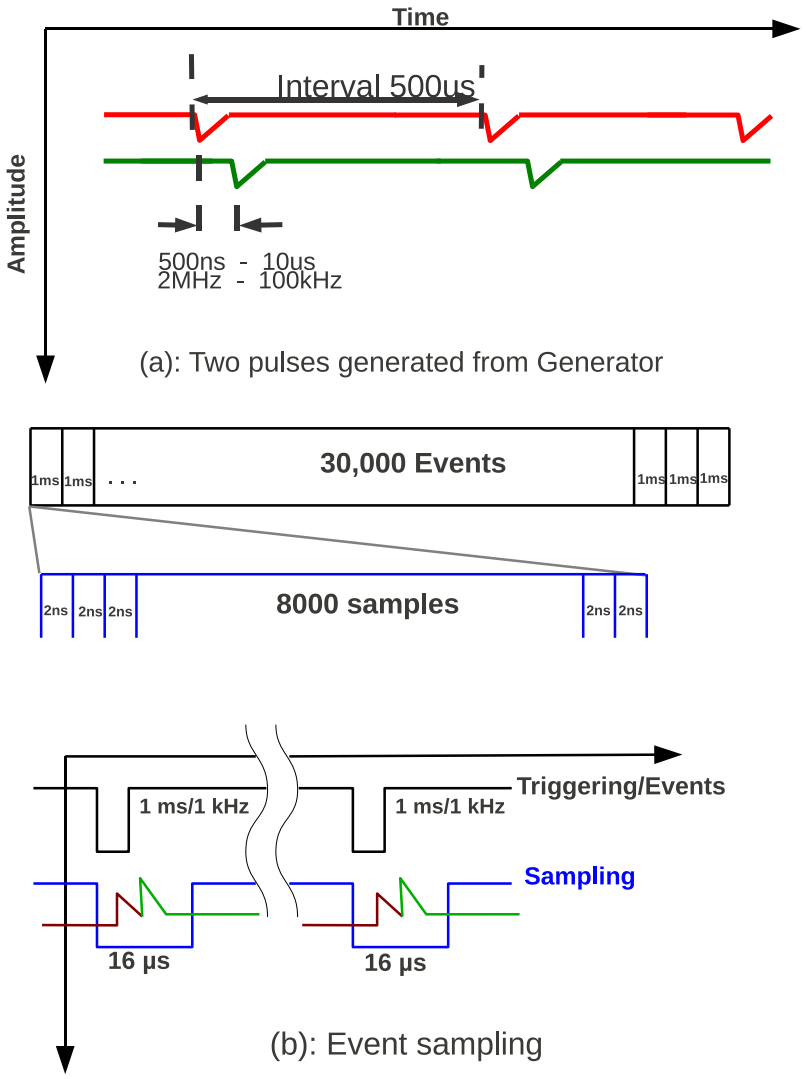

Figure 5.6: (a): Red line indicates first burst and green line indicates second burst respectively. (b): It shows beam parameters and also two pulse bursts (red and green) which are passing through the individual event.

Test Results

In this case, amplitude of the LNP-preamlifier signals are adjusted up to different levels 100 mV, 200 mV, 300 mV with the help of the input generator signals and test results are shown in figures (5.7), (5.8) and (5.9) respectively.

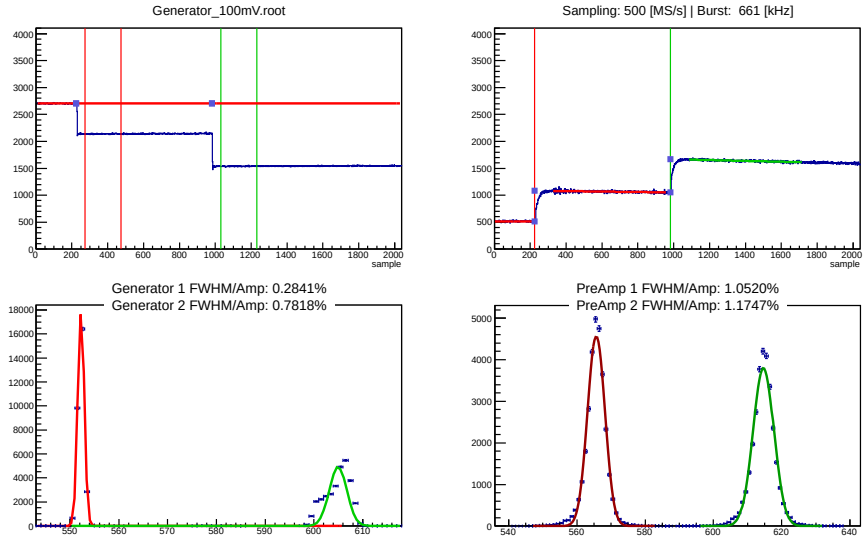

Figure 5.7: In this figure, the upper row shows a single event meaasured by the SADC with a sampling rate of 500 MS/s (for the individual channel) and with a resolution of 12-bits. The left side (up) shows a single event which consists of two pulses generated from the generator as an input signal to the LNP-preamplifier. A straight horizontal red line indicates the baseline for the signals and it also shows the voltage level. the average amplitudes of the first and second pulse are taken between the two vertical red and green lines respectively. The right side (up) shows an output signal from the LNP-preamlifier which is adjusted up to 100 mV by the input generator signal. The bottom row shows the red and green lines which indicate the amplitude distribution of all the 30 000 events of the first and second pulse respectively. The left side (down) shows the amplitude distribution of the first input generator pulse (red line) which gives the ratio of FWHM/Amplitude: 0.2841%, and the second pulse (green line) which gives the ratio of FWHM/Amplitude: 0.7818 %. The right side (down) shows the average amplitude distribution of the first output LNP-preamplifier pulse (red line) which gives the ratio of FWHM/Amplitude: 1.0520%, and the second input pulse (green line) which gives the ratio of FWHM/Amplitude: 1.1747%.

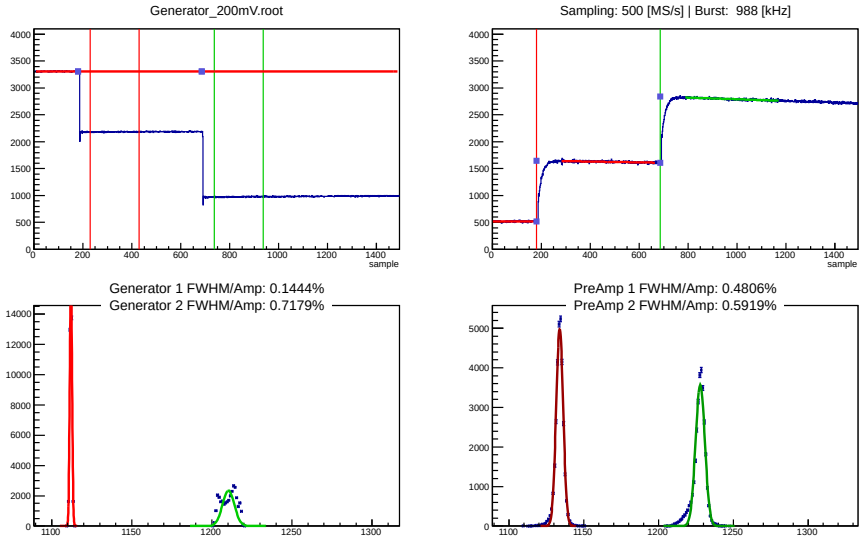

Figure 5.8: In this figure, the upper row shows a single event meaasured by the SADC with a sampling rate of 500 MS/s (for the individual channel) and with a resolution of 12-bits. The left side (up) shows a single event which consists of two pulses generated from the generator as an input signal to the LNP-preamplifier. A straight horizontal red line indicates the baseline for the signals and it also shows the voltage level. the average amplitudes of the first and second pulse are taken between the two vertical red and green lines respectively. The right side (up) shows an output signal from the LNP-preamlifier which is adjusted up to 200 mV by the input generator signal. The bottom row shows the red and green lines which indicate the amplitude distribution of all the 30 000 events of the first and second pulse respectively. The left side (down) shows the amplitude distribution of the first input generator pulse (red line) which gives the ratio of FWHM/Amplitude: 0.1444%, and the second pulse (green line) which gives the ratio of FWHM/Amplitude: 0.7179%. The right side (down) shows the average amplitude distribution of the first output LNP-preamplifier pulse (red line) which gives the ratio of FWHM/Amplitude: 0.4806% and the second input pulse (green line) which gives the ratio of FWHM/Amplitude: 0.5919%.

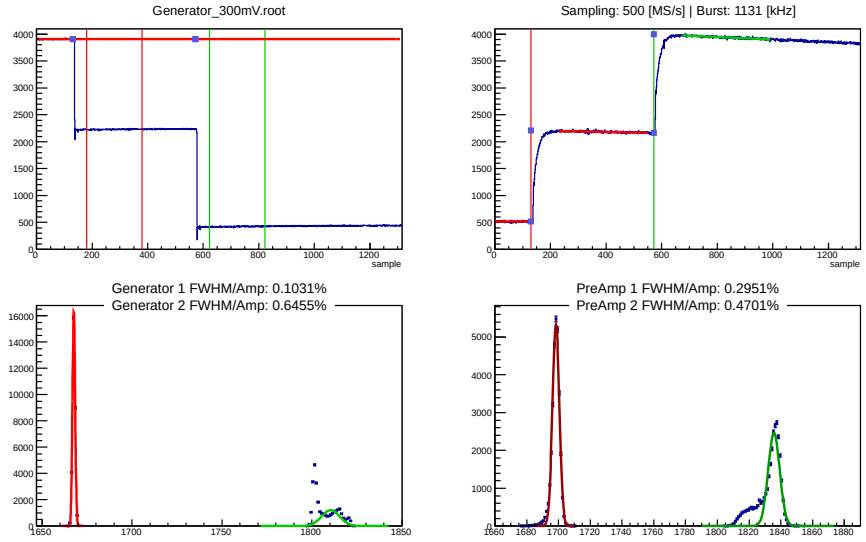

Figure 5.9: In this figure, the upper row shows a single event meaasured by the SADC with a sampling rate of 500 MS/s (for the individual channel) and with a resolution of 12-bits. The left side (up) shows a single event which consists of two pulses generated from the generator as an input signal to the LNP-preamplifier. A straight horizontal red line indicates the baseline for the signals and it also shows the voltage level. the average amplitudes of the first and second pulse are taken between the two vertical red and green lines respectively. The right side (up) shows an output signal from the LNP-preamlifier which is adjusted up to 300 mV by the input generator signal. The bottom row shows the red and green lines which indicate the amplitude distribution of all the 30 000 events of the first and second pulse respectively. The left side (down) shows the amplitude distribution of the first input generator pulse (red line) which gives the ratio of FWHM/Amplitude: 0.1031%, and the second pulse (green line) which gives the ratio of FWHM/Amplitude: 0.6455%. The right side (down) shows the average amplitude distribution of the first output LNP-preamplifier pulse (red line) which gives the ratio of FWHM/Amplitude: 0.2951%, and the second input pulse (green line) which gives the ratio of FWHM/Amplitude: 0.4701%.

Linearity comparison between input and output signals of the LNP-preamplifier

The linearity comparison between the input and output signals of the LNP-preamplifier are shown in figures 5.10, 5.11 and 5.12 with fixed pulse amplitude of 100mV, 200 mV and 300 mV respectively. The x-axis shows the delay betweeen the two input pulses varying between 0.5 μs to 10 μs and the y-axis shows the percentage of the normalized output signal as a function of delay between two bursts.

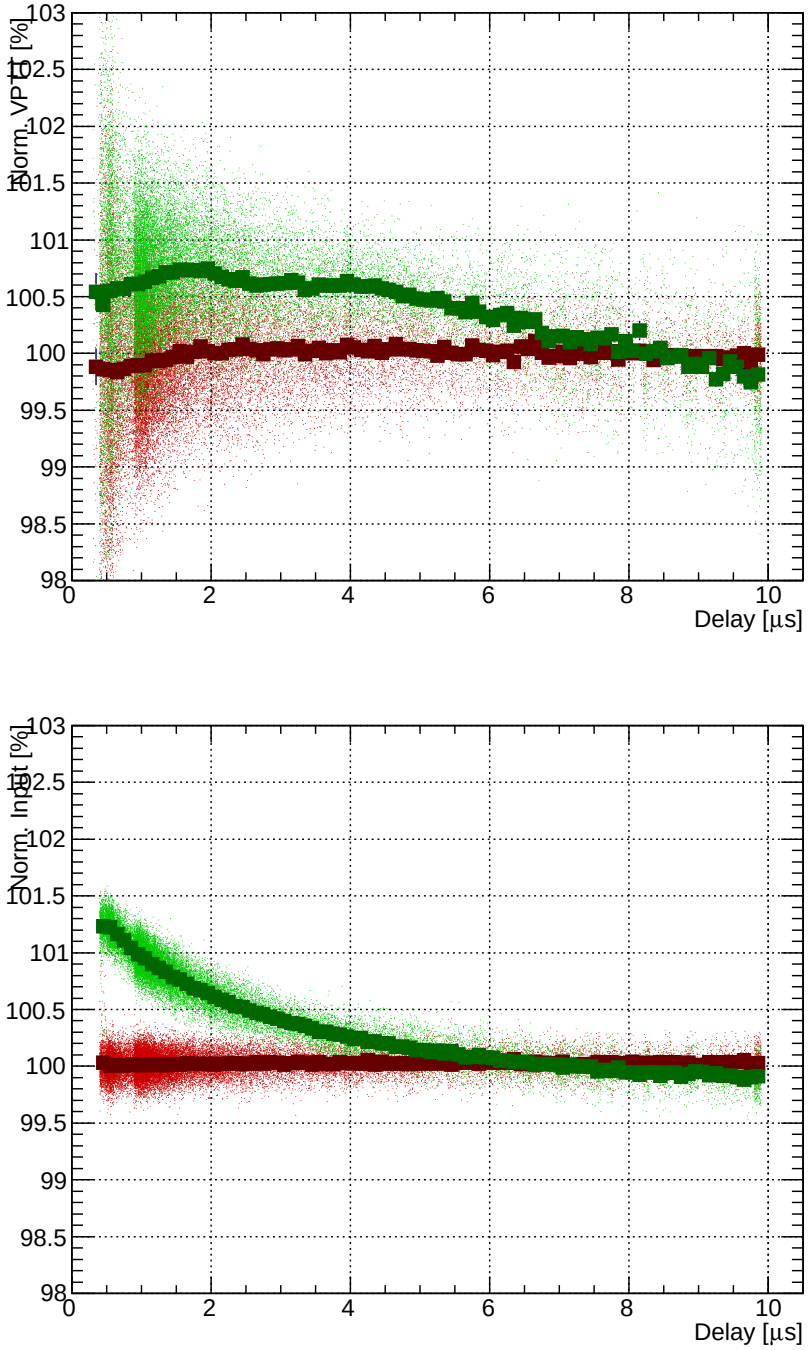

Figure 5.10: The lower histogram shows normalized input signals as a function of delay between two pulses with fixed amplitude of 100 mV. Red and green colour data points show the first and the second pulses respectively. The upper histogram shows normalized output signals of the LNP-preamlifier as a function of delay between two pulses. The red and green colour data points show the distribution of the first and the second pulses respectively. It shows some relative error which is getting bigger when the delay between the two pulses is reduced from 10 µs to 0.5 µs.

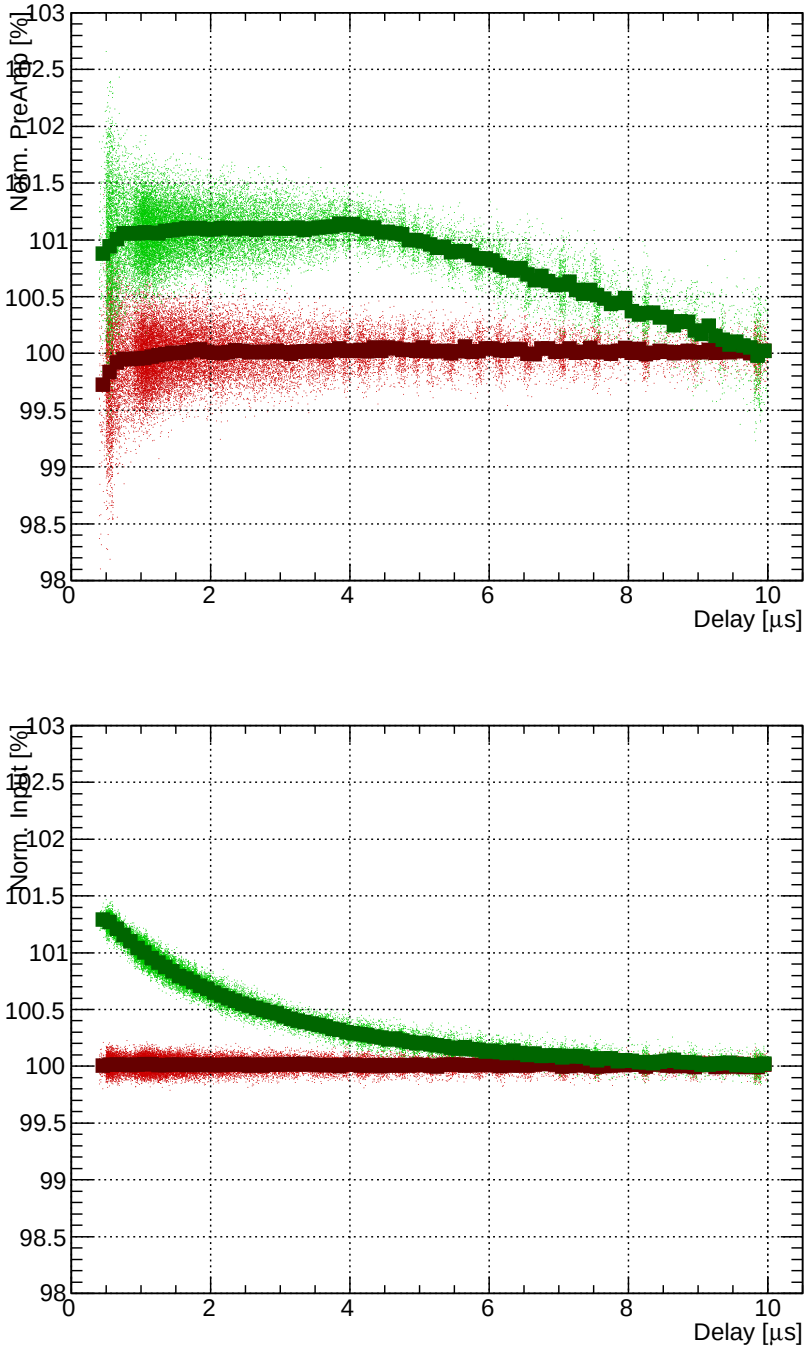

Figure 5.11: The lower histogram shows normalized input signals as a function of delay between the two pulses with fixed amplitude of 200 mV. Red and green colour data points show the first and the second pulses distribution respectively. The upper histogram shows normalized output signals of the LNP-preamlifier as a function of delay between the two pulses. The red and green colour data points show the distribution of the first and the second pulses respectively. It shows the relative error which is getting bigger when the delay between the two pulses is reduced from 10 µs to 0.5 µs.

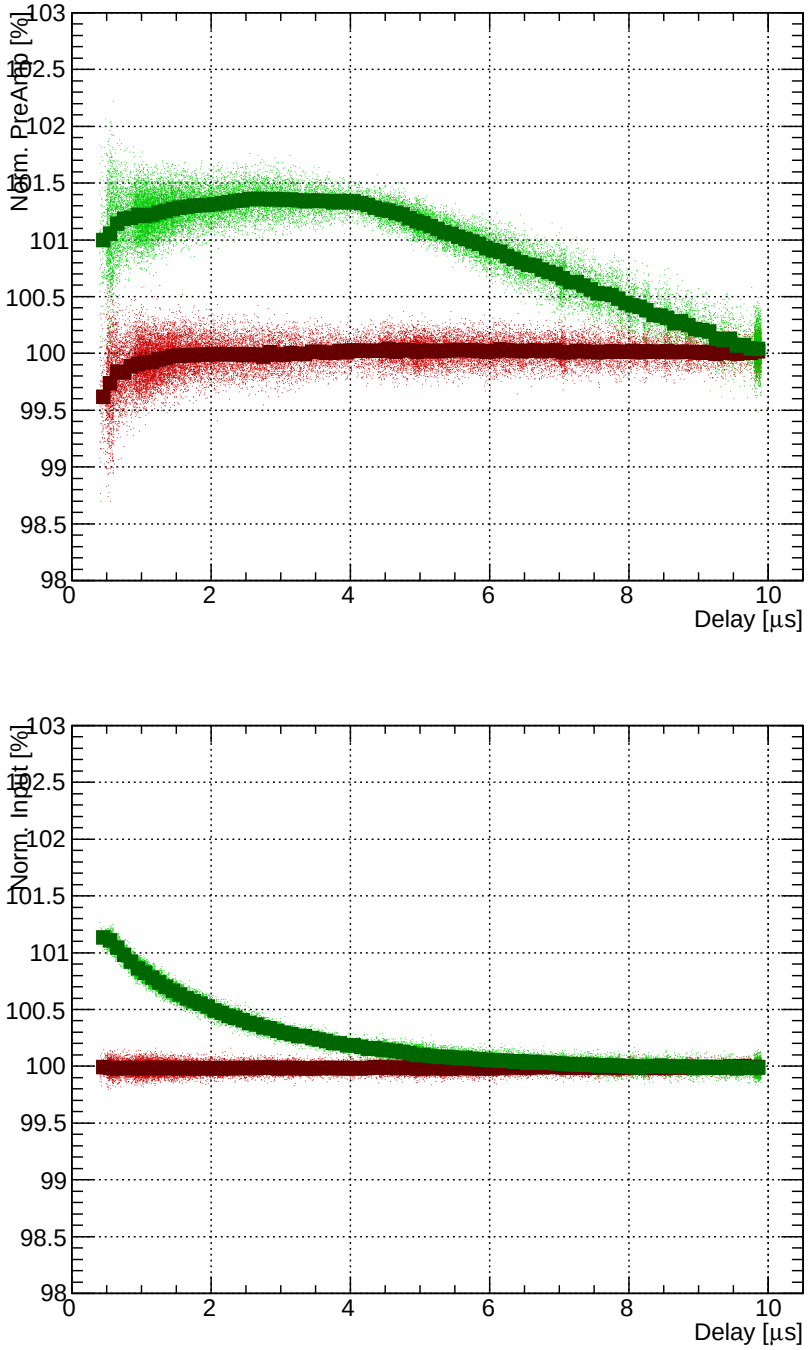

Figure 5.12: The lower histogram shows normalized input signals as a function of delay between the two pulses with fixed amplitude of 300 mV. Red and green colour data points show the first and the second pulses distribution respectively. The upper histogram shows normalized output signals of the LNP-preamlifier as a function of delay between the two pulses. The red and green colour data points show the distribution of the first and the second pulses respectively.

Discussion

By increasing the amplitude of the two pulses from 100 mV to 200 mV and 300 mV, the shift (gap) between two pulses is also increased, especially at a point of 6 μs where the input generator signals show linearity, but at the same point output LNP-preamplifer signals are shown big shift (gap). For example: in case of 100 mV: the shift is around 0.2 %, in case of 200 mV: the shift is around 0.7 %, in case of 300 mV: the shift is around 0.8 %. This happens because of the long tail pile-up effect, as the second pulse lies on the tail of the first pulse. Even the pulse signals in both cases (input generator signals and output LNP-preamplifer signals) are no more linear when the delay is reduced up to 0.5 μs between two pulses.

The test results are quite satisfactory by using 14 bit Tektronix AFG 3252 generator. The measurements of the input signals generated from the generator are not linear and it is also affecting on the output LNP-preamplifier signals.

Therefore next test is performed in a different way by using a FPGA (Field Programmable Gate Array) instead of the generator.

5.4.2 Linearity test of the LNP-preamlifier by using FPGA (Field Programmable Gate Array)

The linearity of the LNP-preamplifier is tested by using the FPGA instead of the generator and additionally using the Non-inverting current feedback summer with operational amplifier of the type AD811. In this case, two pulses are generated from the FPGA and the amplitude of the LNP-preamlifier signals are adjusted up to a fixed level of 180 mV with the help of the operational amplifier.

A test setup is illustrated in figure 5.13 and it consists of following components.

(1) FPGA (Field Programmable Gate Array) Development Board, Spartan-3AN, 133 MHz (50MHz) clock

(2) Non-inverting current feedback summer with OpAmp AD811 (R1,2,3,4=680Ω), Vcc= +/-12V

(3) Passive Splitters – optimized for 50Ω impedance

(4) coupling network: 50Ω termination +AC-coupling1pF + input load (270pF)

(5) LNP-preamplifier SP883a03 ≪low gain≫ with +/-6V linear power supply

(6) Shaper (KVI), peaking time ≪100, 200, 400ns≫ with +/-12V linear power supply (NIM-chassis)

(7) VME Interface

(8) Linex DAQ Computer

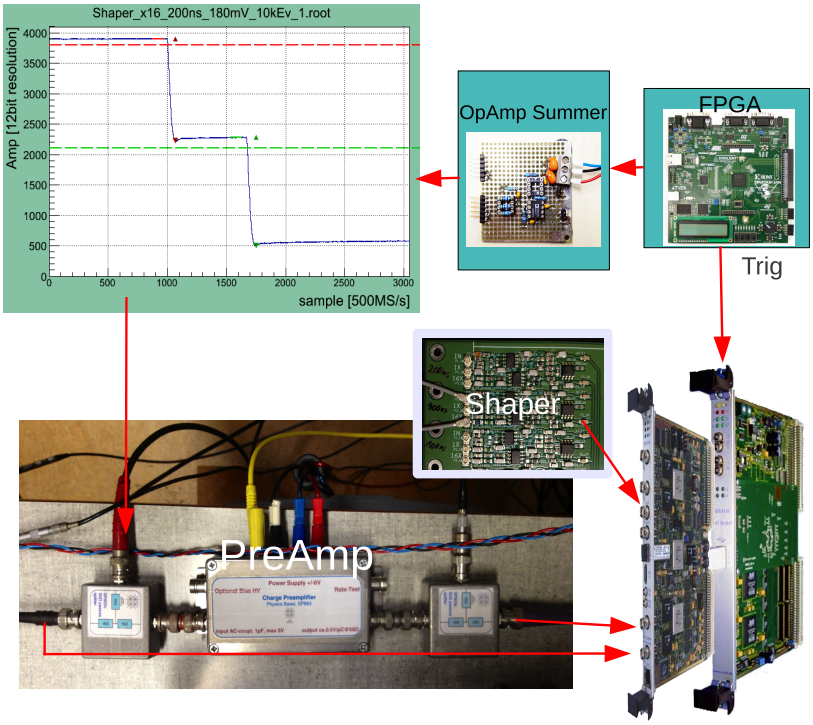

Figure 5.13: shows a sketch of the test setup and the arrangement of the experimental components used to test the linearity of the LNP-preamplifier by using the FPGA. First of all two pulse bursts were generated from the FPGA and passing through the Non-inverting current feedback summer operational amplifier. The passive splitters were used to split input signal because it keeps original shape of the signal after splitting. The output signals from the operational amplifier, LNP-preamplifier and the shaper were directed towards the channels of the SADC.

Working Principle

The working priciple is illustrated in figure 5.13. Two pulse bursts are generated from the FPGA and passing through the Non-inverting current feedback summer operational amplifier. With the help of passive splitter, each and every signal is splitted into two equal parts which are half in amplitude but same in shape. One signal is directed towards LNP-preamplifier of the type SP883a03 and the other signal is directed towards the first chanel of the SADC. Output signals from the LNP-preamplifier are again split into two equal parts, one is directed towards the shaper and the other one is directed towards the second channel of the SADC. The output signal from the Shaper is then directed towards the third channel of the SADC.

FPGA and Operational amplifier

The FPGA and the operational amplifier with their properties are shown in figure 5.14. The FPGA (Field Programmable Gate Array) consists of Development Board, Spartan-3AN, 133 MHz (50MHz) clock and the Non-inverting OpAmp consists of four resistors as in figure 5.14 (R1, R2, R3, R4) and the resistance of each resistor is $R = 680\Omega$.

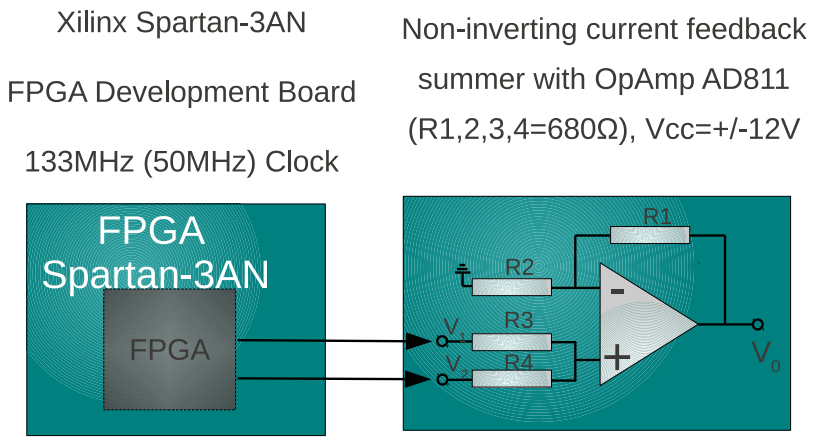

Figure 5.14: It shows the FPGA and the OpAmp. Non-inverting current feedback summer OpAmp is adding the two input burst signals generated from the FPGA and producing the combined output signal.

Double Burst Parameters

The delay between the two bursts is varying gradually between 500 ns to 10 μs and the interval between two events is 500 μs. In this case the total number of events are 10,000 and every event is sampled by 8000 times as shown in figure 5.15.

From figure 5.15, part (a) shows the input signals generated from FPGA. Red colour shows the offset (constant value) and the transition from red colour to green colour shows the appearance of the first burst signal. The transition from green colour to blue colour shows the appearance of the second burst signal. The delay between two bursts is varying gradually between 500 ns to 10 μs. Therefore the transition from green colour to blue colour is also varying from maximum to minimum.

Figure 5.15, part (b) shows the output signals from the LNP-preamplifier. Light blue colour shows the offset (constant value) and the transition from light blue colour to green colour shows the appearance of first burst signal. The transition from green colour to brown colour shows the appearance of the second burst signal. As second signal is laying on the tail of the first signal therefore green colour is transiting into brown and yellow colour, as the delay between two bursts is varying between 500 ns to 10 μs. Therefore the transition from green colour to brown colour is also varying from maximum to minimum.

Figure 5.15, part (c) shows the output signals from the shaper. Red colour shows the offset (constant value) and the transition from red colour to light green colour shows the appearance of first burst signal. These signals are really small. Then the transition from the light green colour to the red colour shows the offset (constant value). After the transition from red colour to light green colour shows the appearance of the second signal and again the red colour meaning the offset (constant value).

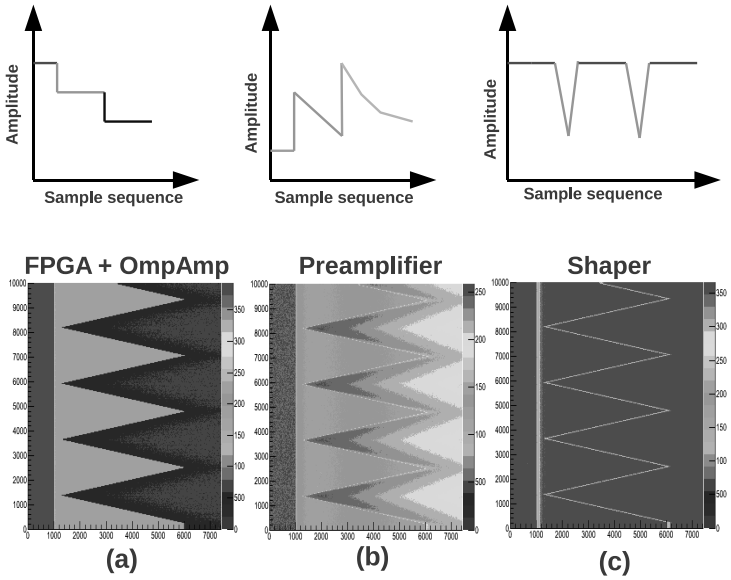

Figure 5.15: This figure shows the delay between the two bursts varying between 500 ns to 10 μs. The interval between the two events is 500 μs. The number of samples are along X-axis and number of events are along Y-axis. The total number of events are 10,000 and every event is sampled by 8000 times and their amplitude distributions are shown in all three cases (generator, LNP-preamplifier, shaper).

Test Results

As discussed earlier, the KVI shaper can be adjusted to different pulse peaking times (100 ns, 200 ns, 300 ns) and can also amplify 16X times instead of just 1X. Therefore the output LNP-preamplifier signals are tested one by one with different pulse peaking time 100 ns, 200 ns and 300 ns when the gain factors are 1X and 16X as described is table 5.1.

KVI Shaper	100 ns	200 ns	400 ns
1X	fig (5.16)	fig (5.18)	fig (5.20)
16X	fig (5.17)	fig (5.19)	fig (5.21)

Table 5.1: This table guides amoung the coming set of six figures.

All figures that are mentioned in table 5.1 are described as follows.

(a) The upper row shows a single event meaasured by the SADC with a sampling rate of 500 MS/s (for the individual channel) and with a resolution of 12-bits. The sample voltage values are shown on the Y-axis and the sample sequence number is on the X-axis. Two pulses are generated from the FPGA, which gives two LNP-preamplifier output signals and two shaper output signals respectively.

(b) The central row shows the normalized output signal amplitude as a function of delay between two bursts. Red data points indicate the distribution of the first pulse and green data points indicate the distribution of the second pulse respectively.

(c) The bottom row shows the amplitude distribution of all the 20,000 events. In the one dimentional histogram, the bins are filled with the measured amplitudes for each event and the final histograms fitted with a gauss function. The red line gauss function and green line gauss function indicate the distribution of the first and second pulses respectively. FWHM/ amplitude ratio in percentage shows how well signals are distributed.

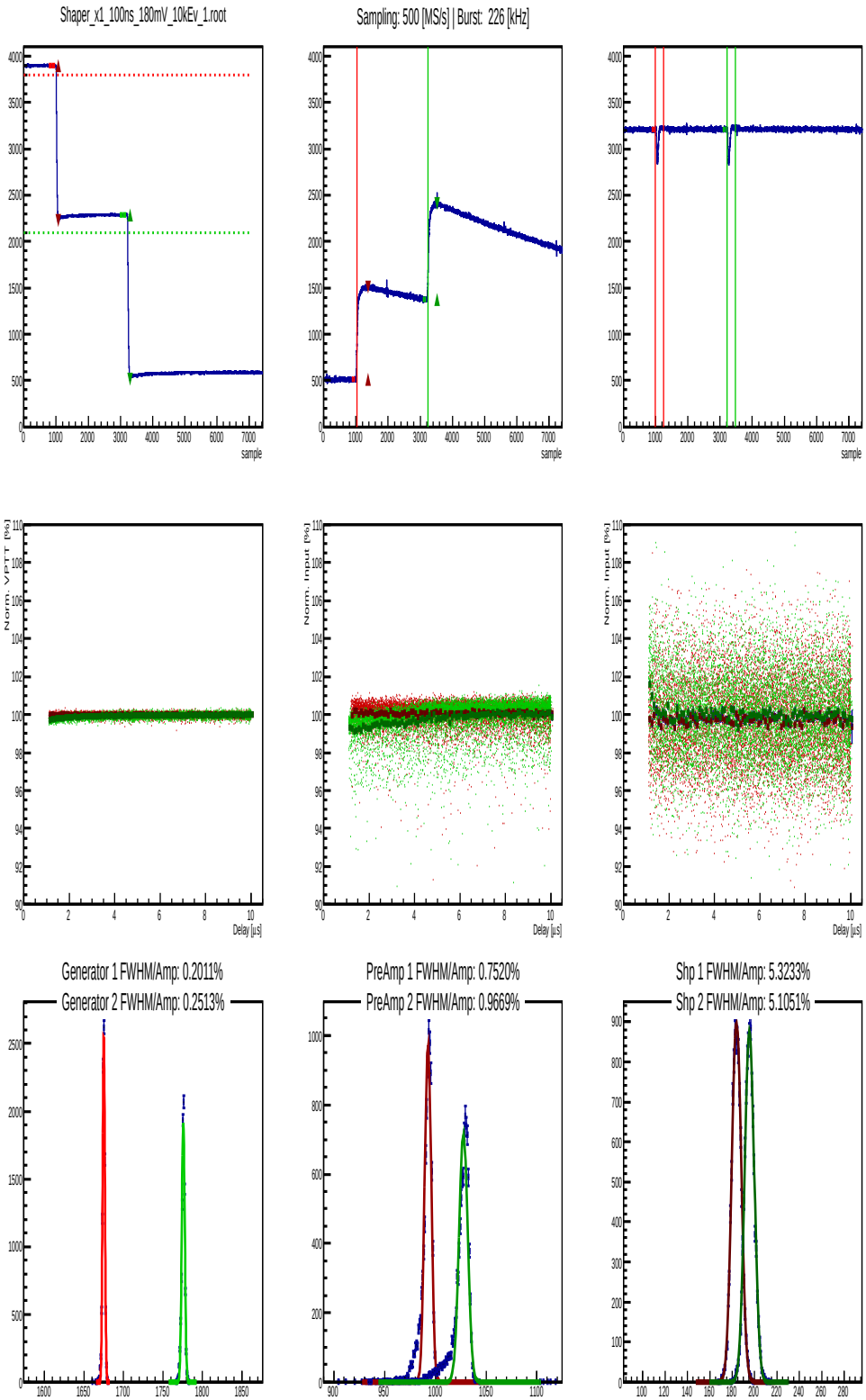

Figure 5.16: shows the output shaper signal with a gain factor of one (1X), when the pulse peaking time is 100 ns. The upper row (left to right) shows a single event generated from the FPGA, the output signal from the LNP-preamplifier and the output signal from the shaper respectively. The central row (left to right) shows the first burst (red data points), and the second burst (green data points) normalized output signal as a function of delay between the two bursts generated from the FPGA, the output signal from the LNP-preamplifier and the output signal from the shaper respectively. The bottom row (left to right) shows the amplitude distribution of all the 20,000 events of the signals generated from the FPGA, the output signal from the LNP-preamplifier and the output signal from the shaper respectively.

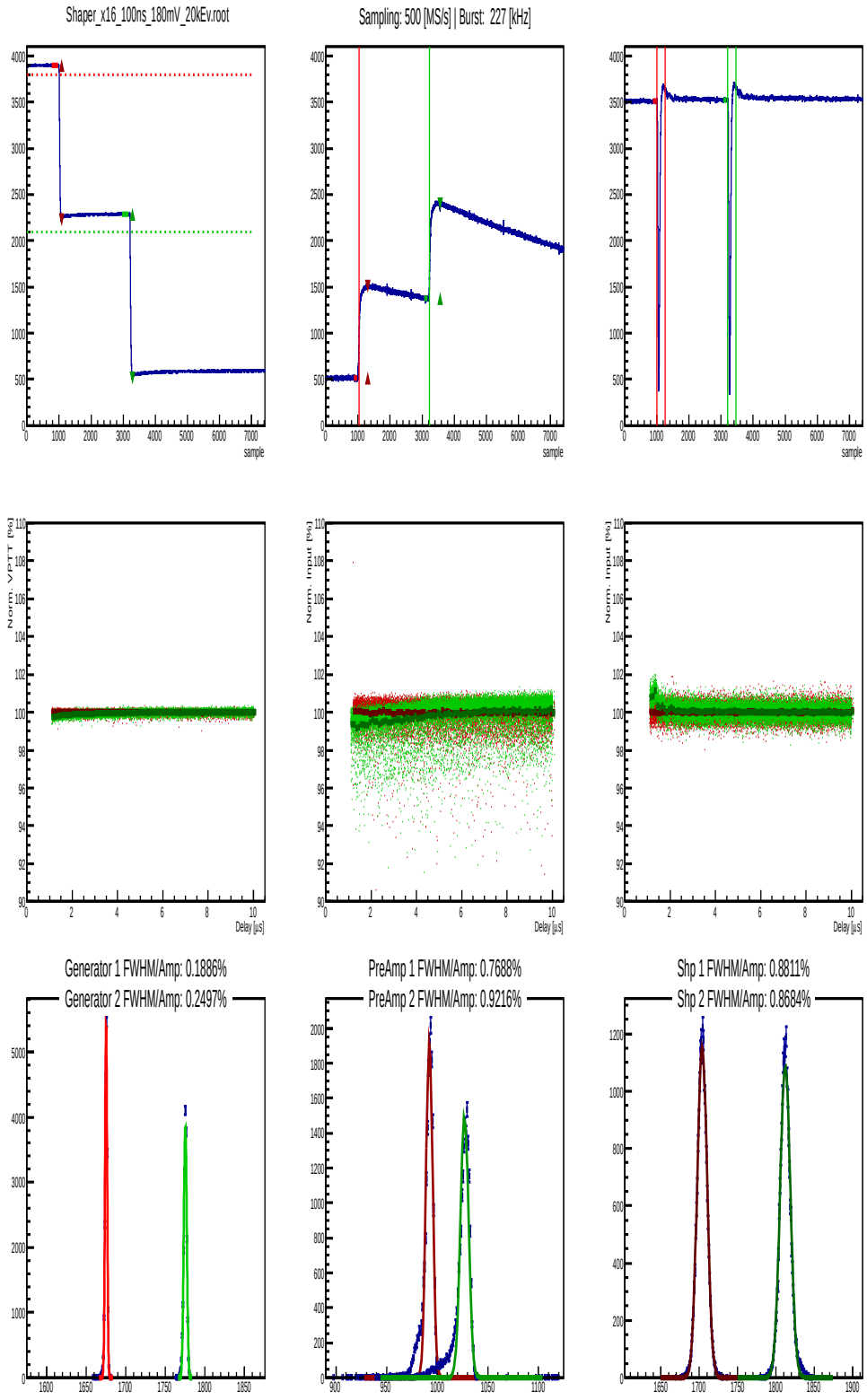

Figure 5.17: shows the output shaper signal with a gain factor of 16 (6X), when the pulse peaking time is 100 ns. The upper row (left to right) shows a single event generated from the FPGA, the output signal from the LNP-preamplifier and the output signal from the shaper respectively. The central row (left to right) shows the first burst (red data points), and the second burst (green data points) normalized output signal as a function of delay between the two bursts generated from the FPGA, the output signal from the LNP-preamplifier and the output signal from the shaper respectively. The bottom row (left to right) shows the amplitude distribution of all the 20,000 events of the signals generated from the FPGA, the output signal from the LNP-preamplifier and the output signal from the shaper respectively.

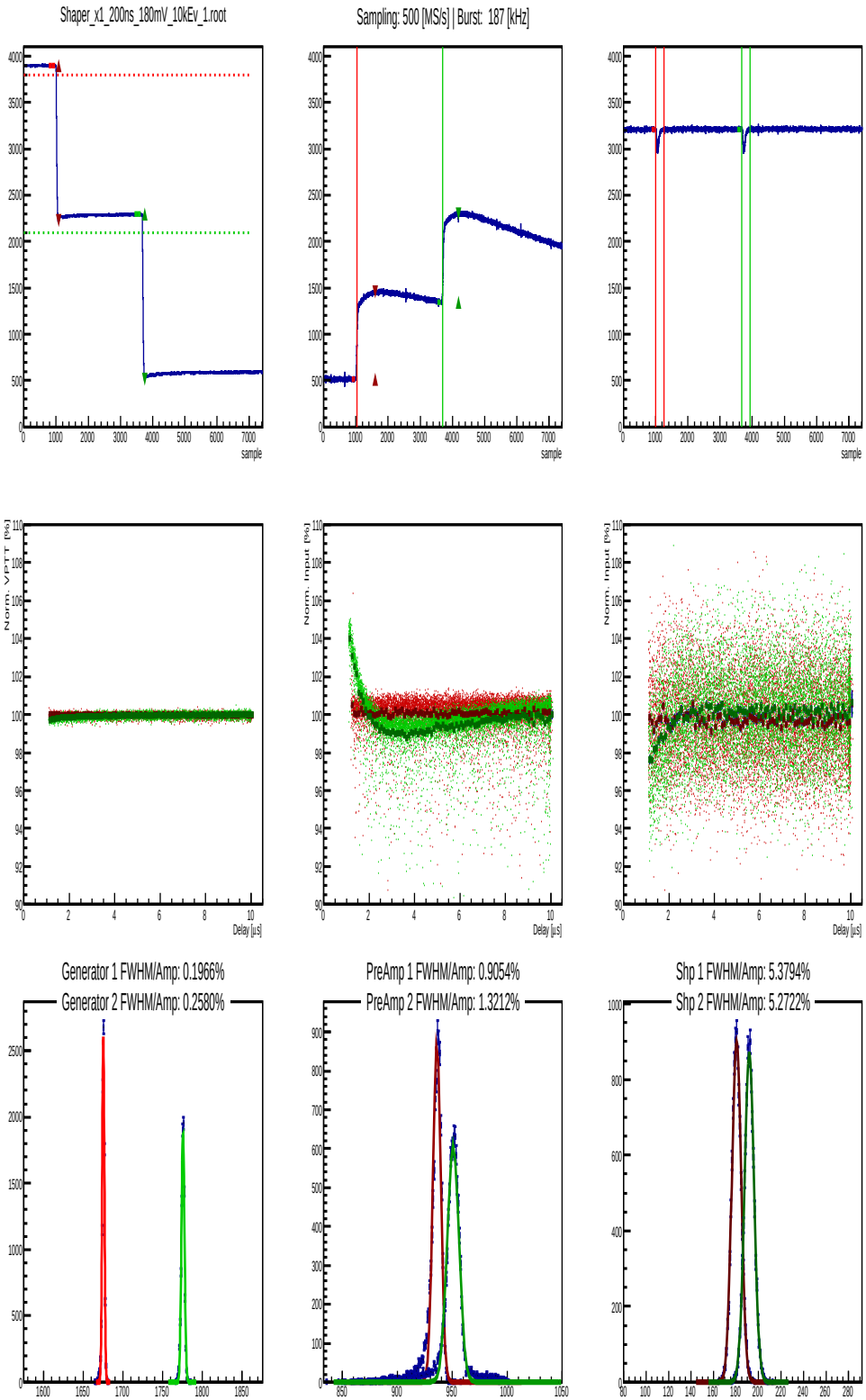

Figure 5.18: shows the output shaper signal with a gain factor of one (1X), when the pulse peaking time is 200 ns. The upper row (left to right) shows a single event generated from the FPGA, the output signal from the LNP-preamplifier and the output signal from the shaper respectively. The central row (left to right) shows the first burst (red data points), and the second burst (green data points) normalized output signal as a function of delay between the two bursts generated from the FPGA, the output signal from the LNP-preamplifier and the output signal from the shaper respectively. The bottom row (left to right) shows the amplitude distribution of all the 20,000 events of the signals generated from the FPGA, the output signal from the LNP-preamplifier and the output signal from the shaper respectively.

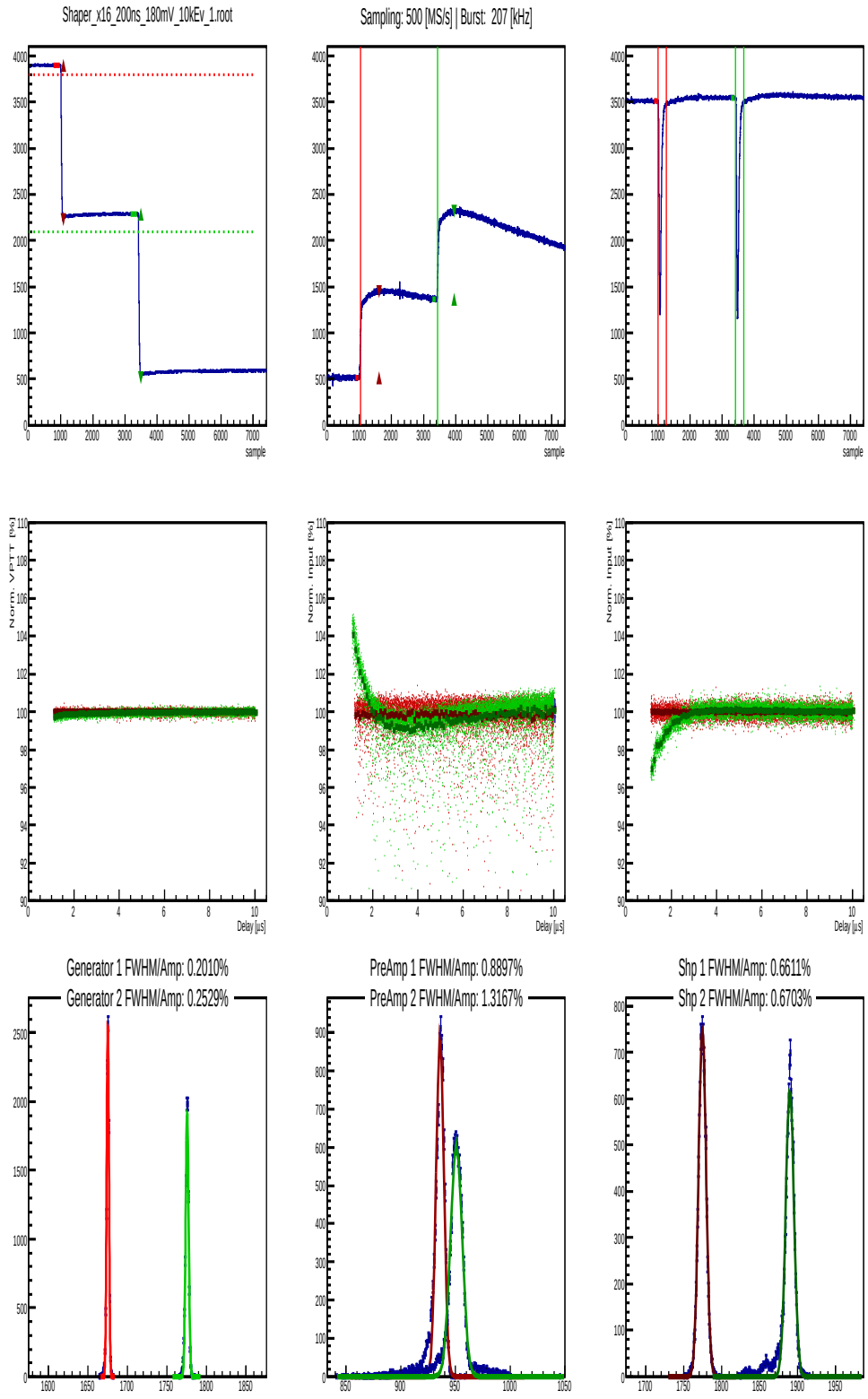

Figure 5.19: shows the output shaper signal with a gain factor of 16 (16X), when the pulse peaking time is 200 ns. The upper row (left to right) shows a single event generated from the FPGA, the output signal from the LNP-preamplifier and the output signal from the shaper respectively. The central row (left to right) shows the first burst (red data points), and the second burst (green data points) normalized output signal as a function of delay between the two bursts generated from the FPGA, the output signal from the LNP-preamplifier and the output signal from the shaper respectively. The bottom row (left to right) shows the amplitude distribution of all the 20,000 events of the signals generated from the FPGA, the output signal from the LNP-preamplifier and the output signal from the shaper respectively.

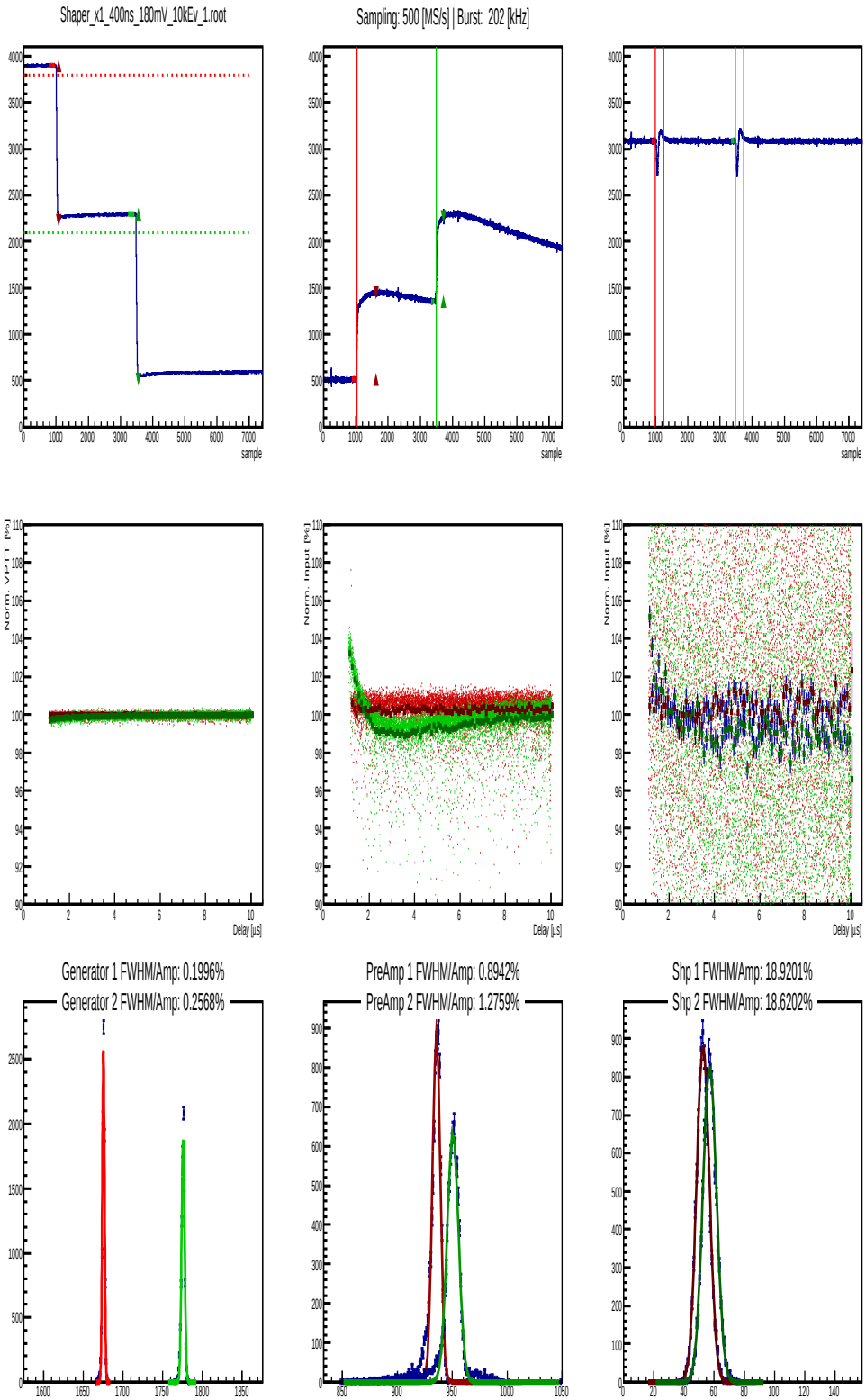

Figure 5.20: shows the output shaper signal with a gain factor of one (1X), when the pulse peaking time is 400 ns. The upper row (left to right) shows a single event generated from the FPGA, the output signal from the LNP-preamplifier and the output signal from the shaper respectively. The central row (left to right) shows the first burst (red data points), and the second burst (green data points) normalized output signal as a function of delay between the two bursts generated from the FPGA, the output signal from the LNP-preamplifier and the output signal from the shaper respectively. The bottom row (left to right) shows the amplitude distribution of all the 20,000 events of the signals generated from the FPGA, the output signal from the LNP-preamplifier and the output signal from the shaper respectively.

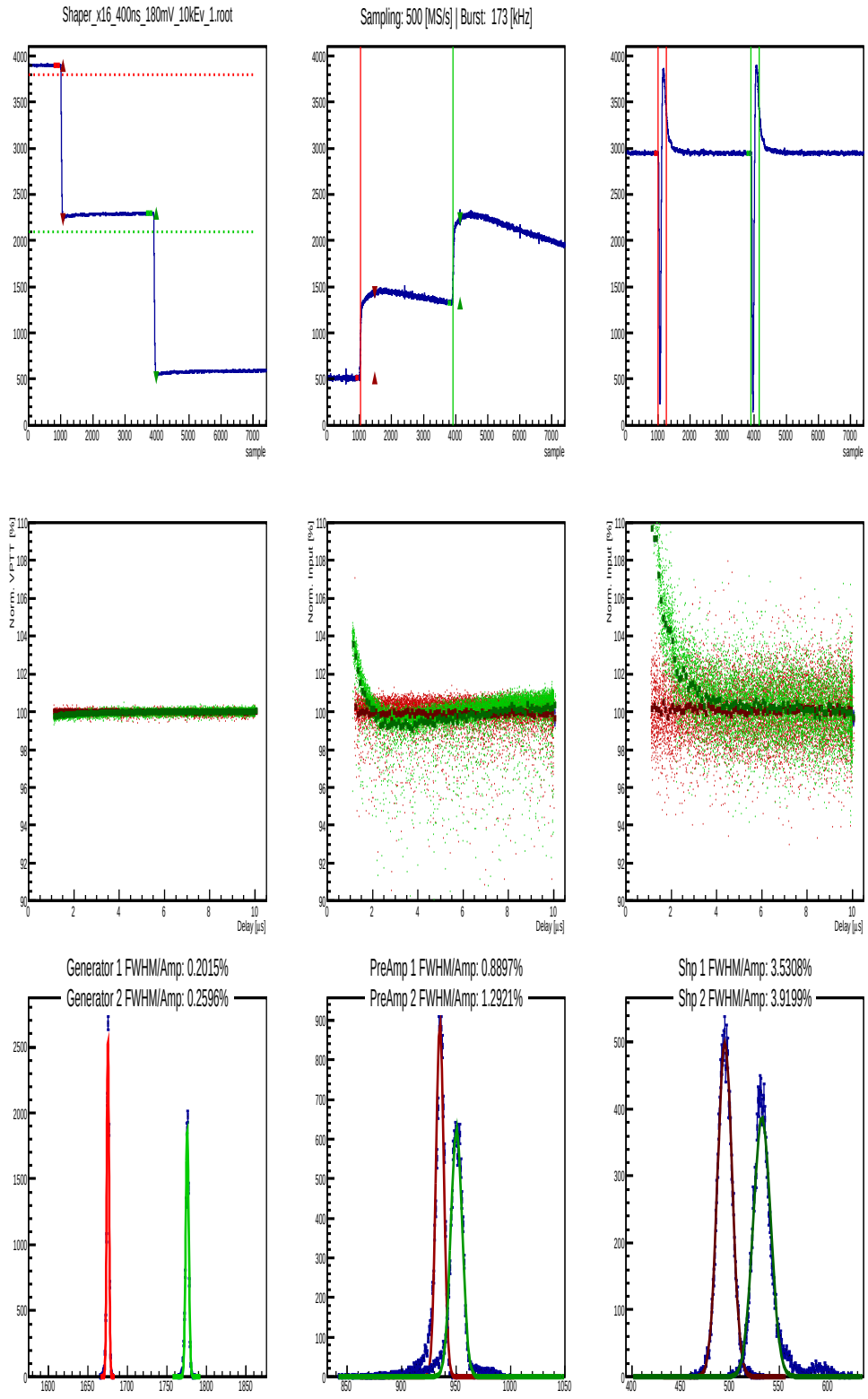

Figure 5.21: shows the output shaper signal with a gain factor of 16 (16X), when the pulse peaking time is 400 ns. The upper row (left to right) shows a single event generated from the FPGA, the output signal from the LNP-preamplifier and the output signal from the shaper respectively. The central row (left to right) shows the first burst (red data points), and the second burst (green data points) normalized output signal as a function of delay between the two bursts generated from the FPGA, the output signal from the LNP-preamplifier and the output signal from the shaper respectively. The bottom row (left to right) shows the amplitude distribution of all the 20,000 events of the signals generated from the FPGA, the output signal from the LNP-preamplifier and the output signal from the shaper respectively.

Discussion

The test results show that the FPGA plus the KVI shaper is a good combination and gives us excellent results. The linearity is within 1%, when the pulse peaking time is 100 ns. The LNP-Preamplifier shows the best performance with 100 ns shaping time, first and second pulse shows percentage ratio FWHM/Amp: 0.2011%, and the FWHM/Amp: 0.2513%, respectively. The amplitude distribution of the output signals from the LNP-preamlifier of the first and the second pulse shows a percentage ratio FWHM/Amp: 0.7520%, and FWHM/Amp: 0.9669%, respectively. Therefore the resolution difference betweeen the input FPGA signals and output LNP-preamlifier signals are very small.

In case of the output shaper signals when the peaking time is 100 ns with a gain factor of 16X we also obtain good results. It shows a percentage ratio FWHM/Amp: 0.8811%, and FWHM/Amp: 0.8684%, of the first and the second pulse respectively which is within one percent.

5.5 Linearity test of the LNP-preamplifier by connected Photodetectors

In this case different types of photodetectors (PMT, VPTT) are used to detect signals emitted from the LEDs. These are the same photodetectors as will be used in the $\bar{\text{P}}$ANDA experiment as discussed in chapter 3. The idea is to test linearity of the LNP-preamlifier in presence of photodetectors.

Therefore it is divided into two different cases.

(1) Linearity test of the LNP-preamplifier by using the function generator.

(2) Linearity test of the LNP-preamplifier by using LED driver based on FPGA (Field Programmable Gate Array)

5.5.1 Linearity test of the LNP-preamplifier by using the standard generator

In section 5.4.1, the linearity of the LNP-preamlifier is already tested by using the pulse generator. But in this case, it is tested in a different way by using the photodetectors. Two pulses are generated from the 14 bit generator with the same parameters as discussed in section 5.4.1.

A test setup is illustrated in figure (5.22) and it consists of following components.

(1) 14 bit Tektronix AFG 3252 (Arbitrary/Function Generator)

(2) Two blue LEDs (Light Emitting Diodes)

(3) Photodetectors (PMT, VPTT)

(4) LNP-preamplifier SP883a03 «low gain» with +/-6V linear power supply

(5) SADC: (Sampling Analog to Digital Converter) 12-bit, 500MS/s, 500MHz, 4ch. Struck Struck SIS3350

(6) VME Interface

(7) Linex DAQ (data acquisition) Computer

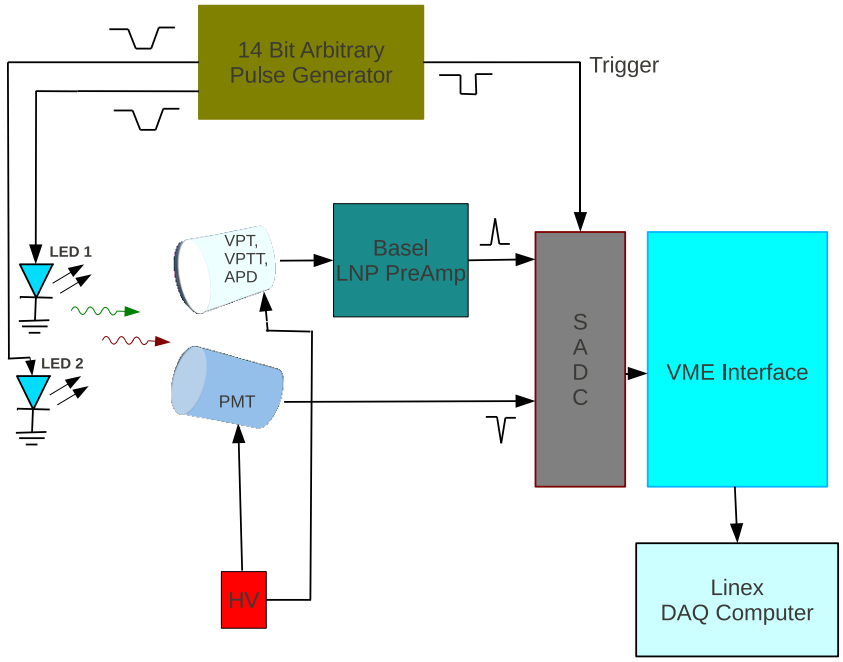

Figure 5.22: The experimental setup to test the linearity of the LNP-preamplifier by using the photodetectors.

Working Principle

Two LEDs are tested one by one to adjust the amplitude of the signal generated from the generator up to some different levels 100 mV, 200 mV and 300 mV. Then pulse bursts are sending to both LEDs (LED 1, LED 2) and detected by the photodetectors (PMT, VPTT/LAAPD) as shown in the figure (5.22). Light emitted from the two LEDs is detected by two different types of photodetectors which are placed in front of the two LEDs. The first type of photodetector is a photomultiplier tube (PMT), A high voltage supply iseg NHQ 203M (2×3 KV/4mV) is also connected with the PMT to provides high out put voltage with a very low noise.Those signals detected by the PMT are directed towards one of the channels of the SADC with the help of short coaxial cable.

The second type of the photodetector is the Vacuum Photo-Tetrode (VPTT). The signals detected by VPTT are first passing through the LNP-preamplifier of the type SP883a03 (18x28mm) with the help of a coaxial cable and then directed towards the other channel of the SADC.

Test Results

PMTs are very sensitive detectors but will not be used in $\bar{\text{P}}$ANDA experiment because of high count rates and the presence of strong magnetic fields as discussed in chapter 3. In this test, the PMT (Hamamatsu) type number R5070 with voltage divider E 2924-500 (base) is used to analyse the input signals from

the generator. The amplitudes of the output LNP-preamlifier signals are adjusted up to the different levels 100 mV, 200 mV, 300 mV with the help of the input generator signals and the results are shown in figures (5.23), (5.24) and (5.25) respectively.

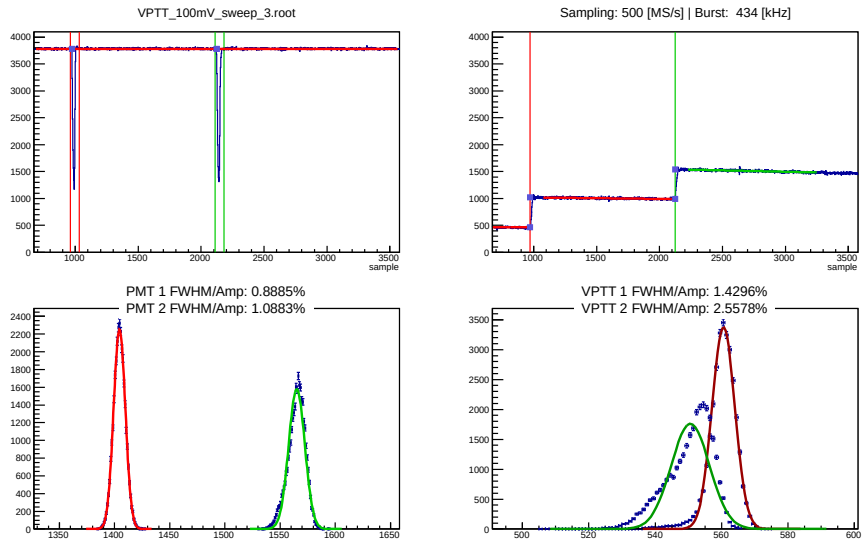

Figure 5.23: In this figure, the upper row shows a single event meaasured by SADC with a sampling rate of 500 MS/s (for the individual channel) and with a resolution of 12-bits. Left side (up) shows a single event which consists of two pulses generated from the generator with some delay detected by the PMT which gives an output PMT signal. A straight red line indicates baseline for the signals and it also shows the voltage level. The average amplitudes of the first and the second pulses are taken by two vertical red and green lines respectively. The right side (up) shows an output signal from the LNP-preamlifier which is adjusted up to 100 mV by the input generator signal. The bottom row shows red and green lines which indicate the amplitude distribution of all the 30 000 events of the first and second pulse respectively. The left side (down) shows the average amplitude distribution of the first input generator pulse (red line) which gives the ratio of FWHM/Amplitude: 0.8885% and the second pulse (green line) which gives the ratio of FWHM/Amplitude: 1.0883 %. Right side (down) shows the average amplitude distribution of the first output LNP-preamplifier pulse (red line) which gives the ratio of FWHM/Amplitude: 1.4296% and the second input pulse (green line) which gives the ratio of FWHM/Amplitude: 2.5578%.

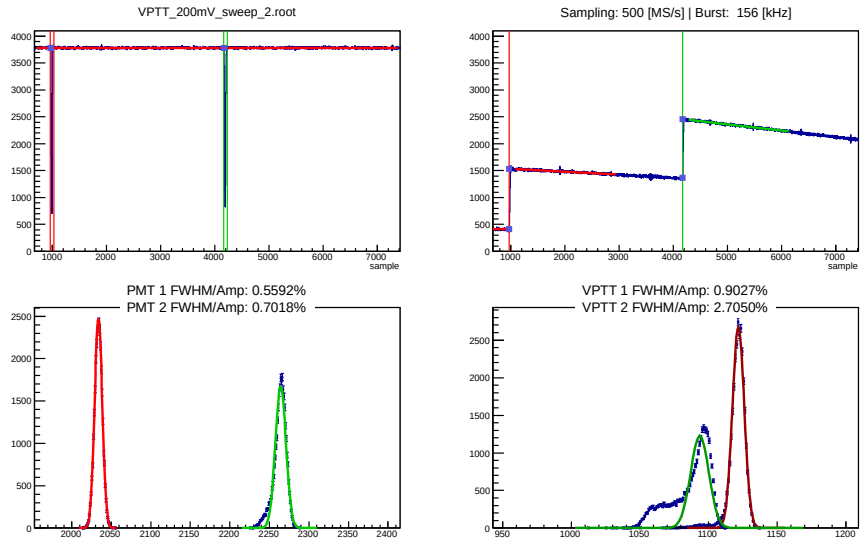

Figure 5.24: In this figure, the upper row shows a single event meaasured by SADC with a sampling rate of 500 MS/s (for the individual channel) and with a resolution of 12-bits. Left side (up) shows a single event which consists of two pulses generated from the generator with some delay detected by the PMT which gives an output PMT signal. A straight red line indicates baseline for the signals and it also shows the voltage level. The average amplitudes of the first and the second pulses are taken by two vertical red and green lines respectively. The right side (up) shows an output signal from the LNP-preamlifier which is adjusted up to 200 mV by the input generator signal. The bottom row shows red and green lines which indicate the amplitude distribution of all the 30 000 events of the first and second pulse respectively. The left side (down) shows the average amplitude distribution of the first input generator pulse (red line) which gives the ratio of FWHM/Amplitude: 0.5592% and second pulse (green line) which gives the ratio of FWHM/Amplitude: 0.7018%. The right side (down) shows the average amplitude distribution of the first output LNP-preamplifier pulse (red line) which gives the ratio of FWHM/Amplitude: 0.9027% and the second input pulse (green line) which gives the ratio of FWHM/Amplitude: 2.7050%.

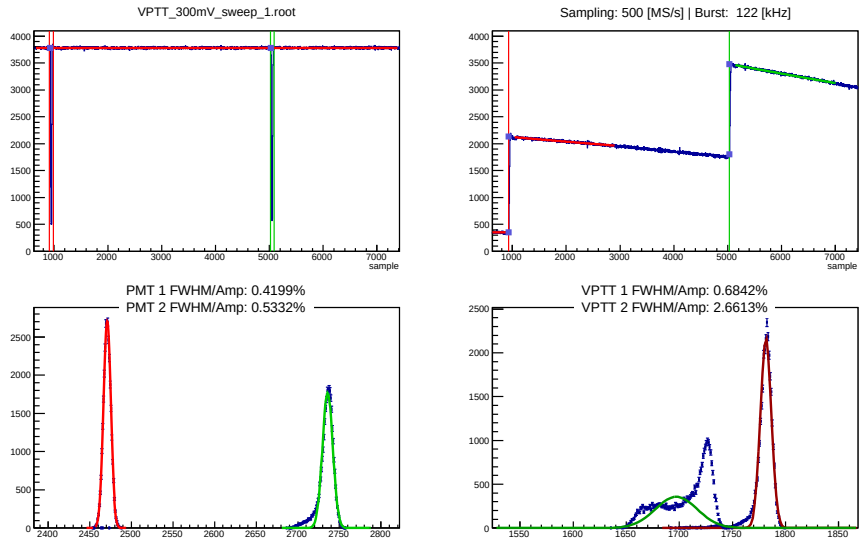

Figure 5.25: In this figure, the upper row shows a single event meaasured by SADC with a sampling rate of 500 MS/s (for the individual channel) and with a resolution of 12-bits. Left side (up) shows a single event which consists of two pulses generated from the generator with some delay detected by the PMT which gives an output PMT signal. A straight red line indicates baseline for the signals and it also shows the voltage level. The average amplitudes of the first and the second pulses are taken by two vertical red and green lines respectively. The right side (up) shows an output signal from the LNP-preamlifier which is adjusted up to 300 mV by the input generator signal. The bottom row shows red and green lines which indicate the amplitude distribution of all the 30 000 events of the first and second pulse respectively. The left side (down) shows the average amplitude distribution of the first input generator pulse (red line) which gives the ratio of FWHM/Amplitude: 0.4199% and the second pulse (green line) which gives the ratio of FWHM/Amplitude: 0.5332%. The right side (down) shows the average amplitude distribution of the first output LNP-preamplifier pulse (red line) which gives the ratio of FWHM/Amplitude: 0.6842% and the second input pulse (green line) which gives the ratio of FWHM/Amplitude: 2.6613%.

Linearity comparison between input and output signals of the LNP-preamplifier

The linearity comparison between the input and output signals of the LNP-preamplifier are shown in figures (5.26), (5.27) and (5.28) with fixed pulse amplitude of 100mV, 200 mV and 300 mV respectively. The x-axis shows the delay betweeen the two input pulses varying between 0.5 μs to 10 μs and the y-axis shows the percentage of the normalized output signal as a function of the delay between the two pulses.

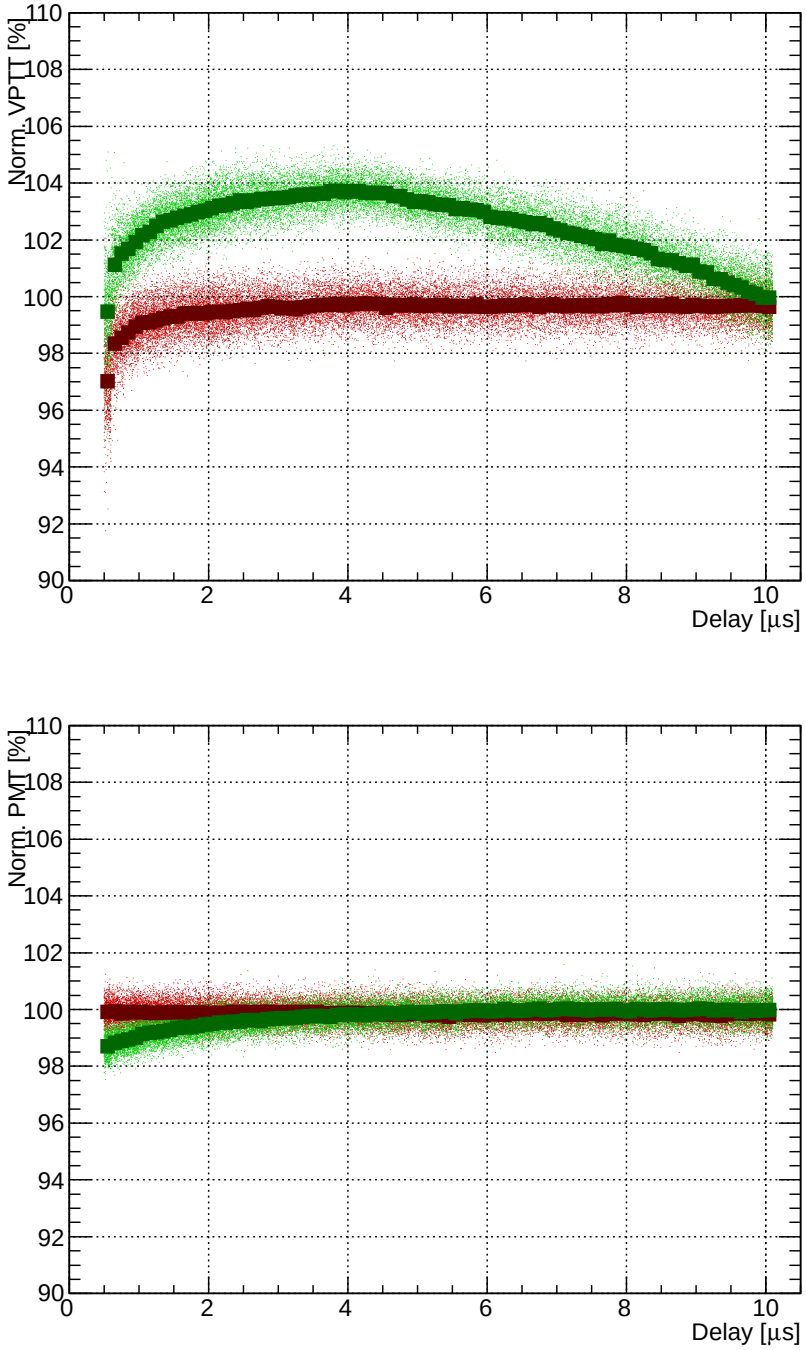

Figure 5.26: In this figure, the lower histogram shows the normalized input signals as a function of the delay between two pulses with fixed amplitude of 100 mV. Red and green colour data points show the first and the second pulses distribution respectively. The upper figure shows the normalized output signals of LNP-preamlifier as a function of the delay between two pulses. Red and green colour data points show the distribution of the first and the second pulses respectively.

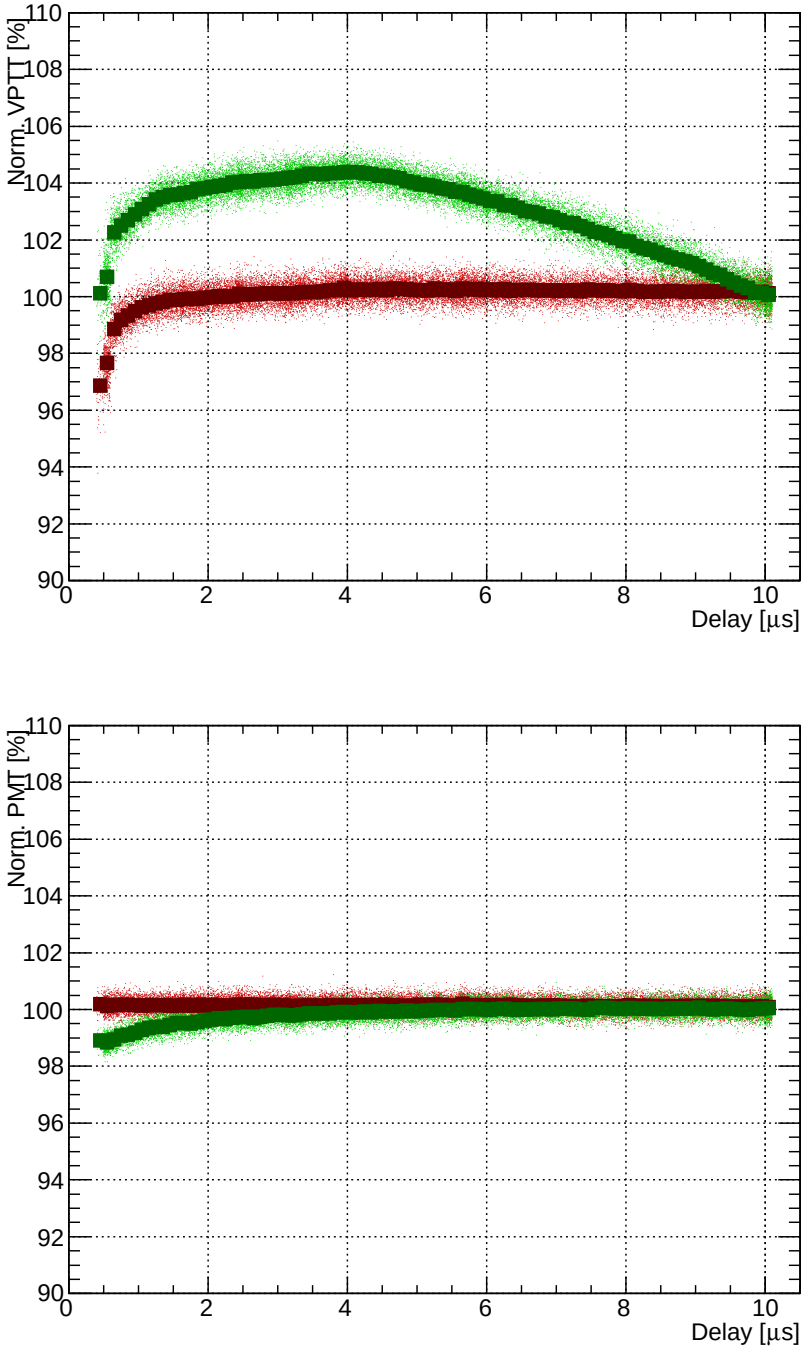

Figure 5.27: In this figure, the lower histogram shows the normalized input signals as a function of the delay between two pulses with fixed amplitude of 200 mV. Red and green colour data points show the first and the second pulses distribution respectively. The upper figure shows the normalized output signals of LNP-preamlifier as a function of the delay between two pulses. Red and green colour data points show the distribution of the first and the second pulses respectively.

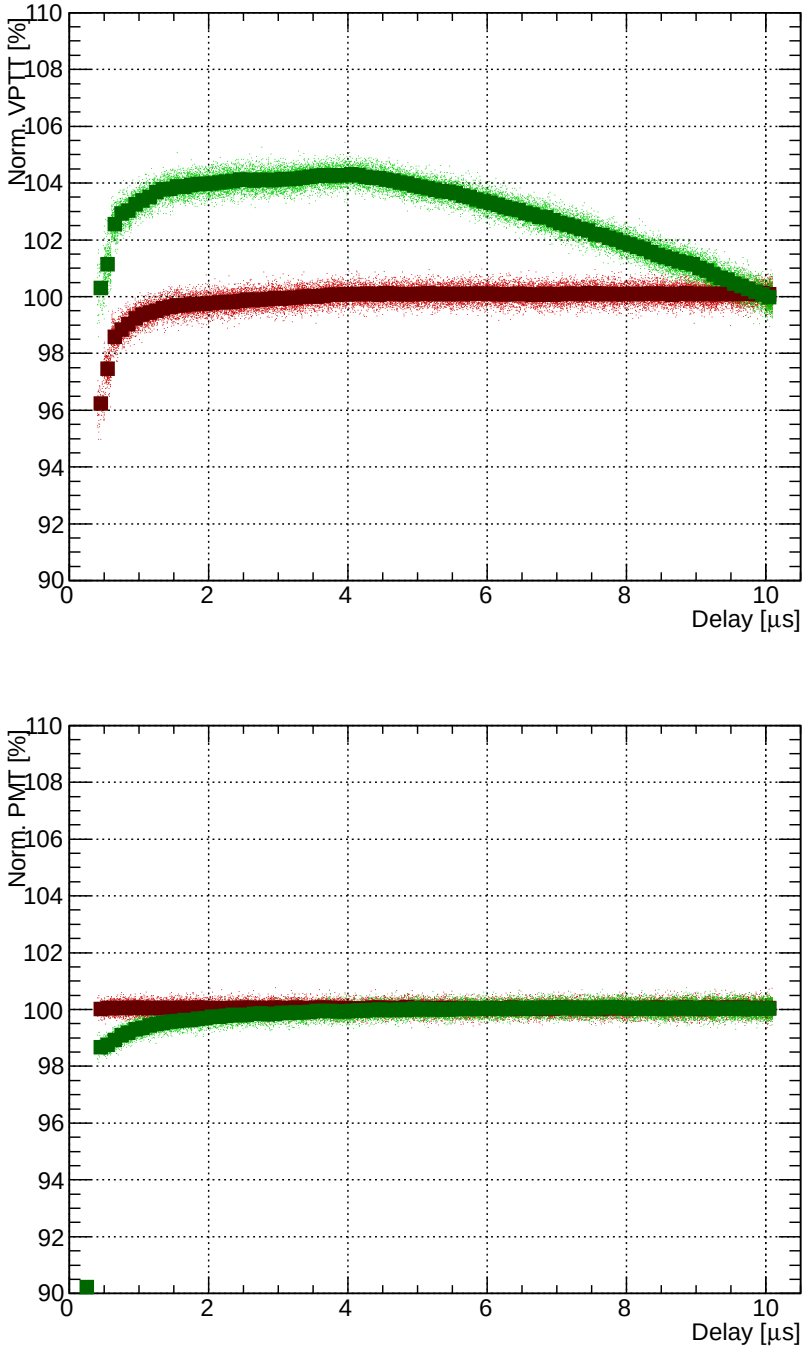

Figure 5.28: In this figure, the lower histogram shows the normalized input signals as a function of the delay between two pulses with fixed amplitude of 300 mV. Red and green colour data points show the first and the second pulses distribution respectively. The upper figure shows the normalized output signals of LNP-preamlifier as a function of the delay between two pulses. Red and green colour data points show the distribution of the first and the second pulses respectively.

Discussion

The test results are quite similar in both cases: with and without photodetectors when the input signals are generated from the function generator. In this case, the input signals generated from the generator are linear as detected by PMT the but the output LNP-preamlifier signals have not shown acceptable results. By increasing the amplitude of the two pulses from 100 mV to 200 mV and 300 mV, the shift (gap) between the two pulses is also increased, specially at a point of 4 μs where the input generator signals show linearity, but at the same point the output LNP-preamplifer signals show a big shift (gap). For example: in the case of 100 mV: the shift is around 3.0%, in the case of 200 mV: the shift is around 3.8%, in the case of 300 mV: the shift is around 4.0%. it is happened because of the long tail pile-up effect, as the second pulse lies on the tail of the first pulse. Test results are quite satisfactory inthe range of 1.0% by using 14 bit Tektronix AFG 3252 generator.

Next step is to perform linearity test in a different way by using the LED driver based on the FPGA (Field Programmable Gate Array) instead of the generator.

5.5.2 The linearity test of the LNP-preamplifier by using the LED driver based on an FPGA (Field Programmable Gate Array)

This test is performed by using the LED driver with the FPGA to test the linearity of the preamlifier. A LED driver which is specially designed to run LEDs after getting signals from the FPGA. Two identical pulses with fixed amplitude are generated from the FPGA and directed towards the LED driver. Two blue LEDs (LED 1, LED 2) are connected with a LED driver as shown in figure 5.29 and the following equipment is used in this test.

(1) FPGA (Field Programmable Gate Array) Development Board, Spartan-3AN, 133 MHz (50MHz) clock

(2) LED driver

(3) Two blue LEDs (Light Emitting Diodes)

(4) Photodetectors (PMT, VPT,VPTT,APD)

(5) LNP-preamplifier SP883a03 ≪low gain≫ with +/-6V linear power supply

(6) Passive Splitters – optimized for 50Ω impedance

(7) Shaper (KVI), peaking time ≪100, 200, 400ns≫ with +/-12V linear power supply (NIM-chassis)

(8) SADC: (Sampling Analog to Digital Converter) 12-bit, 500MS/s, 500MHz, 4ch. Struck Struck SIS3350

(9) VME Interface and Controller FPGA

(10) Linex DAQ (data acquisition) Computer

Working Principle

The working principle is illustrated in figure 5.29. Two LEDs are tested one by one to adjust amplitude of the signal generated from the FPGA. With the help of the LED driver two pulse bursts are generated. Light emitted from the two LEDs are detected by two different types of photodetectors placed in front of the two LEDs. The first type of photodetector is a photomultiplier tube (PMT).

A high voltage supply iseg NHQ 203M (2×3 KV/4mV) is also connected to the PMT to provide high output voltage. The signals detected by the PMT are directed towards one of the channels of the SADC with a short coaxial cable.

The second type of photodetector is a Vacuum Photo-Tetrodes (VPTT) type number R11375 MOD made by Hamamatsu and a high voltage supply iseg NHQ 203M (2×3 KV/4mV) is also connected with the VPTT. The detected signals are first passing through the LNP-preamlifier. Output signals from the LNP-preamplifier are split into two equal parts, one directed towards the shaper and the other one directed towards the second channel of the SADC. Output signals from the Shaper are then directed towards the third channel of the SADC.

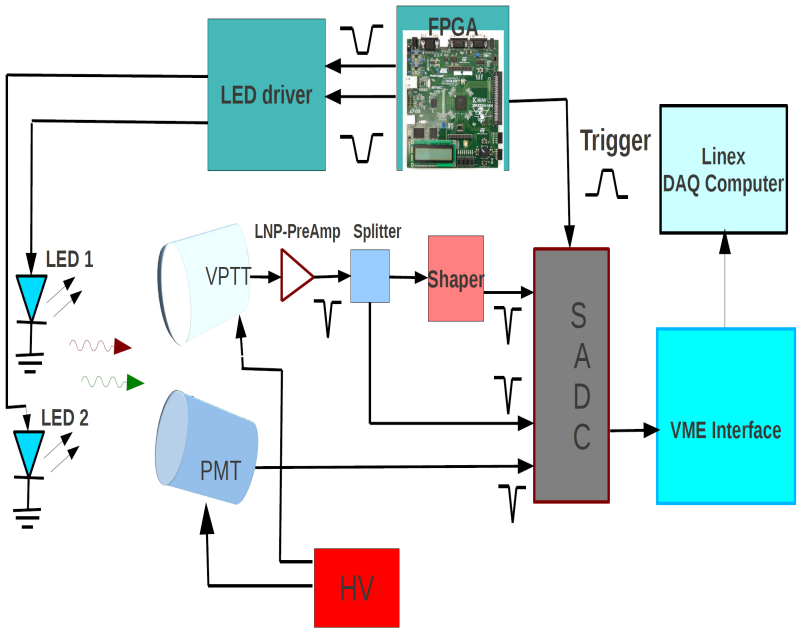

Figure 5.29: shows setup to test linearity of the LNP-preamplifier by using the LED driver based on the FPGA.

Test Results

In this test, two input signals are generated from the FPGA. With the help of the LED driver, the amplitude of the signals are fixed up to 70 mV and the delay between two bursts is varying gradually from 0.5 μs to 10 μs. The total number of events is 9386 and other beam parameters are the same as discussed in section 5.4.2 and results are shown in figure 5.30.

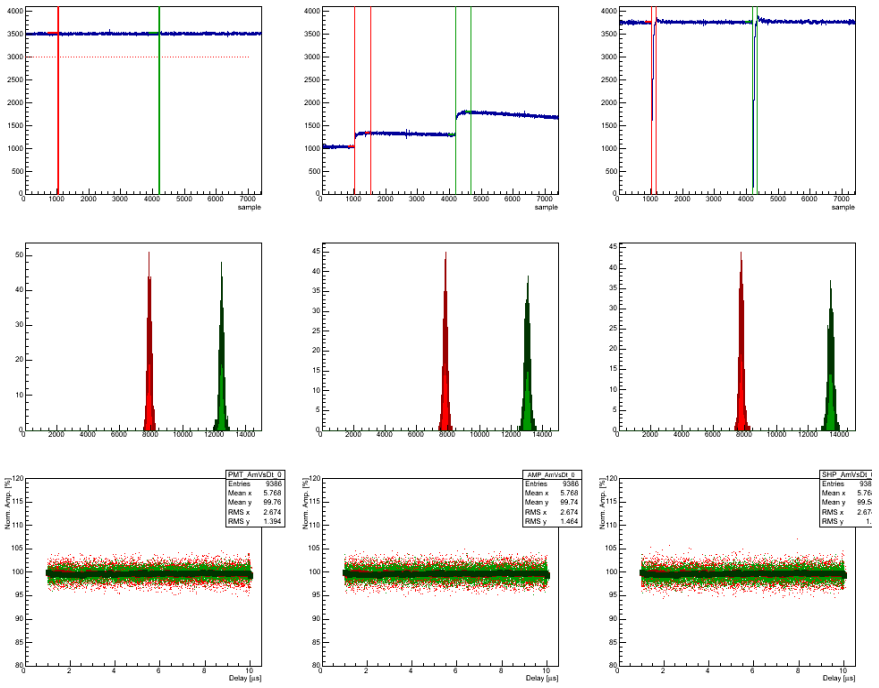

Figure 5.30: The test results are shown in three rows. Upper row (left to right) shows a single event generated from the FPGA, the output signal from the LNP-preamplifier and the output signal from the shaper respectively. Central row (left to right) shows the amplitude distribution of all the 9386 events of the signals generated from the FPGA, output signal from the LNP-preamplifier and the output signal from the shaper respectively. The bins are filled with amplitude values and the data points are fitted with a gauss function. The red line gauss function and green line gauss function fit the distributions of the first and second pulses respectively. The bottom row (left to right) shows first burst (red data points), the second burst (green data points) normalized output signal as a function of delay between two bursts generated from the FPGA, output signal from the LNP-preamplifier and output signal from the shaper respectively.

Discussion

The LED driver and FPGA is a good combination and gives us very nice results. FWHM/amplitude ratio range is almost less than 0.2%, for all delays. Which shows that the LNP-preamlifier is a linear device. In this test, the amplitude of the pulses are fixed up to 70 mV, and the LNP-preamlifier shows complete linearity.

The next step is to test the amplitude linearity of the LNP-preamlifier by using a LED driver based on FPGA (Field Programmable Gate Array).

5.6 Amplitude linearity of the LNP-preamplifier by using the LED driver based on the FPGA (Field Programmable Gate Array)

All previous tests have been done to test linearity of the LNP-preamlifier by using double bursts with fixed amplitudes and with delay varying between 0.5 μs to 10 μs. Next step is to test amplitude linearity of the LNP-preamplifier by changing the amplitudes of the input pulses with the LED driver based on the FPGA.

A test setup is illustrated in figure (5.31) and it consists of following components.

(1) FPGA (Field Programmable Gate Array) Development Board, Spartan-3AN, 133 MHz (50MHz) clock

(2) DAC (Digital to Analog Converter)12 bit DAC SPI 0-3.3V

(3) LED driver

(4) Passive Splitters – optimized for 50Ω impedance

(5) coupling network: 50Ω termination +AC-coupling1pF + input load (270pF)

(6) LNP-preamplifier SP883a03 ≪low gain≫ with +/-6V linear power supply

(7) Shaper (KVI), peaking time ≪100, 200, 400ns≫ with +/-12V linear power supply (NIM-chassis)

(8) VME Interface

(9) Linex DAQ Computer

Working Principle

Two identical pulses with fixed amplitude are generated from the FPGA and directed towards the LED driver. The amplitude of these pulses can be changed between zero to 3.3 V with the help of a DAC. Two blue LEDs (LED 1, LED 2) are connected with the LED driver. The amplitude of the events is varying from 2.5 V to 7 V, produced from the LED driver. 2.5 V is the minimum voltage which is required to emit light from the two LEDs. The rest of the process is same as discussed in section 5.5.2.

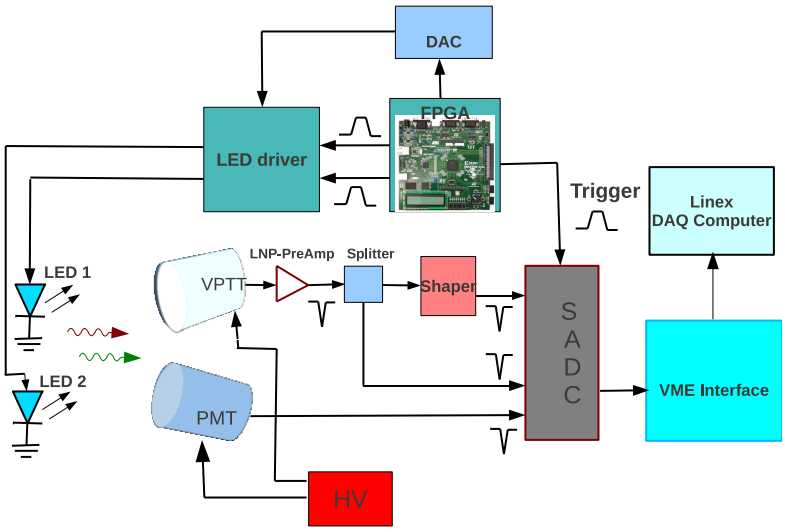

Figure 5.31: shows setup to test the amplitude linearity of the LNP-preamplifier by using LED driver based on the FPGA.

5.6.1 Test Results

As discussed earlier, the amplitude of the events are varying from 2.5 V to 7 V. The total number of events are 4223. and one of the events is shown in figure 5.32. First of all two LEDs are emitting light at the same time. After some interval light is emitted only from LED 1 and then after some interval light is emitted only from LED 2. The LNP-preamlifier would be a linear device if sum of the two pulses A(1+2) is linear to the sum of the individual pulses A (1) and A (2).

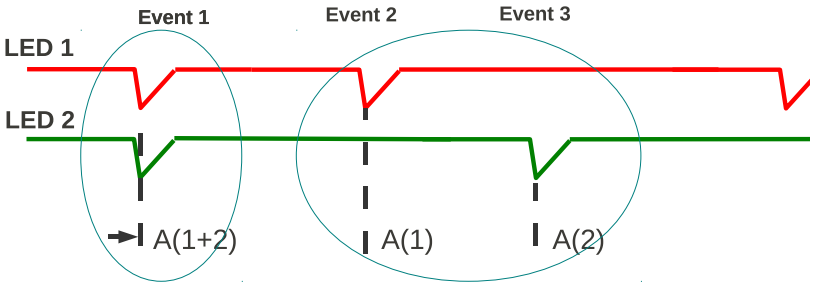

(a) Signals are emitting from the two LEDs

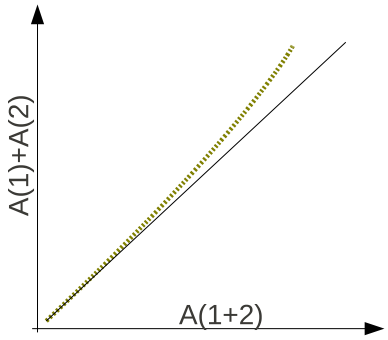

(b) Amplitude linearity

Figure 5.32: (a) The red line corresponds to LED 1 and the green line corresponds to LED 2 respectively. Event 1: two pulse signals are produced at the same time (A (1+2)) from the LED driver. Event 2: the first pulse signal (A 1) is produced after some interval, Event 3: the second pulse signal (A 2) is produced after some internval. (b) It shows the sum of the two pulses A(1+2) intended to be linear to the sum of the individual pulses A (1) and A (2). The line deflection towards sum of the indivial events shows non linearity of the output signals

.

Amplitude Linearity: Example

One of the examples to test the amplitude linearity of the LNP-preamlifier is shown in figure 5.33. It shows individual pulses A (1) and A (2) and the sum of the two pulses A(1+2) after being detected by the photodetectors (PMT, VPTT) and the LNP-preamlifier output and shaper signals.

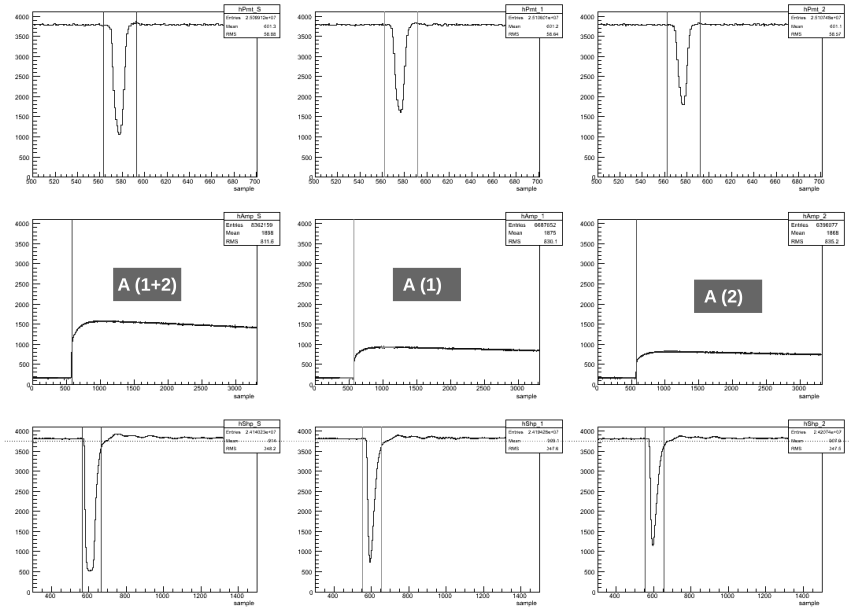

Figure 5.33: shows an example of a single event generated from the LED driver. The upper row shows the PMT output signal, the middle row shows the preamplifier output signal and the lower row shows the shaper output signal. The left hand side column shows when two pulse signals are generated at the same time A(1+2), the central column shows when only the first pulse signal A(1) is produced from LED 1, the right hand side column shows when only the second pulse signal A(2) is produced from LED 2.

Amplitude linearity VPTT: Preamplifier

Those LED signals which are detected by the VPTT are first passing through the LNP-preamlifier and than directed towards one of the channels of the SADC for continuous digitization of the LNP-preamlifier signals and shown in figure 5.34.

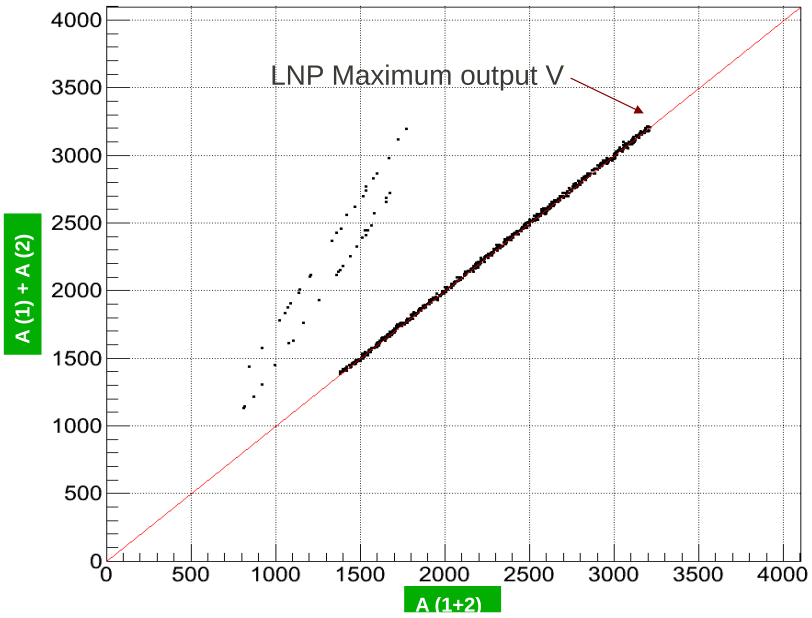

Figure 5.34: shows the linearity graph of the LNP-preamlifier output signals meaasured by the SADC. The amplitudes of all output signals are varying from minimum 2.5 V to maximum 7 V. The output signals are taken along the horizontal axis when two pulse signals A (1+2) are generated at the same time from both LEDs and the sum of the individual events A(1)+A(2) are taken along vertical axis. This graph shows that LNP-preamplifier is a linear device.

Amplitude linearity VPTT: Preamplifier and Shaper

Those LED signals which are detected by the VPTT are first passing through the LNP-preamlifier and then through the shaper. The output shaper signals are then directed towards one of the channels of the SADC and results are shown in figure 5.35.

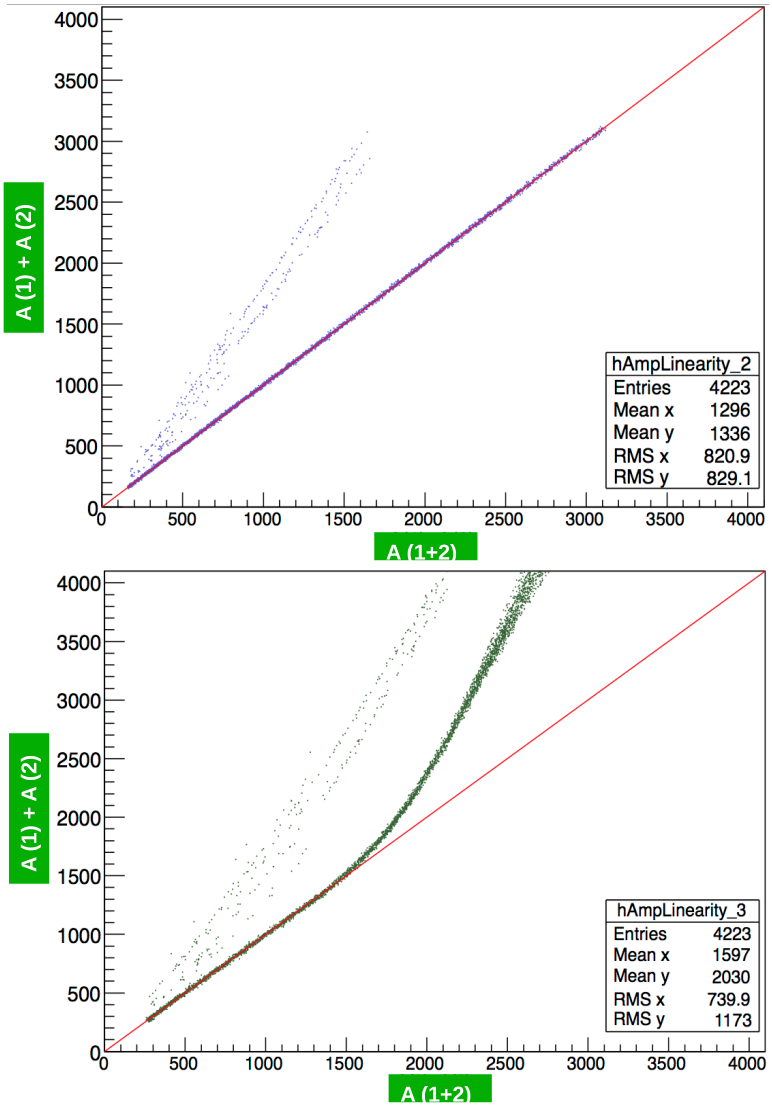

Figure 5.35: It shows the linearity graph of all the shaper output signals which are meaasured by the SADC with a sampling rate of 500 MS/s (for the individual channel) and with a resolution of 12-bits. The amplitudes of all output signals are varying from minimum 2.5 V to maximum 7 V. The output signals are taken along horizontal axis when two pulse signals A (1+2) are generated at the same time from both LEDs and the sum of the individual events A(1)+A(2) are taken along vertical axis. The red line indicates 45° angle from the horizontal axis and those shaper output signals which are lying on the red line show linearity.

Discussion

The test results show that the LNP-preamlifier is a linear device and figure 5.34 is a perfect example of that, where most of the LNP-preamlifier output signals are lying on the red line. From figure 5.35, those events which are not lying on the red line means they are not in sequence. The upper graph shows good results and we can say that the LNP-preamlifier is a linear device. The lower graph is 16 times larger than the upper graph and events with higher amplitudes are rapidly shifted towards the vertical axis. But events with lower amplitudes are still lying on the red line which is quite good because we are interested to amplify signals with lower amplitudes.

5.7 Conclusion

As discussed earlier the linearity of the measurement devices is an important feature in the experimental physics. Since 2006, Basel Univeristy (Physics department) is working for the development and testing of the LNP-preamlifier for $\bar{\text{P}}$ANDA EMC as discussed in detail in chapter 4.

In order to test linearity of the LNP-preamlifier, different tests have been performed with different combinations as discussed in chapter 5. Resent results show that the LNP-preamlifier is a linear device and can be used for $\bar{\text{P}}$ANDA EMC. These are very first measurements and can be improved further.

Bibliography

[1] http://www-panda.gsi.de/framework/documents.php
EMC Technical Design Report (Oct 2008, chapter 1)

[2] http: http://www-panda.gsi.de/framework/docsearch.php?subject=papers=on
The PANDA Experiment at FAIR, Paola Gianotti, INFN

[3] http://www-panda.gsi.de/db/talksDB/SM18-110905_Marcello-EXA2011.pdf
International Conference, September 4-9, 2011

[4] http://www-panda.gsi.de/framework/docsearch.php?subject=papers=on
"PANDA Electromagnetic calorimeters", Pavel Semenov, Yu.Kharlov, 25. JAN. 2009

[5] http://www-panda.gsi.de/framework/documents.php?section=Reports
Technical Design Reports, Oct 2008, chapter 2

[6] http://www-panda.gsi.de/db/papersDB/JM18-070910_messchendorp_menu07.pdf
11th International Conference, Jülich, Germany, September 10-14, 2007,

[7] http://www-panda.gsi.de/db/papersDBr/AR15-071008_hadron_rotondi.pdf
Conf. on Hadron Spectroscopy – Frascati, October 8-13, 2007

[8] http://www-panda.gsi.de/db/papersDBr/AG18-100610_meson10_ag.pdf
September 9, 201011 : $0WSPC/INSTRUCTIONFILEmeson10_ag$

[9] http://www.lepp.cornell.edu/charm07/talks/Wednesday/0900_voloshin.pdf
D meson spectroscopy, Mikhail Voloshin, FTPI, University of minnsota

[10] http://www-panda.gsi.de/framework/content/physics/phys_nucstruc.php
Physics - Nucleon Structure

[11] http://www-panda.gsi.de/ Welcome to the PANDA Experiment Website

[12] http://www-panda.gsi.de/db/talksDBr/KK13-111207_DOE1211_PANDA.pdf
Internal targets for the PANDA Experiment PoS(STORI11)036

[13] http://www-panda.gsi.de/db/papersDBr/GS14-110427_LEAP11-proceedings-GS.pdf
Physics and Detector, G. Schepers for the PANDA Collaboration

[14] http://www-panda.gsi.de/db/papersDBr/AK14-111009_Khoukaz_PoS_new.pdf
Internal targets for the PANDA Experiment PoS(STORI11)036

[15] http://www-panda.gsi.de/db/talksDBr/JS13-110609_PANDA_overview_TIPP11.pdf
Overview of the PANDA experiment, Jerzy Smyrski Jagiellonian University, Krakow

[16] http://www.hep.lu.se/courses/fyst17-fkf050/2012/chapter3.pdf
Oxana Smirnova, Lund University

[17] http://depts.washington.edu/nucmed/IRL/nmphysics_fall07/InteractionsWithMatter200
Robert Miyaoka, Ph.D. Old Fisheries Center

[18] http://www.hep.lu.se/staff/lytken/teaching/fys023.pdf
Leif J¨onsson, Lectures in Particle physics, Spring 2010

[19] auther = "W.R Leo", title = "Techniques for Nuclear and Particle Physics Experiments", publisher = "Springer-Verlag", volume = "Second Revised Edition" year = "1993" chapter = "10"

[20] auther = "W.R Leo", title = "Techniques for Nuclear and Particle Physics Experiments", publisher = "Springer-Verlag", volume = "Second Revised Edition" year = "1993" chapter = "2"

[21] http://learn.hamamatsu.com/articles/avalanche.html
Hamamatsu web site

[22] http://jazz.physik.unibas.ch/panda/ PANDA web site

[23] http://learn.hamamatsu.com/articles/photomultipliers.html
Hamamatsu web site

[24] http:http://sales.hamamatsu.com/en/products/electron-tube-division/detectors/phot
Hamamatsu web site

[25] http://www-panda.gsi.de/db/papersDBr/GS14-110427_LEAP11-proceedings-GS.pdf
PANDA at FAIR, physics and detector, G.schepers, Germany

[26] http://www-panda.gsi.de/html/reports.php
"Physics Performance Report", MAR. 2009

[27] http://www-panda.gsi.de/db/papersDB/MK18-121029_M.Kavatsyuk_IEEE2012-summary-I-su
PANDA web site

[28] https://indico.gsi.de/getFile.py/access?contribId=7&sessionId=6&resId=4&materialI
Front-End Electronics for the Electromagnetic Calorimeter, M. Kavatsyuk, KVI, University of Gr

[29] auther = "Glenn F.Knoll", title = "Radiation detection and measurement", publisher = "John Wiley & Sons,Inc", volume = "Forth Edition" year = "2010" chapter = "17"

Appendix A

Interaction of photon with matter

A.1 Interaction of photons with matter

Photons are electrically neutral particles with zero mass and velocity c (speed of light). They do not loose energy by coulomb interaction with atomic electrons as charged particles do. Their penetration power is much higher than charged particles.

The main intereactions of γ ray photons with matter are
(1) Photoelectric Effect
(2) Compton Scattering
(3) Thomson and Rayleigh Scattering
(4) Pair Production

Photoelectric Effect

When a photon of low energy (few electronvolts) interacts with matter and trasfers all of its energy to the atom. and disappears Then a photoelectron ejected from one of the bound shells of the atom. Energy of emitted photoelecton is

$$E_e = h\nu - E_b \tag{A.1}$$

where E_b is the binding energy of the photoelectron in its original shell. Photoelectric effect also depends on some other factors

$$P(PhotoelectricEffect) \propto \frac{Z^3}{E^3\rho} \tag{A.2}$$

Where Z is atomic number of the material, E is energy of the incident photon, and ρ is the density of the material [17]. After the ejection of the photoelectron from K or L shell, a vacancy appears. This vacancy is filled by an other free electron in the medium or by electron from the higher shells.

Compton Scattering

This is a process of elastic scattering by which a gamma-ray photon tranfers some of its energy to a free electron and another photon appears with some angle Θ from the original photon direction. Compton scattering is directly proportional to the density ρ of the material.

The scattering angle Θ is dependent on the amount of energy transfered in collision as shown in the figure (A.1).

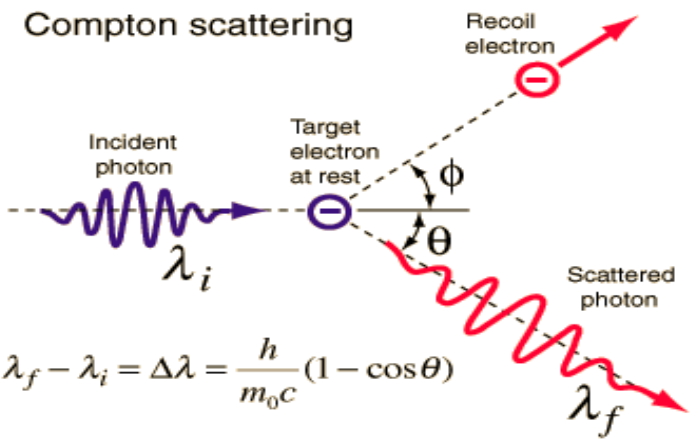

Figure A.1: An incident photon is moving with an initial wave length λ_i towards the target electron which is at rest. After collision, a scattered photon is deflected with an angle of Θ with final wave length λ_f and the recoil electron moves with an angle of Φ towards an other direction [45].

$$E_1 = \frac{E_o}{1 + E_o/m_e C^2(1 - cos\Theta)} \tag{A.3}$$

In both scattering, only the direction of the incident photon is changed and no energy is trasferred to the medium. So the atoms are neither excited nor ionized [19].

In the process of Thomson scattering, a low energy photon is scattered by a free electron in the classical limit. On the other hand, in the process of Rayleigh scattering, the photon is scattered by an atom as a whole. It is also called coherent scattering because all of the electrons in the atom act in a coherent manner. Coherent scattering is important for photons of energy greater than 50 keV [17].

Pair Production

For a pair production, the energy of an initial photon must be greater than 1.022 MeV. This process occurs when a high energy photon interects with an

electric field of charged particles [17]. The phenomenan behind this process is that when a high energy photon is passing near the nucleus of an atom then it interacts due to the strong electromagnetic field and may disappear as a photon and reappear as a pair of positive and negative electron. The total energy of a photon is converted into an electron-positron pair and kinetic energy.

Comparison

Photoelectric effect always occurs with bound electrons. The K-shell (first shell) electrons are tightly bound with the nucleus. The cross section increases rapidly as the K-shell energy is approached. After this point, the cross section drops as no more K-electrons are available for the photoelectric effect. Below this energy, the cross section rises again and drop at L, M, levels etc.

The Compton scattered cross section is defined as the average fraction of the total energy contained in the scattered photon and the Compton absorption cross section is the average energy transferred to the recoil election [20].

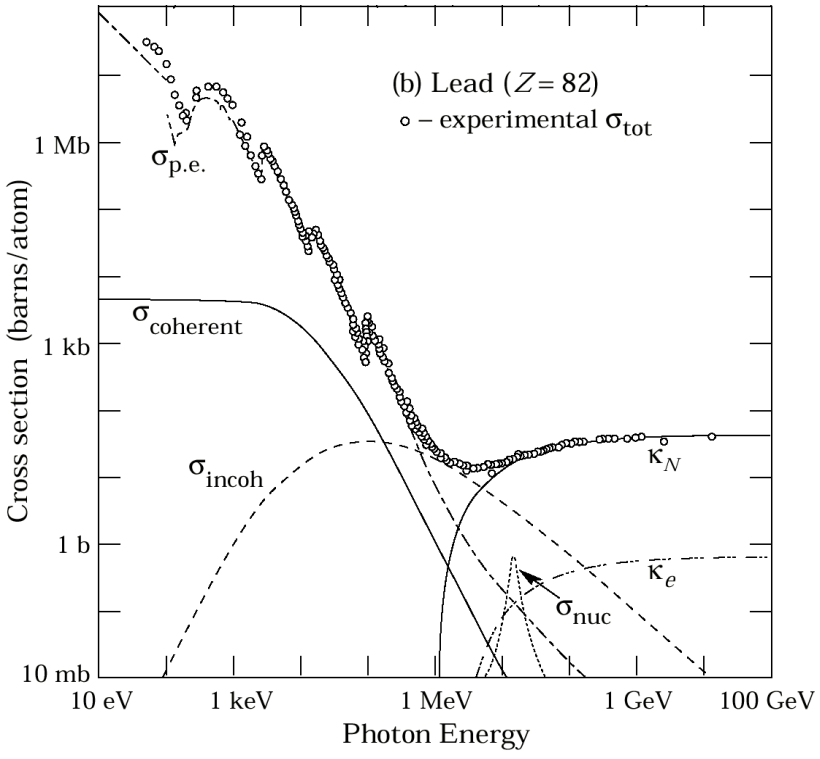

Figure A.2: It shows the total photon interaction cross-section on a lead atom [16]. The bubble curve shows the photoelectric cross section, the dotted line shows the total compton scattering cross section and a solid curve shows pair production cross section in Lead.

A.2 Assembly of the LNP-preamplifier on the VPT/VPTT (Hamamatsu)

Assembling of VPT/VPTT (Hamamatsu) with new features is shown in the figure (A.3). A round shape HV-PCB is designed only for the VPT or the VPTT (Hamamatsu) because VPTT (RIE) has different pin configuration.

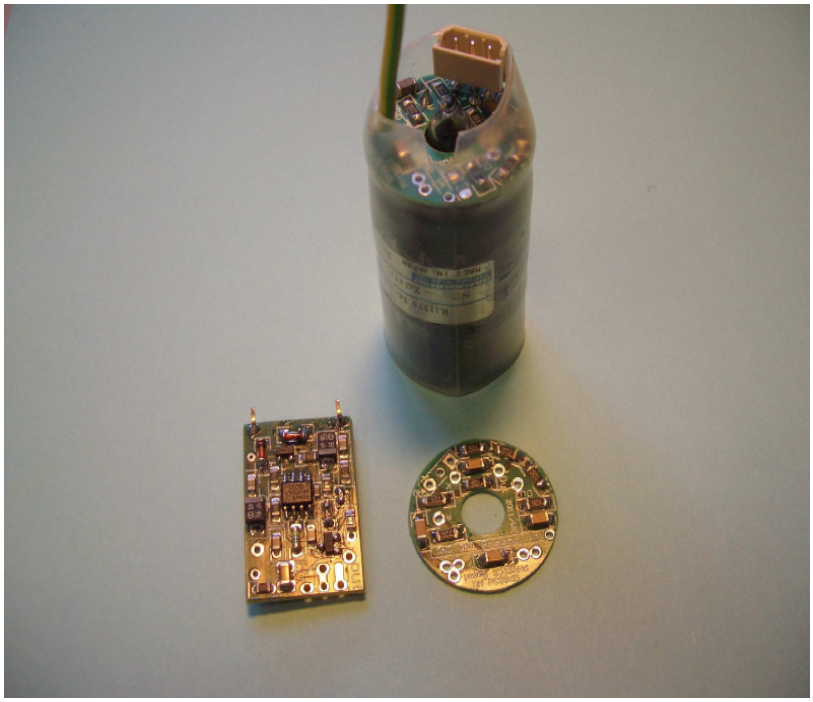

Figure A.3: Assembling of the LNP-preamplifier on the VPT/VPTT (Hamamatsu) with the HV-PCB [22].

A.3 Noise measurement setup

After the development of LNP-preamplfier, it is necessary to test its performance. For that purpose a noise measurement setup has been sketched at Basel university (Physics department). With the help of this test setup, we can test the performance of the LNP-preamplfier with respect to the low noise / low power consumption. Some of the basic components have been used to measure the noise of the LNP-preamplfier and the test setup is shown in the figure (A.4).

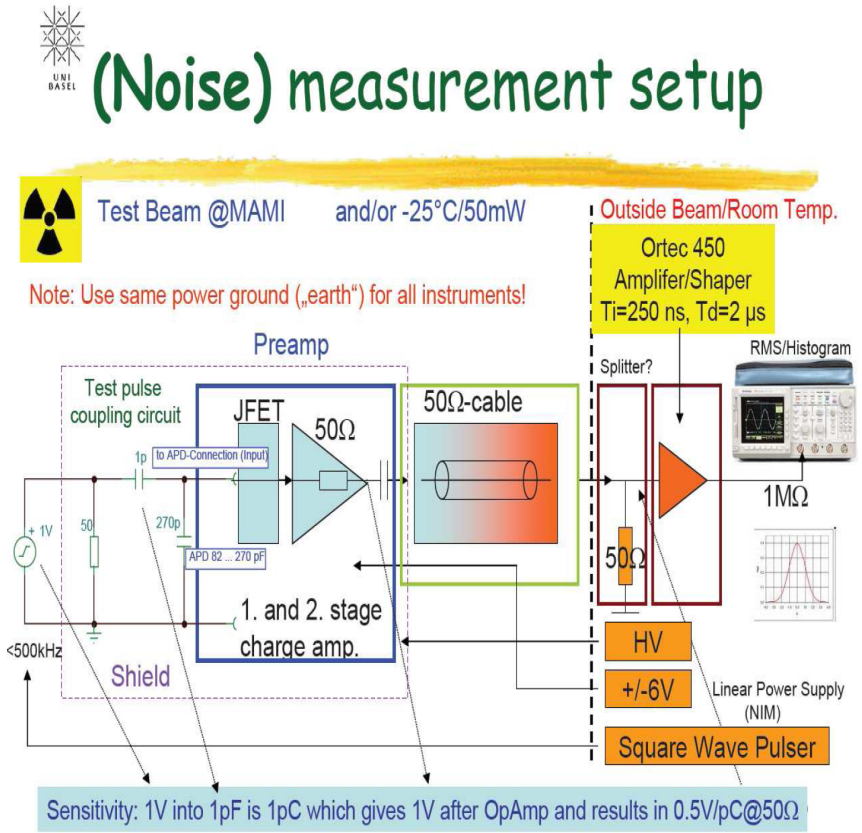

Figure A.4: shows a noise measurement setup to test noise of the different types of the LNP-preamplfiers. A LNP-preamplfier of a type SP883a03 is used for this Setup [22].

The test setup consists of three basic components: detector, LNP-preamplifier and shaper. The pulse coupling circuit is one of the important components as shown on the left side of figure (A.4). It acts as a detector producing 1V pulse passing through a capacitor of 1 pF and gives 1 pC. Then this charge sent to the LNP-preamplfier which acts as an interface between the detector and the rest of the electronics. The LNP-preamplifier consists of charge sensitive configuration to integrate the incoming charge pulses and produced voltage pulses. External power supply (+/- 6 V) is also connected with LNP-preamplfier to charge it. Different types of LNP-preamplfiers are used during this process. The LNP-preamplfier of different types are used in the noise measurement setup. According to the noise measurement setup, output signal from the LNP-preamplfier is 1 V and results in 0.5 V/pC at 50 Ω resistance. and moved towards the amplifier shaper with a 50 Ω cable. The amplifier converts the output signal into a suitable signal and gives a result of 0.5 V/pC at 50 Ω. Which is usable to measure the energy and timing of the signal.